Author:
Froggatt, Edith Sarah

Title:
An investigation of scrambling in Langmuir-Blodgett films using neutron and x-ray reflectivity.

AN INVESTIGATION OF SCRAMBLING IN LANGMUIR-BLODGETT FILMS USING NEUTRON AND X-RAY REFLECTIVITY

by
Edith Sarah Froggatt

A thesis submitted to the University of Bristol in accordance with the requirements of the degree of Doctor of Philosophy in the School of Chemistry, Faculty of Science.

January, 1999.

Abstract

The problem of scrambling or interlayer mixing in alternating Langmuir-Blodgett (LB) films is a serious hindrance to the application of the technique to the formation of molecular-scale devices which fully exploit the possibilities of molecular electronics. Neutron reflectivity is used here, in conjunction with X-ray reflectivity, to investigate order within fatty acid LB films. Samples with only one deuterium-labelled mono- or bilayer are shown to give the required information on the distribution of that labelled layer through the film, which is not possible with alternating structures. The X-ray data give information on total film thickness and density, enabling monolayer thicknesses to be calculated. This information is used to deduce the phase of the dipped monolayers and hence put forward a possible explanation of how and why scrambling occurs. For the neutron data, a new modelling approach is described which uses a gaussian to model the distribution of deuterium-labelled material within the sample, and very good fits to the data have been obtained. The results from this approach are not only consistent with the conclusions of other workers to date, but by enabling better quality fits to be obtained they greatly enhance understanding of the scrambling phenomenon, and some very positive results are described, namely, the preparation of several unscrambled LB films.

By varying the experimental parameters, such as monolayer pressure, subphase pH, temperature or ion composition, dipping speed, time under water and position of the labelled layer, one at a time, it is shown that consideration of both dipping speed and film viscosity enables LB films to be prepared in which the labelled layer has not mixed with the surrounding layers. This is explained in terms of the Langmuir film of a fatty acid having to be in the S phase, and having to be dipped at a rate which ensures complete and uniform transition to the L_2 phase during deposition, or the L_2' phase if increased head-head binding is present, e.g. dipping against an amine, to obtain an unscrambled LB film. Surface potential results are used to provide qualitative macroscopic illustrations of the different monolayer phases, which are then used to explain the above observations. A high surface pressure monolayer must therefore be dipped slowly, whilst a lower surface pressure monolayer can be dipped faster, to give unscrambled films.

The preparation of LB films of eicosylamine alternating with docosanoic acid shows that with the increased headgroup interaction, scrambling is totally eliminated, whereas with docosanoic acid as the first layer, no order is seen. This is explained in terms of differences in film phase when compared with acid-acid films. The current theory on the origin of pyroelectricity in such amine-acid films (changes in molecular dipole moment) is given further support by the observation of an increase in film thickness on heating.

Three polysiloxane molecules with side chains having terminal carboxylic acid groups are shown to form LB films with insufficient layer structure to allow a labelled layer to remain unmixed.

Memorandum

The work described in this thesis was undertaken in the Department of Physical and Theoretical Chemistry within the School of Chemistry at the University of Bristol under the supervision of Dr. R. M. Richardson between October 1993 and September 1996 and is the original work of the author unless stated otherwise in the text. No part of this work has previously been submitted for a degree at this or any other university. The views expressed in this thesis are those of the author and not of the University.

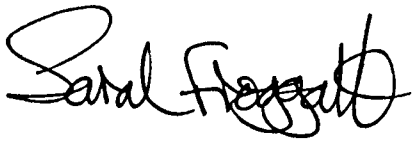

Sarah Froggatt.

Acknowledgements

I would like to thank my supervisor, Dr. Rob Richardson, for his help and guidance throughout, and Drs. Jeff Penfold, John Webster and Dave Bucknall at ISIS for their help through many neutron experiments, especially during SURF commissioning time. Thanks are also due to Dr. Tim Richardson at Sheffield and Dr. Dave Lacey at Hull for provision of the polymeric pyroelectric molecules and the perdeuterated amine.

Thanks to Mum and Dad, my brothers and all my friends for moral support and encouragement, particularly during my writing up, and special thanks to Stephen for some very impromptu and frantic maths lessons, Helen for a vast amount of expert typing and invaluable help with graph-plotting software, and Jack for supportive comments and superbly constructive criticism.

Thanks to the Chemistry Workshops for helping me to get my equipment working, sometimes doing it for me yesterday. Thanks too to Dr. Silas Ndiye for some very stimulating discussions on life, the universe and molecules.

And how could I forget my fellow inhabitants of E004, past and present? Simon, Jason, Lesley, Ali the mad Zog, Pepe the mad triathlete, Sam the body builder, Adam the footballer and Iain the (definitely mad) climber - cheers, guys, and thanks for everything!

ESF.

Note

This thesis uses the non-standard unit of the Angstrom ($1\text{Å} = 10^{-10}$ m) instead of the SI-preferred unit of the nanometre.

Chapter 1. Introduction.

1.1. Introduction

This chapter gives a brief history of the study of Langmuir-Blodgett films and discusses their potential in molecular electronics applications, together with a summary of why this work was undertaken.

1.2. History

Thin films of oils or other molecules floating on water have been used for millennia. The ancient Babylonians used the patterns formed by pouring oils on water as a form of divination, and the Japanese used dyes floating on water to deposit patterns on paper by laying the paper on the water-and-dye surface. However, little was understood about the phenomenon.

Benjamin Franklin carried out several experiments on the calming effect of oil on water but it was not until the end of the nineteenth century that serious scientific study began. Agnes Pockels carried out a rigorous series of experiments (in her kitchen!) looking at fatty acids and her results correlate extremely well with modern work carried out on far more sophisticated equipment. Lord Rayleigh began working on such films at around the same time and he suspected that they were monomolecular, i.e. one molecule thick. Workers recognised the need for molecules to have a hydrophilic and a hydrophobic end for films to form. For a fuller introduction to the early history of the field, the interested reader is referred to the first chapter of [1] and references therein.

At the beginning of the twentieth century Irving Langmuir was working on gas adsorption at the General Electric Laboratories in Schenectady, NY. A natural progression from this was to look at liquid adsorption at the air-water interface and the study of monomolecular films gathered momentum. Such films are now called Langmuir films and the apparatus he devised is known as the Langmuir trough. His first paper on the subject [2] was published in 1917 and after this initial study he revisited the area several times over the next 20 years or so. His work in this field is reviewed in [3].

In 1935 Katherine Blodgett, working in the same laboratory as Langmuir, published the first paper describing the technique of preparing multilayer films on solid substrates by dipping them through the floating monolayer [4] and such films are known as Langmuir-Blodgett or LB films. There was much excitement about the commercial potential of LB films and Blodgett published several patents on a wide variety of applications, most exploiting the optical properties of the films and the precise thickness control available with the technique. For instance, by varying the pH of the subphase and its known metal ion content at the time of dipping, different proportions of fatty acid and salt can be incorporated into the LB film. The acid can be dissolved out, leaving a "skeleton" film of salt, whose refractive index can thus be varied directly in relation to the dipping conditions [5].

Blodgett and Langmuir both moved on to study other areas and interest waned until Hans Kuhn started investigating such films in the late 1960s. Other groups followed suit and work now focused on widening the types of system studied to include di-chained molecules, complex headgroups, branched chains and mixed films containing two or more compounds. An excellent review of this period is given in [3].

1.3 Molecular Electronics.

In the 1970s and 1980s, increasing interest in electronics prompted a rapid awakening to the potential of the LB technique for producing highly ordered systems with the desired properties "built-in", as Blodgett had foreseen 40 years earlier.

As molecular modelling and organic synthesis become more sophisticated, molecules can be designed and built to maximise certain properties, for example dipole moment, optically-triggered bistable conformational changes or electrical conductivity. Combined with the LB technique, this opens up a wide range of potential applications in the field of Molecular Electronics, where building devices up from particular molecules means that such devices can be made extremely small, thus providing faster switching and response times, lower power requirement and less heat dissipation than current silicon-based technology. In addition, since it is possible to ensure by design that these molecules are transparent in either the visible or infra-red part of the spectrum, the possibility of

addressing components by laser beam becomes a reality. This would give additional speed benefits as well as eliminating the need for hard-wiring components to the outside world. Other applications closer to commercial exploitation include forming sensors out of molecules sensitive to particular gases using the LB technique [6], and a range of biochemical uses, such as enzyme assays or drug screening, can be addressed by immobilising the molecule under study in an LB film which mimics its normal *in vivo* environment [6]. An excellent summary of these and other potential applications is given in the final chapter of reference [1].

1.4 Reasons for This Work.

Two particularly promising molecular electronics applications for LB films are Second Harmonic Generation (SHG) [1] and pyroelectric effects [1], as outlined in Appendices 1 and 2. Both of these phenomena rely on a noncentrosymmetric arrangement of their constituent molecules, with all dipole moments pointing in the same direction. This can be achieved in either of two ways (Fig. 1.1).

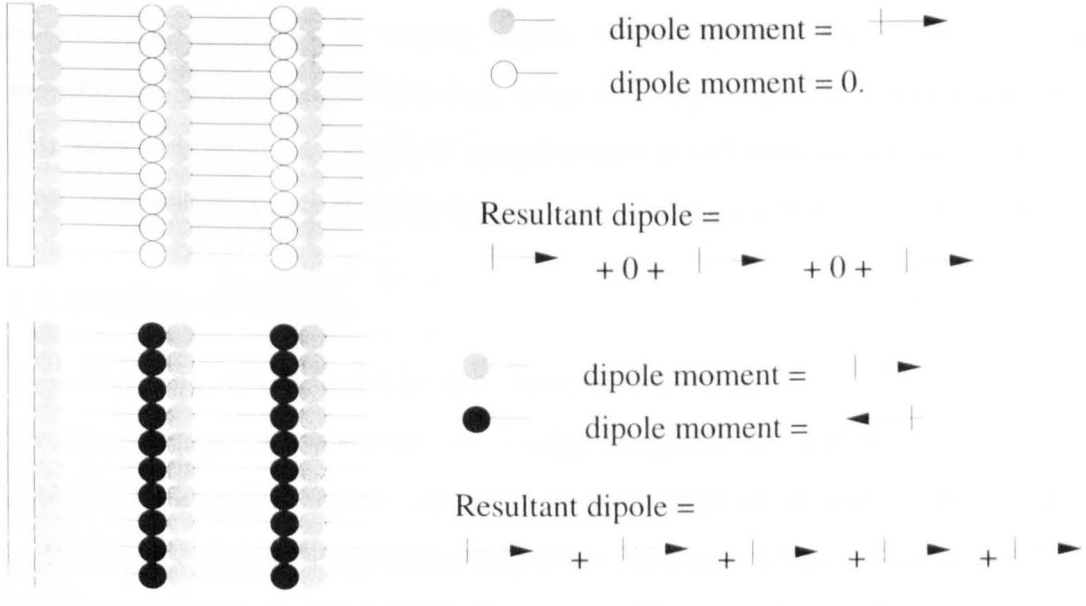

Figure 1.1 Schematic diagram of the two types of alternating LB films on hydrophilic substrates.

Obviously, the latter arrangement is the more desirable, since it gives the maximum possible resultant dipole. Such LB films are termed ABAB structures. Their potential is enormous in the field of opto-electronics, particularly communications or sensing, for the reasons given above.

Attempts to produce such films in practice, however, have been unsuccessful, and only very limited order has been observed [7]. This is thought to be a result of successive layers mixing with each other [8], a phenomenon known as scrambling, so that the molecules point in all directions, with only a random chance of a small resultant dipole. It is not yet understood whether this scrambling takes place at the moment of dipping [8] or while the substrate is under water in between dips [8]. The present project was therefore undertaken to clarify this, to investigate the scrambling mechanism and to establish ways in which it could possibly be avoided.

Previous work on the problem has used neutron reflectivity and deuterium-labelled layers [9] to study the mixing of each layer into the others, but only on ABAB or AABB films, so it was not possible to establish if individual layers mixed into those below, those above or both. The present project tackled the problem by labelling only one bilayer in each sample, at varying depths, thus simplifying the modelling required to interpret the neutron reflectivity data, since the simplest possible system has been used. The results from these fatty acid samples were tested with acid-amine films and then with more complex polysiloxane molecules, and the initial hypotheses were confirmed.

1.5 Outline of Thesis.

As a necessary starting point for this study, in order to place the present work in context, the current state of knowledge concerning Langmuir and LB films is summarised in Chapter 2. From this review, the range of parameters which were to be investigated in order to achieve a better understanding of the influence of film production techniques on the structure and properties of LB films is identified, and this is also given in Chapter 2. The chapter ends with an introductory discussion of previous work into the characteristics of LB films using X-ray and neutron reflectivity methods. The theory of these methods is given in more detail in Chapter 3, together with a discussion of the

various methods of analysing the data which are produced, to yield information on sample structure. The actual equipment used for the production of these films, and for their subsequent analysis by X-ray and neutron reflectivity, is described in Chapter 4, and results are given for the fatty acid films in Chapter 5 and for acid-amine films in Chapter 6. Chapter 7 gives the conclusions, including, *inter alia*, guidelines on how best to prepare films with the properties and unscrambled structure required for use in optoelectronic devices. Additional theory for SHG and pyroelectric effects is discussed briefly in the two Appendices.

1.6 References

[1] G.G.Roberts, Editor, Langmuir-Blodgett Films, Plenum (New York) 1990.

[2] I. Langmuir, J. Am. Chem. Soc., **39**, 1848 (1917).

[3] G. L. Gaines Jr., Insoluble Monolayers at Liquid-Gas Interfaces, Wiley, New York (1966).

[4] K. B. Blodgett, J. Am. Chem. Soc., **57**, 1007 (1935).

[5] K.B.Blodgett and I.Langmuir, Phys. Rev., **51**, 964 (1937).

[6] T. Moriizumi, Thin Solid Films, **160**, 413 (1988).

[7] M. R. Buhaenko, M. J. Grundy, R. M. Richardson and S. J. Roser, Thin Solid Films, **159**, 253 (1988).

[8] M. R. Buhaenko and R. M. Richardson, Thin Solid Films, **159**, 231 (1988).

[9] M. J. Grundy, R. J. Musgrove, R. M. Richardson and S. J. Roser, Langmuir, **6**, 519 (1990), and U. Pietsch, T. A. Barberka, U. Englisch and R. Stömmer, Thin Solid Films **284-285**, 387 (1996).

Chapter 2. The Nature of Spread and Dipped Films.

2.1 Introduction.

This chapter discusses the various factors which affect Langmuir-Blodgett (LB) film formation, such as the subphase conditions, monolayer state and monolayer treatment during dipping. It begins by describing in detail the individual film phases of a Langmuir film to facilitate an understanding, on both the molecular and macroscopic levels, of the importance of monolayer state on the subsequent structure of the LB film. In particular, monolayer viscosity is discussed as perhaps the most salient parameter to be considered in appreciating Langmuir and LB film behaviour. The chapter then reviews previous work on LB films, concentrating on the techniques and approaches which have been used to measure and characterise scrambling in LB films. Finally, it reviews the current theories on the causes of LB film scrambling, to place the present work in context.

2.2 Langmuir Films.

2.2.1 General Aspects.

An amphiphilic molecule is one with both hydrophobic ("water-hating") and hydrophilic ("water-loving") character. Typically, such a molecule has a hydrophilic head group and a hydrophobic tail, and its shape is therefore approximately cylindrical. An excellent example is a fatty acid such as docosanoic acid, whose structure is given schematically in Figure 1. The chain region of the molecule is approximately 27Å long, while the headgroup region is approximately 3Å long.

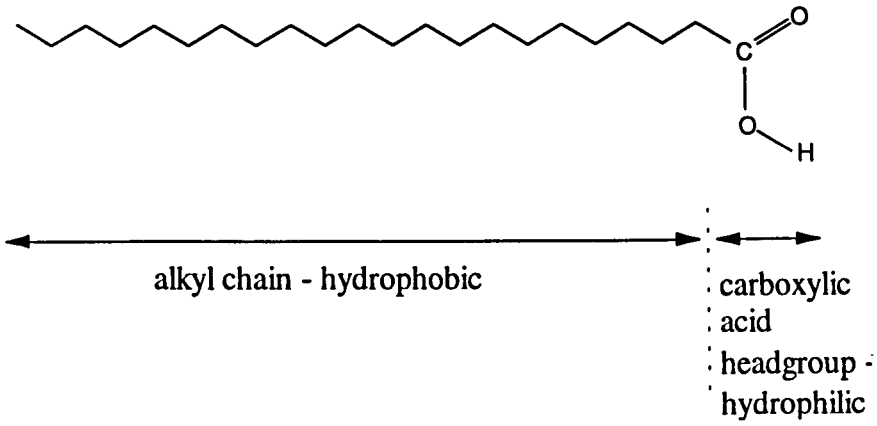

Figure 1. Schematic diagram of the structure of docosanoic acid, showing the two different regions of the molecule.

Molecules such as these spread spontaneously on a clean water surface, with the headgroup in the water and the tail away from the interface [1], thus reducing the surface tension γ or, conversely, increasing the surface pressure π:

$$\pi = \gamma_0 - \gamma$$

where γ_0 is the surface tension of the pure subphase.

Surface pressure is usually measured using the Wilhelmy plate technique [2], whereby the apparent buoyancy of a porous plate (e.g. filter paper), suspended from an analogue microbalance and partially immersed in the subphase, has a linear dependency on the surface pressure.

The surface pressure of the spread film can be manipulated by altering the area available using either rigid booms or continuous flexible barriers. If the area is reduced slowly and steadily, the pressure changes may be recorded against area and the resultant plot is known as a π - A isotherm ("isotherm" because the temperature is kept constant during a particular run). Some examples are shown in Figure 2.

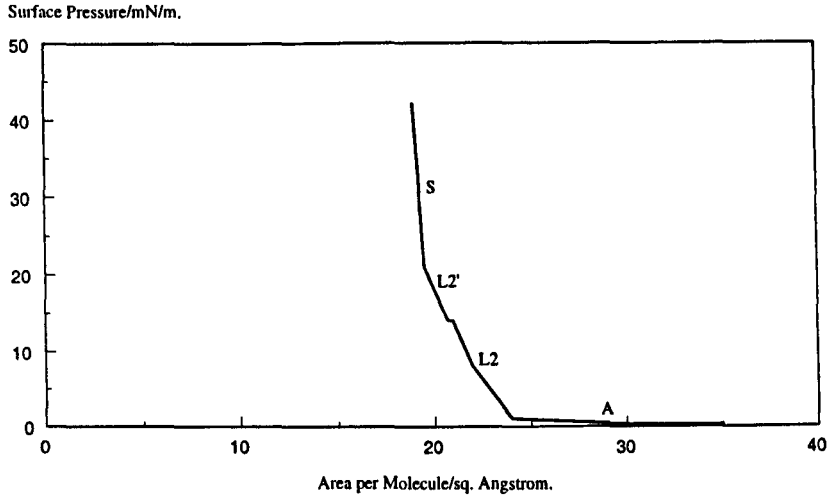

Figure 2 a)

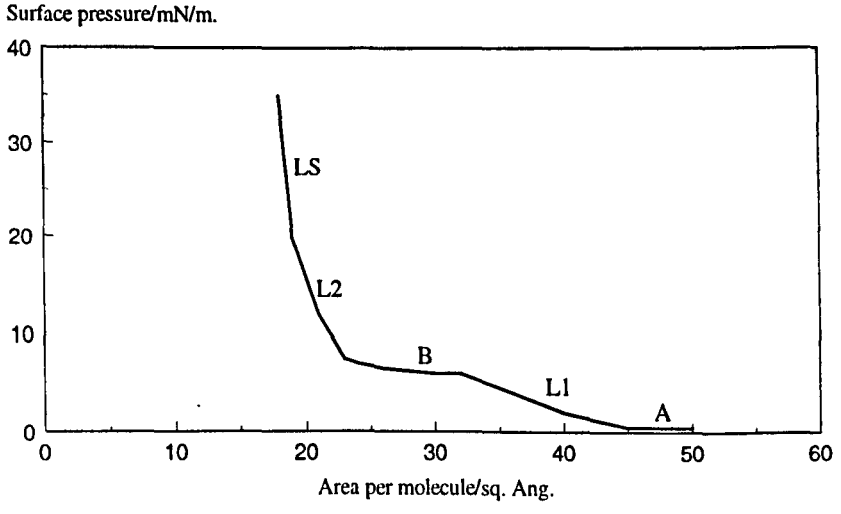

Figure 2 b)

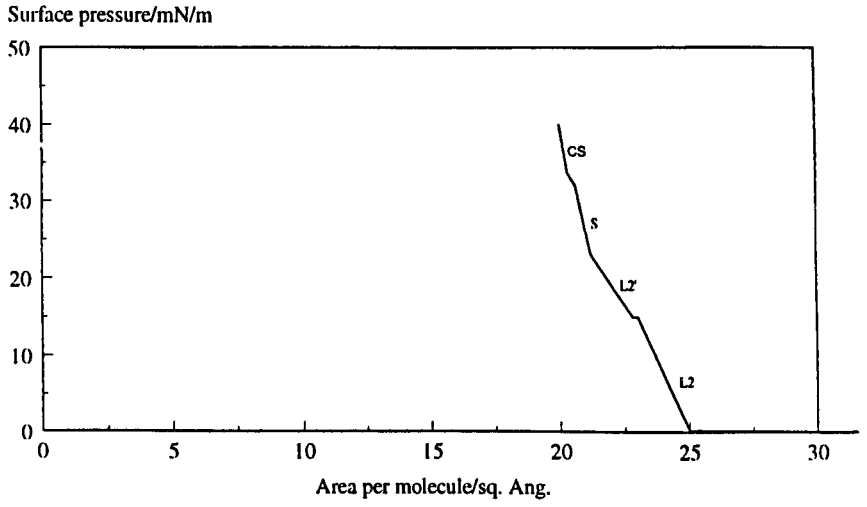

Figure 2 c)

Figure 2. π - A isotherms of a) docosanoic acid, b) pentadecanoic acid, both on pure water acidified to pH3 at 20°C, and c) docosanoic acid on pure water at pH5.5 at 20°C. The labelling of the various parts of the isotherms is discussed in the text.

It can be seen from Figure 2 that, whilst the two molecules show different isotherms in terms of changes in gradient and at what area or pressure these changes take place, they both show a region of low compressibility at low surface area, regardless of subphase pH. When extrapolated to zero on the pressure axis, this gives a value for the close-packed area per molecule (apm) of 20Å^2, which is the expected value for a carboxylic acid headgroup [2]. This confirms that the headgroup is in the water, with the rest of the molecule directed away from the interface. Thus it can be seen that the π - A isotherm provides ready access to valuable information at the molecular level.

The changes in gradient in the isotherm are indicative of phase changes, i.e. the packing of the molecules on the surface is being altered by the ever-decreasing area in a direct 2-dimensional analogy of the behaviour of the bulk material on compression. Much work has been done to explain the features of the isotherms of various molecules, in terms of molecular orientation and packing. Gaines [2] provides an excellent review of the initial work in this field, the chief conclusions of which were as follows. Note that

this is a very simple picture; it will be consolidated and brought up to date a little later in this discussion.

a) The monolayer is only truly gaseous at very large apm; in some cases this can be as large as 5000Å^2, for fatty acids it is ~ 400 Å^2.

b) At apm below this, but still in the flat zero-measurable-π region, the monolayer is historically referred to as "liquid-expanded" (l-e). It has long been regarded as an intermediate phase, where the molecular arrangement is not fixed and is constantly moving, in other words a very fluid phase. The molecules were historically regarded as lying flat on the subphase in this region, although it is now thought that they are approximately perpendicular to the subphase throughout the isotherm, from the largest apm to the smallest.

c) Once the pressure starts to rise, the isotherm shows a region of constant gradient, in the case of fatty acids up to ~ 20-25 mNm^{-1}. This was historically referred to as the "liquid-condensed" (l-c) phase, i.e. the molecules were regarded as being ordered compared to the liquid-expanded phase, but still with considerable freedom. It is comparable to a 2D smectic liquid crystal phase, in that all the molecules point in roughly the same direction, away from the subphase, but at a range of angles and with plenty of freedom to move in two dimensions. Nevertheless, since they are much closer together than in the liquid-expanded phase, a surface pressure is generated, which increases steadily as the apm is reduced.

d) Inevitably, a point is reached when the molecules are forced so close together that the random packing of a liquid is superseded by the ordered packing of a solid. The pressure continues to rise, as more and more of the monolayer adopts the close-packing, but it rises very steeply, since the already close-packed areas will naturally resist any further compression. The bulk pressure on a monolayer 30Å thick at 40mN/m is equivalent to approximately 133 atmospheres ($P = \pi/\delta$, δ is the monolayer thickness).

e) Finally, there comes a point where all the material in the monolayer has adopted the closest packing arrangement available to that molecule. If the monolayer is

compressed still further, the forces in the film, by now of the order of the 2D equivalent of 230 atmospheres, cause buckling and crumpling at any weak spots which are inevitably present in a crystalline structure. The monolayer becomes an uneven multilayer and is said to have collapsed.

Whilst this picture, as was stated earlier, is very simplistic, it will be seen to be readily analogous to the behaviour of fatty acids in the bulk. The packing at low π is dominated by the headgroups and in the liquid-expanded, liquid-condensed, solid and collapsed phases it is dominated by the packing of the hydrocarbon chains. This behaviour is analogous to that shown by similar molecules on heating, for example T_g marks the transition between different packing modes of the hydrocarbon chains. Therefore, as might be expected, monolayer packing is strongly susceptible to subphase temperature and these effects will be discussed in more detail shortly.

As will be seen in Chapters 5 and 6, some molecules, notably polymeric ones, form monolayers whose isotherms show none of these features. In this case, the size of the molecules, and the stoichiometry of the backbone and sidegroups, prevents them from adopting a truly close-packed arrangement, at least under the conditions available in a Langmuir trough, and the monolayer remains in a fluid phase (liquid-condensed) until it collapses into a disordered multilayer.

Other molecules, notably those with ring structures such as phthalocyanines, are prevented from adopting a fluid arrangement by their various pendant groups, and the monolayer is rigid (solid) throughout almost the entire π range of the isotherm.

To return to the discussion of fatty acids and their monolayer phases, the three basic categories described above (l-e, l-c and solid) are not able to explain the various "kinks" in the gradient within a particular isotherm region, nor the plateaux which are sometimes observed. Both of these are illustrated in Figure 2. The irreproducible nature of these features from worker to worker led to them being ascribed to impurities, either in the monolayer or the subphase. However, as techniques and materials improved, these features continued to be seen by increasing numbers of workers, and effort was devoted to studying and explaining them.

2.2.2 Current View of Monolayer Phases.

The culmination of this line of study was careful and detailed work by Bibo and Peterson [3] which, with scrupulous attention to purity of materials, has established what phases occur, dependant on molecular chain length and subphase temperature, and which built on the above 3-phase picture to include other phases, which explain the extra isotherm features consistently. The present discussion will use their terminology. Broadly speaking, at very low π, i.e. very high area per molecule, the molecule is in the gaseous state. At areas per molecule below about 100Å^2 (region A in Figure 2) it forms islands in the liquid state on the micron scale, surrounded by a clean water surface, with little interaction between them (i.e. a two-phase system). This arrangement holds until the area per molecule approaches 30Å, when the increasing proximity forces the molecules to adopt a closer packing. Brewster Angle Microscopy (BAM) [4] and glancing angle X-ray scattering [5] have been used to elucidate these packing arrangements and also, particularly BAM, to illustrate the two-phase regions of the isotherm. For instance, the islands mentioned above are known to be approximately circular for a straight-chain fatty acid at $\pi < 1$mN/m [4], and the packing within them is the same as for the L_2 part of the isotherm, i.e. the hydrocarbon chains are tilted at about 30° to the surface normal [5].

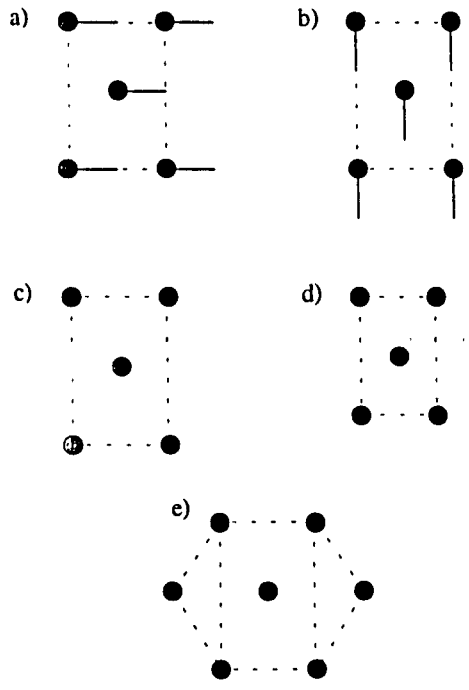

Figure 3 Schematic diagram of packing in a) the L_2 phase, b) the L_2' phase, c) the S phase, d) the CS phase and e) the LS phase, showing the differences in packing arrangements. Note especially that a) - d) show centred-rectangular packing, while e) shows hexagonal packing.

As the area is reduced still further, the tilt of the chains is reduced and in the L_2' region the chains are at an angle of about 15° [5]. In the S and CS regions the chains are vertical [5]. In all four of these phases the molecular packing is centred-rectangular (Figure 3). The only difference between the phases is the molecular tilt [3] and its direction [5]. For instance, note that in Figure 3a) the molecules are tilted towards their nearest neighbour and in Figure 3b) towards their next-nearest neighbour. For clarity, the angles of tilt have not been shown. In both the S [Figure 3c)]and CS [Figure 3d)] phases, the molecules are perpendicular to the surface; the difference between these phases is that, whilst the S phase has an area per molecule of 19.2Å^2, the CS phase, which is found only at lower temperatures, has an area per molecule of 18.7Å^2. In the LS phase, which is only observed in docosanoic acid at subphase temperatures above 25°C, but which constitutes

the entire high-pressure region in stearic acid isotherms at all temperatures between 10 and 30°C [3], the molecules are packed hexagonally, with the chains perpendicular to the surface [5]; this is illustrated in Figure 3e).

These workers [5] also used the evanescent wave, arising from an X-ray beam incident at a grazing angle below the value for total internal reflection, to investigate the in-plane features of these Langmuir films. They found that the peak width from the CS phase corresponded to order on the scale of more than 160 lattice spacings, whereas for the L_2, L_2', LS and S phases, the peak width corresponded to order on the scale of less than 54 lattice spacings. This is a significant difference in long-range behaviour, and implies that only the CS phase may be regarded as an ordered close-packed crystalline solid. The remaining phases correspond well with the various smectic phases of liquid crystals.

Considering Bibo and Peterson's work in more detail [3 and references therein], the effect of temperature on the monolayer must not be underestimated. The magnitude of this effect is in turn related to the length of the hydrocarbon chain of the acid. As illustrated in Figure 2, shorter chains, e.g. C_{14} or C_{16}, show different phases than do longer chains such as C_{18}, C_{20} or C_{22}, and the effect of temperature is therefore different in each case. For instance, the very short chain myristic (C_{14}) acid, which is incidentally the shortest that can form a monolayer without excessive dissolution into the subphase, shows the same phases at 13°C as does palmitic (C_{16}) acid at 34°C, namely L_1, L_2 and LS. In other words, the very short chain endows the monolayer with the degree of fluidity the slightly longer chain can only attain at a much higher temperature. Lengthening the chain further, to stearic (C_{18}) acid, the monolayer phases are different again and the L_1 phase is not present. Consequently, there is no plateau region in the isotherm as there is for the shorter-chain acids, and the isotherm is the simplest of all in this series of molecules, with only the A region, the L_2 phase and the LS (superliquid) phase. The presence of only this fluid hexagonally packed region at higher π is the most likely reason for the difficulty experienced by all workers in obtaining stable monolayers of stearic acid or the two shorter ones (C_{14} and C_{16}), and hence the subsequent difficulty

of dipping them as an LB film, without introducing ions into the subphase. The effect of such ions will be discussed later, in Section 2.2.4.

Continuing the homologous series still further, Bibo and Peterson found that arachidic (C_{20}) acid showed phases different from stearic acid, with the appearance of the L_2' phase at temperatures below 19°C, and that docosanoic (C_{22}) acid showed a still-wider range of phases, namely the S phase shown in Figure 2a). Their phase diagrams show that docosanoic acid has an L_2' phase at all temperatures between 9 and 28°C, although at the extremes of this range the phase is a very short part of the isotherm. In addition, at temperatures between 14 and 16°C, the S phase is also a very short part of the isotherm, being followed almost immediately by the CS (condensed-solid) phase. This last dominates the isotherm below 14°C, and at a subphase temperature of 8°C it is present at a surface pressure of only 10mN/m. This evolution of phases with temperature serves to illustrate the effect of chain length and temperature on the packing of the monolayer: short chains and high temperatures lead to the formation of more loosely-packed films, whilst long chains or lower temperatures enable more close-packed films to be formed. In other words, the high surface pressure phase varies according to temperature or chain length. These results are summarised in the phase diagram shown in Figure 4.

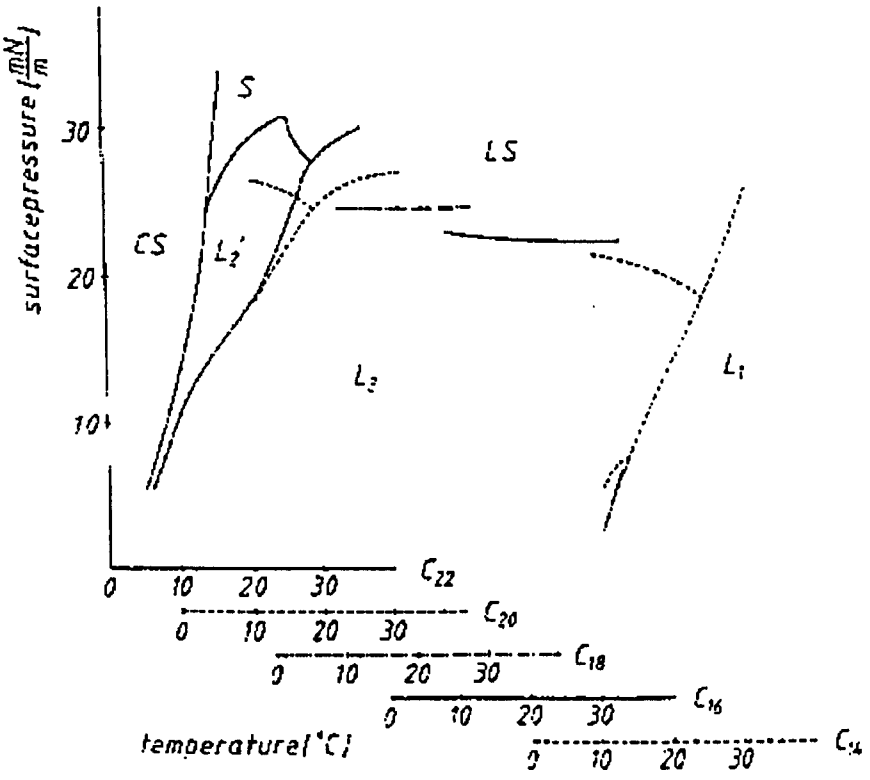

Figure 4 Superimposed phase diagrams of five fatty acids, with temperature scales shifted relative to one another as follows: C_{22} - C_{20} 10°C; C_{20} - C_{18} 13°C; C_{18} - C_{16} 16°C; C_{16} - C_{14} 20°C. Diagram from Bibo and Peterson, [3].

2.2.3 Monolayer Flow and Viscosity.

Each of the phases discussed above will naturally exhibit differing bulk properties, reflecting the differing molecular arrangements within them. Of these, viscosity is perhaps the most important for LB film preparation, since it will be the determining factor in how well the monolayer is transferred onto the substrate.

Talc has been used to illustrate the presence and flow of a monolayer right from the earliest days, but only as a crude indicator. Initial qualitative work by Daniel and Hart, and later Malcolm, investigated monolayer flow on compression and during dipping. Daniel and Hart [6] devised a simple technique to illustrate monolayer flow onto a substrate during dipping, by distributing small (4mm) PTFE discs over the monolayer surface in a grid formation prior to starting to dip. Photographs throughout the dipping

process illustrated the flow of the monolayer onto the substrate. The idea has been extended by Malcolm [7a, 7b], who used sulphur powder to form the grid. As this material is less dense than PTFE, and since it is also easy to form lines rather than a series of points, the technique enables yet clearer visualisation of the monolayer flow. Malcolm took the work further by designing a parallelogram-shaped trough in which the sides moved parallel to the direction of monolayer flow revealed by the grid of sulphur powder, thus reducing the monolayer distortion resulting from drag along the trough sides [7c].

These two pieces of work show that, at least on the scale of a 1cm grid, a monolayer moves as a sheet during dipping, with shear and compressional forces acting as far away as 5cm from the moving substrate. This vivid, if arguably crude, visualisation gives a readily accessible broad-brush picture of what is happening to the monolayer. Buhaenko et al. [8a-c] carried out more quantitative studies and examined the variation in viscosity of monolayers of docosanoic acid and a few other materials with surface pressure, subphase pH, subphase temperature and subphase cations. Their main conclusion was that, as might be expected, a monolayer becomes more viscous as surface pressure is increased, reflecting the ever-closer packing. Conversely, reducing the pH (and hence reducing repulsion between neighbouring COO^- headgroups) or increasing the temperature both make the monolayer more fluid.

These authors used both canal viscometry and an oscillating knife-edge bob to measure the surface viscosity of a range of fatty acids (C_{17} - C_{26}, [8a, 8c]), and later studied a variety of other materials [8b, 8c] using relaxation and resonance techniques. In addition [8b], they used a transducer to measure the forces acting during LB deposition, and this work will be discussed in Section 2.3. Their experimental conditions, of pure fatty acid over pure water acidified to pH3, are the same as those used in the present work, although beyond this direct comparison is difficult, since they measured surface viscosities only up to 30 mNm^{-1}, and the present work used surface pressures up to $40mN/m^{-1}$. In addition, the dipping speeds they investigated were of the order of 120 times faster than the fastest used in the present work. Nevertheless, their conclusions are extremely useful, because they aid the understanding of monolayer behaviour in the

work done up to 30mNm^{-1}. Firstly, they found that η^s (the surface viscosity of a monolayer) was independent of π for acid monolayers in the L_1 and L_2 phases, suggesting Newtonian behaviour, i.e. the viscosity is independent of shear rate. Thus, acid monolayers in these phases are truly fluid and able to flow readily. η^s for docosanoic acid in these phases is between 5.9 - 7.8 x 10^{-4} SP for $\Delta\pi$ = 5 mNm^{-1} , and ~12 x 10^{-4} SP for $\Delta\pi$ = 10 mNm^{-1}. However, above the L_2' $\rightarrow$ S transition, i.e. above π $\approx$ 30 mNm^{-1} for docosanoic acid, the monolayer becomes non-Newtonian, deduced from the fact that the viscosity could not be measured using these techniques.

$Log_{10}\eta^s$ was found to increase linearly with n, the number of hydrocarbons in the chain, and this is explained in terms of increased cohesion between the chains in a two-dimensional system such as a monolayer. They also found that a large contribution to η^s is made by the hydrogen-bond interaction between the headgroup and the subphase, based on their investigation of η^s with T, directly in line with Bibo and Peterson's findings on the effect of T on the phase changes revealed by isotherms [3]. The magnitude of this effect is of the order of a 50% reduction in η^s (12.3 x $10^{-4} \rightarrow$ 6.1 x 10^{-4} SP) on raising T from 19°C to 30°C, for docosanoic acid at pH3.

In the course of this work on viscosity, Buhaenko also studied monolayer stability [8c]. The chief findings of relevance to the present work were in relation to docosanoic acid and stearylamine. Specifically, a docosanoic acid monolayer, pH3, π = 35 mNm^{-1}, loses only 8% of its area over a period of ~80 minutes. At pH5.60, with no subphase ions, the area change was <5% over 60 minutes. For the amine (two CH_2 units shorter than the eicosylamine used in the present work), the figures were 12% of area lost over 72 minutes at pH5.5, and 9% over 130 minutes on pH2.84. Since the oldest monolayers used for dipping in the present work were only 32 minutes old (5 mm/min dip speed x 4 cm dip length x 4 dips) before the monolayer needed replenishing, Buhaenko's data fully support the π and pH values used here.

2.2.4 The Effect of Subphase Cations.

Introducing subphase cations such as Cd^{2+} has a marked effect on the behaviour of a Langmuir film. For instance, the isotherm of docosanoic acid is altered (Figure 5) in such a way that the L_2 and L_2' phases are much less obvious and the transition to the S phase occurs at a much lower surface pressure than over pure water.

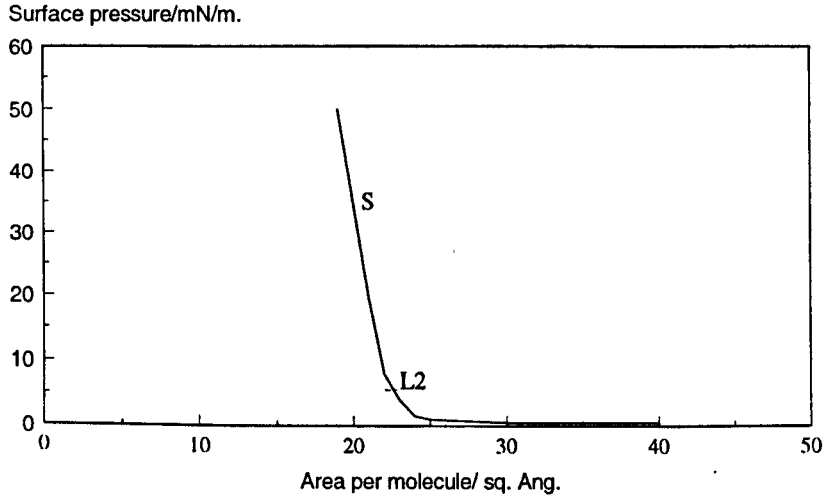

Figure 5 Isotherm of docosanoic acid on a subphase containing 0.25 mM cadmium chloride, 20°C, pH6.3.

The reason for the earlier onset of the S region in Figure 5 is that the Cd^{2+} ions each require two carboxylate ions for electrical neutrality, thus drawing the molecules of the monolayer closer together even at low surface pressures. At pH below 4.8, however, this effect is over-ridden by the pH effect mentioned earlier, whereby H^+ ions screen the headgroup charges, and the cadmium soap is not formed [9].

From these considerations it will be clear that even a "simple" fatty acid monolayer is a complex system and the various parameters must be carefully chosen if the monolayer is to have the required properties for successful manipulation into an LB film. In addition,

attention must always be paid to the phase of the monolayer, since this will ultimately be the single most important factor affecting the structure of any LB film dipped subsequently. Since the phase of the monolayer is necessarily affected by a variety of experimental conditions, and in order to make a rigorous study of the effect of varying each parameter that affects the monolayer, the samples in the present work were prepared at different surface pressures, different pH, different temperatures and either with or without subphase cations, and only one parameter was varied at a time, while the others were kept constant. The parameters were carefully chosen by this author to cover as wide a range of experimental conditions as possible in the time available, in order to ensure a thorough and rigorous approach to addressing the problem of scrambling in LB films.

2.3 Langmuir-Blodgett Films.

2.3.1 Introduction.

Building up multilayers by successive transfer of Langmuir films onto a solid substrate was first described by Blodgett in 1935 [10]. The principle is extremely simple and elegant. Figure 6 illustrates the process schematically:

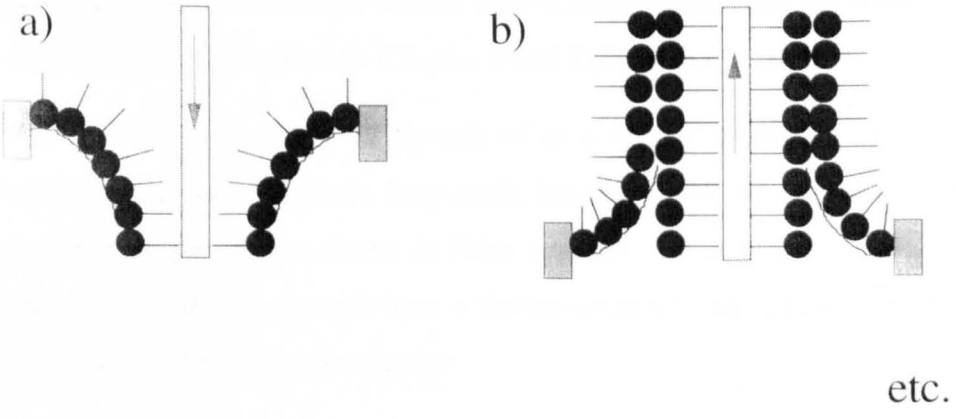

Figure 6 Showing the principle of Langmuir-Blodgett (LB) deposition onto a hydrophobic substrate

Quite simply, the substrate to be coated is passed vertically, at an even rate, through the compressed Langmuir film and a one-molecule-thick layer is deposited with each pass through the interface. The pressure of the Langmuir film is monitored using a Wilhelmy plate and kept constant via a feedback loop (for further details see Chapter 4). If the trough has its water surface divided into two compartments, separated by a suitable gate to avoid mixing of the monolayers, alternating ABAB structures may be readily prepared by moving the sample between the compartments as required, either under water or in the air. Deposition of the monolayer on both down- and up-strokes is known as Y-type dipping. Monolayers which only transfer on the downstroke are known as X-type, while those which only transfer on the upstroke are Z-type [2]. The present work is solely concerned with Y-type dipping.

The change in area of the monolayer on the water is easily measured for each dip stroke and, ideally, should equal the immersed area of the substrate, i.e. the transfer ratio should be 1.0, thus providing a rapid measure of LB film quality. In this work, however, the transfer ratio could not be accurately calculated because the rear face of the substrates used was very rough. Whilst there is evidence that a dipped monolayer can bridge defects due to surface roughness on the Ångstrøm scale [2 and 11], it is unlikely that macroscopic features can be bridged. Therefore, transfer ratios were used here simply as a measure of *relative* quality between layers and between samples, since all the substrates used were similar silicon wafers. Further details of the transfer ratios from this work are given in Table 4 in Chapter 5 and Table 4 in Chapter 6.

The deposited film must be thought of as a crystal. There are three well-known bulk crystal phases of long-chain fatty acids, labelled A, B and C [16]. The repeat distances within these phases are shown in Table 1 below. These three phases only occur in even-chain acids; odd-chain acids have a further three different phases, namely, A', B' and C'. These will not be discussed further.

Acid chain length	Phase A/Å	Phase B/Å	Phase C/Å
C_{18}	(not found in lit.)	43.8	39.9
C_{20}	52.5	48.4	44.1
C_{22}	56.2	53.0	48.2

Table 1. Showing the repeat distances in the three phases within the bulk crystals of three even-chain fatty acids.

von Sydow [17] noted that the phase formed depends on the crystallisation route, and more than one phase may be formed together. The factors affecting crystallisation are temperature, purity, rate of crystallisation and solvent used. For example, crystallisation from the melt gives the C form, which also forms on rapid crystallisation from solution; the B form crystallises slowly from solution, while forms B and C may be obtained as a mixture from solution in petroleum. Both B and C forms have orthorhombic packing. The C form is the most stable at room temperature.

2.3.2 Dipping Speed.

The dipping speed used for LB deposition has not received much systematic attention to date. Blodgett [10] found that the first layer needed to be dipped "fairly slowly (5 to 10 cm/min)" for satisfactory drainage to occur, whereas subsequent layers could be deposited at speeds of the order of 25-37cm/min. This was based solely on observations of drainage during dipping, since subsequent characterisation of the films optically [12] and using X-ray diffraction [13] showed they consisted of ordered layers. Chollet and Messier [14] studied docosanoic and 22-tricosenoic acids using X-ray and electron diffraction and infrared spectroscopy and found that LB films of these molecules were formed of adjoining crystallites, of maximum size 100μm. Because of its terminal double bond, and hence its different packing in the monolayer, 22-tricosenoic acid forms more fluid monolayers than docosanoic acid does. These workers [14] found a

correlation between this increased fluidity and increased anisotropy in the LB film, both in-plane and between layers, compared with docosanoic acid, when both were dipped at 30mN/m (at this π, docosanoic acid is in the S phase, whereas 22-tricosenoic acid is still in the L_2' phase).They used speeds of between 0.1 and 5 cm/min, but do not state anything more specific. Nevertheless, these speeds cover a slower range than those used by Blodgett [10].

Peterson and Russell [15] used polarising microscopy and electron diffraction to study structure further. Their results substantiate those of Chollet and Messier [14] and show that the crystal packing of the first layer determines the packing of subsequent layers, hence the desirability of using a single crystal substrate, such as a silicon wafer.

Closely linked with dipping speed is the effect on the already-dipped LB film of different times under water during subsequent dips. Obviously, a fast dipping speed will result in shorter times under water between dips than will slower speeds. Any effect would be exaggerated by deliberately leaving the sample under water for, say, 10 minutes or more between dips. The nature of the dipped film was observed to change by Blodgett in 1935 [10] and she established that the poor quality of some films was a direct result of the time spent under water, all other conditions being equal. Following initial attempts by Langmuir [18] to explain the deposition of some materials on the downstroke only (X-type) in terms of overturning of molecules under water, Hönig [19] proposed a mechanism showing that the energetics were feasible for half of the X-type layer to overturn under water and form a Y-type film covering half the substrate. Overturning on this scale is required in order to explain two decisive experimental observations. The first is that X-type films have very nearly the same X-ray diffraction repeat distance as Y-type films [20], i.e. twice the molecular length. This is surprising for a film which dips only on the downstroke and which would therefore be expected to have a repeat distance of only one molecular length. The second observation is that X-type films are hydrophobic on the surface, as are Y-type films [10]. Dipping only on the downstroke would, in theory, result in an LB film with the headgroups to the outside, which would be hydrophilic. Therefore, an explanation is needed which takes account of these observations. Overturning of molecules under water answers both, but the various

mechanisms proposed did not take energetics into account. Hönig's proposal of half the molecules overturning under water and attaching themselves head-to-head with the half that stays put means that the surface would be hydrophobic, which would explain why no pick-up occurs on the upstroke, and it would also explain why the films have a repeat distance the same as a Y-type film of the same material. The vacancies left by the overturned molecules in their original layer might then be filled by molecules from the next dipped layer, resulting in a very uneven structure. If less than half overturned, some pick-up would occur on the upstroke and a mixed X-Y film would result, again with a very uneven structure. This would explain Blodgett's observation [10] that film quality deteriorated with the number of dips. Also, Hönig's theory would predict that a longer time under water would allow more overturning to occur, resulting once more in a very uneven structure.

The energetics of overturning depend on the relative strengths of the following interactions: tail-tail, head-head, tail-water and head-water. The energies of these interactions may be expressed as ε_{tt}, ε_{hh}, ε_{tw} and ε_{hw}. If the sum

$$\varepsilon_{tt} - \varepsilon_{tw} + \varepsilon_{hw} - \varepsilon_{hh} \qquad (2.1)$$

is positive, the film will be X-type; if negative, Y-type. Thus, an overturning layer is explained by considering a film which dips X-type, i.e. for which the sum in Eq. 2.1 is positive: the tails are more strongly attracted to other tails than to water, while the heads are more strongly attracted to water than to other heads. Thus, the head-head attraction between neighbouring molecules within the plane of the downstroke layer is weaker than the attraction of the heads for the water, so any which are not completely surrounded by fellow molecules within the plane of that particular layer, either at the edges of the substrate or due to uneven deposition, can detach themselves while the substrate is under water. These detached molecules, freely moving in the subphase, now have their tails surrounded by water on all sides, which is not energetically favourable, so they readily turn over and redeposit head-head on the substrate, either immediately on top of their original layer or to fill in holes in a previous uneven layer, so as to surround their tails by other tails. This then alters the nature of the outermost surface of the film from hydrophilic to hydrophobic, and no material is deposited on the upstroke: an X-type film

results. For a film which dips Y-type, the head-head interaction dominates the four terms to render the sum of Eq. 2.1 negative, the molecules remain firmly bound within the layer in which they were dipped and deposition occurs in both directions. The energies involved are typically a few kT. The equation given also explains the differences Blodgett observed [10] with changes in ionic strength and pH, as these would affect the ε_{hw} and ε_{hh} terms. Because this theory answers all the observations satisfactorily, it has long been regarded as the best explanation of what happens during the LB dipping process. The present work adds an extra dimension, in terms of the requirement also to consider the phase the Langmuir film is in during dipping.

Hönig went on [21] to try to quantify the effect of time under water on this overturning mechanism, using as a starting point the results of Peng et al. [22], which showed a close correlation between time under water and the extent of X-type behaviour. Based on the SEM micrographs taken by Peng et al., which show X-type films to be very uneven, Hönig proposed that this unevenness itself affected the degree of X-type behaviour in an autocatalytic fashion, i.e. the more irregular the surface, the easier it would be for molecules to overturn. Hönig's mechanism influenced thinking towards minimising the time under water, i.e. increasing the dipping speed, to minimise the chances of this under-water scrambling taking place. However, scrambling could still not be eliminated, so it is clear that other mechanisms are involved. Therefore, the present work investigated the effects of time under water and dipping speed.

With Hönig's mechanism in mind, Buhaenko et al. [23] and Grundy et al. [24], *inter alia*, prepared LB films with alternating ABAB or AABB structures, in order to investigate the scrambling effect and the influence of time under water. However, because of the repeating nature of their samples they were unable to establish conclusively whether molecules mixed into the layer above or into that below. Their work will be discussed more fully in section 2.4. In another paper [25], Buhaenko and Richardson investigated dipping speed more thoroughly, using the measurement of contact angles and of the force of emersion and immersion. Contact angles were recorded photographically, and a transducer was used to measure the forces. Samples were prepared on hydrophobed glass. Films were eicosanoic (C_{20}) acid dipped at

30mN/m over subphases containing 0.3mM $CdCl_2$, with the pH ranging from 2.4 to 6.0, i.e. pure fatty acid to mixed acid/salt films. The forces measured were in the range 30-50mN/m. They found that the force increased with pH, so it is sensitive to increased ion binding and hence film viscosity [8]. In addition, subphase ions increase the viscosity of the subphase, and the ion concentration immediately beneath the monolayer will increase with pH, due to increased binding to the headgroups. This would make the subphase more difficult to expel at the three-phase contact line, and hence increase the force of emersion.

The dipping speed used also affected the force of emersion: between 6 and 60mm/min, the force increases rapidly with speed, with the increase slowing down above 60mm/min. This suggests a critical speed above which the meniscus moves faster than the monolayer can adsorb onto the substrate. The critical speed, U_{crit}, marks this transition between reactive and nonreactive dipping. Reactive dipping means the monolayer is spontaneously adsorbed. Non-reactive means the monolayer is forced onto the substrate as a result of its rapid withdrawal; this traps the subphase, which would normally drain away, and this in turn increases the force measured since it introduces extra viscous drag. An alternative explanation is that a high monolayer viscosity would give rise to a drop in π near the point of deposition, since the monolayer would not be able to flow to replace that which had just been taken up by the substrate. This would render the monolayer inhomogeneous at high dipping speeds. This author favours the latter interpretation.

U_{crit} is not to be confused with the highest speed at which a substrate may be withdrawn dry. For acid films, this is of the order of 1800mm/min; for salt films, of the order of 1080mm/min.

Buhaenko et al. [23] also found that below U_{crit}, the reactive deposition that occurred appeared to lead to a mixing up of A and B layers, but they point out the preliminary nature of their results and the need for further work. Their conclusion is that a higher U_{crit} indicates greater attraction between headgroups on the substrate and in the monolayer, thus increasing the likelihood of good deposition.

2.3.3 Contrast Between Acid and Salt Films.

It must be pointed out that nearly all the work described above was done using fatty acid salt films, since pure fatty acid films were thought to be difficult and irreproducible to dip. For instance, at pH7, Peng et al. [22] were unable to dip more than one layer of stearic acid at all. In fact, this bias towards salt films shows a failure to appreciate and take account of headgroup/water interactions and the screening effect of low pH [9], and the present author considers that more work needs to be done on plain fatty acid films, to increase our understanding of these simple systems, before complexities such as metal ions are introduced. Hence, in the present work, only two samples were dipped over a subphase containing metal ions, allowing an objective comparison to be made between the present experimental techniques and those of previous workers, and the remainder were pure fatty acid films dipped over water at pH3, where all the headgroup charges are screened by H^+ ions and the monolayer is stable.

Buhaenko et al. [23] also found that acid films have the greatest attraction between the headgroups and hence the highest U_{crit}, while salt films have the least headgroup attraction and hence the lowest U_{crit}. This result fully supports the present approach to the merits of studying pure acid films.

2.3.4 Summary of Dipping Parameters.

Given the above considerations, therefore, in this present work samples were dipped not only at different speeds, but also with only one bilayer of the labelled ("B") material within the overall structure. The position of this B bilayer was also varied, from the substrate interface to the centre of the sample to the air interface, in order to elucidate just where the scrambled molecules come from and go to. The effect of 10 minutes under water was also investigated, bringing the total number of parameters varied in monolayer formation and dipping to seven (dipping pressure, subphase pH, subphase ions and subphase temperature have already been mentioned), although due to time constraints the complete matrix of possible samples could not be prepared and studied. Chapters 5 and 6 list the two series of samples prepared and studied in this work.

2.4 Characterisation of LB Films.

The most fruitful methods of studying order on the molecular scale within organic systems are X-ray and neutron reflectivity. The great advantage of these techniques is that the supporting substrate can be readily accounted for and hence excluded from the analysis. A brief resumé of these techniques and the information they can yield will be given here, and a more detailed description of the theory and practicalities will be given in Chapters 3 and 4. Both techniques rely on exactly the same physics as that which causes white light to be split into its component colours by a thin film of petrol on a puddle of water, namely refractive index variations and the interference resulting from differences in path length between waves reflected from the top surface of the film and those reflected from within the film or from the substrate.

X-rays are susceptible to the electron density gradients within a structure, whereas neutrons are affected by nuclear scattering length density gradients. These are analogous to the refractive index changes that a material presents to light. The scattering length that a material presents to neutrons may be described as the extent to which the nuclei of that material divert the neutrons from their incident path; the electron density of a material affects X-rays in the same way. However, whilst electron density varies linearly and predictably with the number of electrons, i.e. with atomic number (e.g. for H, the X-ray scattering length is 2.8×10^{-5}Å, for D it is the same since the atomic number is the same, and for C it is 16.8×10^{-5}Å), neutron scattering lengths are rather more random. The particular usefulness of neutrons for the study of organic systems arises from the fact that hydrogen and deuterium have very different scattering lengths (H -3.73×10^{-5}Å, D 6.67×10^{-5}Å, C 6.65×10^{-5}Å), and so by simply deuterating one type of molecule or part of a molecule in the system under study, one can use neutron techniques to access very detailed information on the structure being investigated.

As mentioned in the previous section, X-ray diffraction work has established that LB films are planar in structure, with the chains and headgroups in ordered layers [13]. The various crystal phases already discussed have been observed and are ascribed to the method of formation of the initial Langmuir film as much as to the dipping conditions

used [26]. Subphase cations are known to affect the tilt angle of the molecules within the dipped film, since samples prepared over a calcium solution, for instance, have a larger repeat distance than those dipped over plain water [13], i.e. the salt molecules are tilted less. However, by its very nature, X-ray reflectivity is unable to provide information on inter-layer mixing. It is, nevertheless, a very useful technique and complementary to neutron reflectivity, because the information it provides about film thicknesses and repeat distances greatly simplifies the interpretation of neutron data.

Neutron reflectivity has been applied to many LB film systems in an attempt to understand the inter-layer scrambling that is observed, and systems using deuterated and protonated fatty acids have been more popular than those using the active molecules that might be used in a commercial application. This is chiefly because the former have been perceived as easier to model, but also to attempt to establish the mechanisms involved in scrambling by simplifying the system under study, prior to moving on to commercial and more complex molecules.

Brief reference has already been made to the initial work in this field by Buhaenko et al. [23]. They used neutron and X-ray diffraction to study cadmium docosanoate LB films, dipped under a variety of conditions, to investigate changes in structure and how these were affected by temperature. Using X-ray diffraction, they found that pure acid films deposited in the B form, i.e. with a 53Å repeat, and that this changed to the C form, i.e. with a 48Å repeat, at 55°C. Pure salt films were found to deposit with the chains perpendicular to the substrate, i.e. with a 60Å repeat, and retained this structure up to 90°C. Mixed films [9], dipped at pH5.3, were found to deposit with both 58 and 60Å repeats, and the 58Å phase disappeared as the temperature rose. Silicon wafers were found to be the best substrate in terms of subsequent film quality and order, compared with di-methyl or tri-methyl silanised glass, and this is perhaps not surprising, given the increased order found on the single-crystal face of a wafer, compared with the large defect densities of a glass surface [27].

2.4.1 Previous Work and Current Theories on LB Film Scrambling.

Using neutron diffraction, Buhaenko et al. [23] studied films of alternating hydrogenous and deuterated cadmium docosanoate, either as HHDD or HDHD type. For pure acid films, the HHDD structure showed a repeat of 105Å, and the HDHD structure a repeat of 52Å. Both structures showed only a repeat of 60Å in pure soap films, and the reasons for this were not clear. Mixed films showed a 59Å phase, and the instrument resolution was not good enough to resolve if this was the 58 or 60Å repeat. As they increased the temperature, they found the acid film structure disappeared at T > 60°C, whereas the soap structure peaks simply broadened, at T > 90°C. They were hoping to use the presence of deuterated material to establish whether these phase changes are caused by diffusion of bilayers or of single molecules, but were unable to ascertain the mechanism by which the phase changes occur. All their samples were dipped at 120mm/min, except for one at 10mm/min to investigate the effect of dipping speed. There was a variation in peak intensities with dipping speed, but they regarded their results as inconclusive with regard to the effect of speed on film quality. A sharp, intense peak would indicate that the H and D layers had not intermixed and that the D-acid remained in the single layer or bilayer in which it was dipped. A broad, shallow peak would indicate the D-acid had mixed with one or other, or both, of the surrounding H-acid layers, according to the theory put forward by Hönig [19], thus rendering the D/H boundary somewhat blurred. A fast speed of 120mm/min gave a sharper peak than a slow speed of 10mm/min. They concluded, as has been mentioned, that a fast dipping speed was required to maintain order in a film dipped at 30mN/m, and this supported the theory on the effect of time under water. Grundy et al. [24] confirmed this result.

It must be pointed out, however, that these experiments again used a Cd^{2+} subphase at pH6.2, which gives a pure salt film. No critical speed was observed by Buhaenko et al. [25] for a pure acid film, and this author concludes that the phenomenon of critical speed is linked to the increased viscosity and generally different phases of salt films, and as such is of limited relevance to the acid films studied in the present work.

Musgrove [26] studied the different crystal phases that occur in fatty acid and salt LB films, as well as order in ABAB films, but the experimental details of the LB film preparation are unfortunately not given in sufficient detail to be sure of consistency. Various other attempts have been made to measure the extent of scrambling, but all to date have used ABAB and salt films. Indeed, the approach of some authors is, surprisingly, that scrambling is inevitable and that it is therefore a useful tool to show the sensitivity of their techniques. The most important of the work which has been carried out in an attempt to shed light on the problem of LB film scrambling is now reviewed.

In an elegant experiment, Pietsch et al. [28] used Mg to label one headgroup region in a multilayer film of lead stearate, and investigated the structure using X-ray reflectivity. They found that the position of the Mg layer, a region of about 2Å thickness, could be pinpointed with an accuracy of between 1 and 3Å, depending on the position of the layer within the film "sandwich": it was easier to pinpoint the layer if it was at the air or the substrate, than if it was in the centre of the sandwich. Interestingly, they also found that thicker films have a more disordered top layer, and that this top layer was often apparently thinner than those below. They explained this apparent thinness in terms of the reduced density of the top layer, which would reduce its effective scattering intensity. This result is in line with Hönig's theory that overturning becomes worse in thicker films [19 and 21].

Englisch et al. [29] used both X-ray and neutron reflectivity to study HHDD films of lead stearate on silicon wafers. They used a π of 25mN/m and a speed of 6-10mm/min. The pH of 6.9 means that the film was entirely salt [9]. They found that the CH_3-CD_3 interfaces were blurred, either through diffusion or through exchange of complete molecules. The extent of exchange was 20%, and this increased as films became thicker. The fuzziness could be explained by holes appearing in each monolayer after dipping, which would then be filled by the next layer to be dipped. This is illustrated in Figure 7. In order to establish whether this is in fact the case, an accurate measure of the deposition ratio would be required.

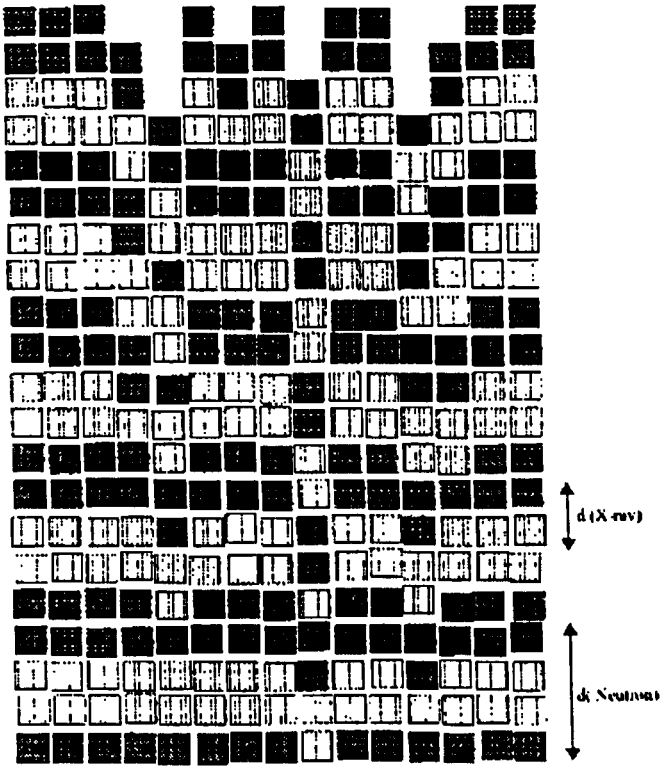

Figure 7 Diagram illustrating the mixing of D molecules (lighter squares) into preceding imperfect layers of H molecules (darker squares) and *vice versa*. The repeat distances for the two techniques are indicated on the right of the diagram. The substrate is at the bottom. From Englisch et al. [29].

Alternatively, the apm might change, and this theory is supported by the work of Tippmann-Krayer et al. [30], who found firm evidence for a reduction in apm between cadmium arachidate monolayers on water (19.7Å^2) and in the dipped film (18.2Å^2), due to a rearrangement of the chains from hexagonal to orthorhombic packing. The deposition ratio remained unity. This was, however, observed for cadmium arachidate, and the present author has not found evidence in the literature for a similar experiment involving a pure acid film. Given the differences in phase behaviour between salt and acid films, due to the headgroup binding induced by the metal ions, it would seem reasonable to assume that this rearrangement to a smaller apm. does not necessarily occur on dipping an acid film. This could be an avenue for further research. Indeed, in

the present work, neutron and X-ray data revealed molecules in individual layers to be tilted at 23° to the surface normal, implying that, in acid films at least, the phase change on dipping is one of relaxing to a less close-packed phase, namely from the S phase to the L_2 phase (see Chapter 5, Section 5.5.1). This is in direct contrast to the observations described above for salt films, once again emphasising the need for further study of acid films.

Vierheller et al. [31] also found H and D intermixing of the order of 20%, in samples with six H layers followed by six D layers. As well as D molecules having filled holes in the H layers below, they also found H molecules within the top six D layers, suggesting a very high molecular mobility. With reference to Grundy et al. [24], they explained this in terms of the length of time their samples spent under water, which was between 10 and 20 minutes for each dipping cycle. After heating at 70°C for 600+ mins, they found that some D molecules had diffused right down through the film to the silicon substrate. Heating at 84°C for a week resulted in the loss of most of the H/D contrast, due to almost complete mixing of the H and D molecules.

Englisch et al. [32] used mixed acid/salt films of stearic acid/barium stearate at pH 6.3, 41mN/m and at 10mm/min. Again, they found an initial D/H exchange of 25%, similar to that found by Vierheller et al. [31]. This proportion increased on heating, to 35% at 65°C and 50%, i.e. no H/D contrast, at 90°C. Since they used a mixed film, there are free acid molecules in the dipped film which are unbound by the metal ions, and these are therefore free to move within the lattice. They needed 33% free acid to explain their results, although this seems an improbably high proportion at pH6.3 [9].

2.4.2 Summary.

It will be clear from the above review that the vast majority of work to date has used fatty acid salts and there is thus a gap in our knowledge of pure fatty acid systems, which the present work is designed to address. Despite the apparent coherence between all these results and the conclusions drawn from them, it must be stressed that none of the above arguments has so far enabled a distinction to be made between a layer mixing into the layer below, the one above, or both, and it would clearly be difficult to establish this

for sure with ABAB films. Hence, in this work, only one layer was labelled. Nor has it been possible so far to produce truly ordered alternating LB films. Some explanation for this is provided by the work of Tippmann-Krayer et al. [30], mentioned above, who found firm evidence for a reduction in molecular area on transfer of a monolayer from water to a solid substrate. Given that the transfer ratio remains at 1.0 then the conclusion is that the dipped film has "holes" where the substrate is uncoated. Such holes have been found by several groups using Atomic Force Microscopy (AFM) [33a - e], including one group who found holes in a cadmium arachidate monolayer on water at 25mN/m [33e]. These holes could have two effects on subsequent dipped monolayers. The first possibility, as proposed by Englisch et al. [29], is that they would be filled in by the next layer, the molecules of which would have to turn over to achieve this, invoking the mechanism proposed by Hönig [19]. The holes would then be perpetuated throughout the structure. Alternatively, the next layer might bridge the holes (the AFM data suggest they are of the order of 300Å across), thus preventing them from having any further effect on the structure beyond reducing the density of the layer in which they are present. A third possibility, and the most likely, is that a combination of both these mechanisms is involved and it might be expected that this would in turn be affected by dipping conditions. The present work, by probing more fully the correspondence between surface pressure (and hence viscosity), dipping speed and film quality, brings new light to bear on the problem of scrambling and shows a means of solving it.

2.5 References.

[1] I. J. Langmuir, J. Am. Chem. Soc., **39**, 1848 (1917).

[2] G. L. Gaines, Insoluble Monolayers at the Air-Water Interface, Wiley (New York) 1966.

[3] A. M. Bibo and I. R. Peterson, Adv. Mater., **2**, 309 (1990).

[4] D. Hönig and D. Möbius, Thin Solid Films, **210/211**, 64 (1992).

[5] R. M. Kenn, C. Böhm, A. M. Bibo, I. R. Peterson, H. Möhwald, J. Als-Nielsen and K. Kjaer, J. Phys. Chem. **95**, 2092 (1991).

[6] M. F. Daniel and J. T. T. Hart, J. Mol. Electron. **1**, 97 (1985).

[7a] B. R. Malcolm, J. Phys. E, **21**, 603 (1988).

[7b] B. R. Malcolm, Thin Solid Films **178**, 17 (1989) and references therein.

[7c] B. R. Malcolm, Thin Solid Films, **178**, 191 (1989).

[8a] M. Buhaenko, J. W. Goodwin, R. M. Richardson and M. F. Daniel, Thin Solid Films, **134**, 217 (1985).

[8b] M. R. Buhaenko, J. W. Goodwin and R. M. Richardson, Thin Solid Films **159**, 171 (1988).

[8c] M. Buhaenko, PhD thesis, University of Bristol, 1988, and references therein.

[9] H. Hasmonay, M. Vincent and M Dupeyrat, Thin Solid Films **68**, 21 (1980).

[10] K. B. Blodgett, J. Am. Chem. Soc. **57**, 1007 (1935).

[11] M. Pomerantz and A. Segmüller, Thin Solid Films, **68**, 33 (1980).

[12] K. Blodgett and I. Langmuir, Phys. Rev. **51**, 964 (1937).

[13] G. L. Clark, R. R. Sterrett and P. W. Leppla, J. Am. Chem. Soc. **57**, 330 (1935).

[14] P. A. Chollet and J. Messier, Thin Solid Films, **99**, 197 (1983).

[15] I. R. Peterson and G. J. Russell, Thin Solid Films, **134**, 143 (1985).

[16] A. I. Kitaigorodsky, "Organic Chemical Crystallography". Consultants Bureau, New York (1961).

[17] E. von Sydow, a) Acta Cryst. **8**, 557 (1955); b) Ark. Kemi. **9**, 231 (1956).

[18] I. Langmuir, Science, **87**, 493 (1938).

[19] E. P. Hönig, J. Coll. Int. Sci. **43**, 66 (1972).

[20] R. C. Ehlert, J. Coll. Sci. **20**, 387 (1965).

[21] E. P. Hönig, Langmuir, **5**, 882 (1989).

[22] J. B. Peng, J. B. Ketterson and P. Dutta, Langmuir, **4**, 1198 (1988).

[23] M. Buhaenko, M. J. Grundy, R. M. Richardson and S. J. Roser, Thin Solid Films, **159**, 253 (1988).

[24] M. J. Grundy, R. J. Musgrove, R. M. Richardson and S. J. Roser, Langmuir, **6**, 519, (1990).

[25] M. Buhaenko and R. M. Richardson, Thin Solid Films **159**, 231 (1988).

[26] R. J. Musgrove, PhD thesis, University of Bristol, 1990.

[27] V. Vogel, Proc. 1st Eur. Conf. on Langmuir-Blodgett Films, Munich, 1986.

[28] U. Pietsch, U. Höhne and H. Möhwald, Langmuir, **9**, 208 (1993).

[29] U. Englisch, T. A. Barberka, U. Pietsch and U. Höhne, Thin Solid Films, **266**, 234 (1995).

[30] P. Tippmann-Krayer, R. M. Kenn and H. Möhwald, Thin Solid Films, **210/211**, 577 (1992).

[31] T. R. Vierheller, M. D. Foster, H. Wu, A Schmidt, W. Knoll, S. Satija and C. F. Majkrzak, Langmuir, **12**, 5156 (1996).

[32] U. Englisch, T. Gutberlet, R. Steitz, R. Oeser and U. Pietsch, Phys. Stat. Sol. B, **201**, 67 (1997).

[33a] E. Meyer, L. Howald, R. M. Overney, H. Heinzelmann, J. Frommer, H. J. Güntherodt, T. Wagner, H. Schier and S. Roth, Nature, **349**, 398 (1991).

[33b] L. Bordieu, P. Silberzan and D. Chatenay, Phys. Rev. Lett. **67**, 2029 (1991).

[33c] H. G. Hansma, S. A. C. Gould, P. K. Hansma, H. E. Gaub, M. L. Longo and J. A. N. Zasadzinski, Langmuir, **7**, 1051 (1991).

[33d] D. K. Schwartz, J. Garnaes, R. Viswanathan and J. A. N. Zasadzinski, Science, **257**, 508 (1992).

[33e] O. Mori and T. Imae, Langmuir, **11**, 4779 (1995).

Chapter 3. The Theory of X-Ray and Neutron Reflectivity.

3.1 Introduction.

As mentioned in Chapter 2, X-ray and neutron reflectivity techniques are extremely useful for the study of a variety of organic systems, especially lamellar systems such as Langmuir or LB films. This is primarily because the supporting substrate, whether it is water or a silicon wafer, can be allowed for very readily, so that special preparation techniques are not required, and also because deuterium has a very different effect on an incident beam of neutrons than does hydrogen, so that deuterium can be used to highlight particular aspects of the internal structure. Selective deuteration of the organic component is relatively straightforward in terms of chemical synthesis, making neutron reflectivity an easily accessible and widely used technique for the study of organic systems. X-ray reflectivity complements the neutron technique by providing information about the bulk sample, such as overall thickness, which makes subsequent analysis of the neutron data much simpler. This is because analysis of the neutron data is not trivial, and as much information as possible about the likely structure of the film must be included from the start in any model used.

In order to understand specular neutron and X-ray reflectivity, it is necessary to develop the basic theory behind these two experimental techniques, and this is the purpose of the first part of this chapter. The discussion then covers the currently available approaches to the modelling process required for data analysis, and their respective advantages and limitations. The complementarity of the two techniques is illustrated throughout.

3.2 Interaction of X-rays and Neutrons with Matter.

3.2.1 X-rays.

When a beam of electrons is fired at a metallic target under an applied voltage, they excite electrons in the outer shells up to higher energy levels. When these decay back to

their original level, the excess energy is released as photons of particular wavelengths, characteristic of the target metal. For copper, the brightest of these is at 1.54 Å (Kα), representing the drop from the 2p level (L shell) to the 1s level (K shell), and this is commonly used for investigating structure on the atomic and molecular scale. The Kβ peak represents the drop from 2s to 1s. In addition, the incident electrons are subject to deceleration by the nuclei of the metal. The excess energy is given off as photons with a wide range of wavelengths, thus giving rise to a broad spectrum of X-rays known as Bremsstrahlung ("braking radiation"). The short-wavelength (i.e. maximum energy) limit of the Bremsstrahlung radiation is determined by the accelerating voltage, as given in Eq. 3.1. Figure 1 shows the X-ray spectrum for copper.

$$\lambda = \frac{hc}{Ve} \tag{3.1}$$

where

λ = wavelength, m.

h = Planck's constant, 6.63×10^{-34} Js.

c = velocity of light, 3.00×10^{8} m/s.

V = applied voltage, eV.

e = charge on an electron, 1.60×10^{-19} C.

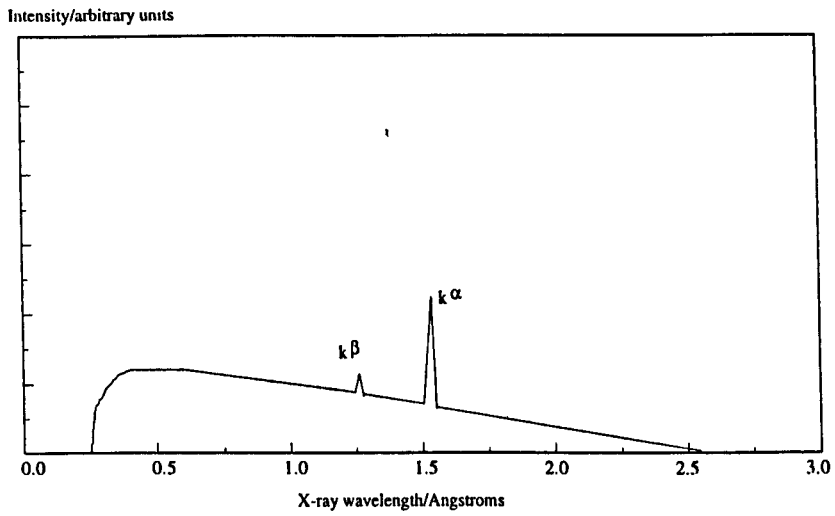

Figure 1 X-ray spectrum for copper at 50keV, showing the Bremsstrahlung radiation and the characteristic peaks. The cut-off at 0.25Å illustrates Eq 3.1.

Just as X-rays are produced by the interaction of electrons with matter, they themselves interact with the electrons of any atom they encounter. The incoming X-ray is an oscillating electric field and so it causes the electron to oscillate. This oscillating charge in turn emits some radiation of the same wavelength (i.e. elastic scattering), but not necessarily in the same direction as the incident beam. Thus the X-rays are scattered out of their incident path and the degree of scattering depends only on the number of electrons in the atom, i.e. its atomic number. The amplitude of the wave scattered by a single electron is given below:

$$A = \frac{A_0 P^{1/2} a_e}{R} \qquad (3.2)$$

where

A = scattered amplitude.

A_0 = incident amplitude.

P = polarisation factor. For an unpolarised incident beam,

$P = \frac{1}{2} + \frac{1}{2}\cos 2\theta$, where 2θ = scattering angle.

R = distance from the electron.

a_e = scattering length of an electron. $a_e = \frac{\mu e^2}{4\pi m} = 2.8 \times 10^{-5}$Å, where

μ = magnetic permeability of a vacuum, 1.26×10^{-6} H/m,

e = charge on an electron, 1.60×10^{-19} C,

m = rest mass of an electron, 9.10×10^{-31}kg.

(This is the basis for ignoring the effect of the nucleus on the X-rays, since its mass m is very large compared with the mass of an electron.)

The intensity of the scattered X-ray is given by

$$I = |A|^2 = \frac{I_0 P a_e^{\,2}}{R^2} \qquad (3.3)$$

where I_0 is the incident intensity.

Considering the case of X-rays scattered from the whole atom, only the effect of the electrons is taken into account as mentioned above, and the overall effect is obtained by simply adding up the amplitude from the different electrons within the atom, taking account of the interference between waves from different parts of the electron cloud:

$$A_{atom} = \frac{A_0 P^{1/2} a_e}{R} f(Q) \qquad (3.4)$$

The term $\frac{A_0 P^{1/2}}{R}$ is known as $A_{standard}$.

Q is the scattering vector, i.e. the change in wave-vector on scattering.

$$Q = \frac{4\pi \sin\theta}{\lambda} \qquad (3.5)$$

f(Q) is the atomic form factor, which depends on the distribution of the electrons. At low Q, f(Q) = atomic number, Z.

Hence at low Q, the X-ray scattering length of an atom = Za_e.

3.2.2 Neutrons.

There are two mechanisms whereby neutrons are scattered. In the first, the magnetic moment of the neutron causes it to be scattered by unpaired electrons in the atom. This is a very useful phenomenon for the investigation of the magnetic properties of materials, but it is not used for this work, although two samples were prepared on Ni (i.e. ferromagnetic) substrates as a courtesy to RAL scientists investigating this phenomenon.

In the second mechanism, neutrons are scattered by nuclear forces, which are very strong and very short range. The neutrons may be scattered coherently, i.e. in a known and constant direction, giving a high intensity in that direction, or incoherently, i.e. in random directions, giving a very low intensity in any one direction.

For neutrons, the scattered amplitude is similar to that in the case of X-rays, namely:

$$A = \frac{A_0 b}{R} \tag{3.6}$$

where

A = scattered amplitude.

A_0 = incident amplitude.

b = nuclear scattering length, i.e. the effective diameter of the nucleus.

R = distance from the atom.

$A_{standard}$ in the case of neutrons is given by:

$$A_{standard} = \frac{A_0}{R} \tag{3.7}$$

Again, similar to X-rays, the scattered intensity is given by:

$$I = \frac{I_0 b^2}{R^2} \qquad (3.8)$$

Note that there is no polarisation factor in the case of neutrons since the wave (neutron) has no polarisation, and note also that b is independent of Q.

The scattering length b is a nuclear quantity and is independent of atomic number Ż. It arises both from different spin states of the nucleus within a pure element, and also from the distribution of isotopes within a naturally-occurring element. Values of b for elements relevant to this work are given in Table 1 and it can be seen that they vary irregularly. The value for hydrogen is negative because the neutron undergoes a phase change of 180° on interacting with the nucleus.

Element	Atomic number, Z	b /10^{-5} Å.
H	1	-3.73
D	1	6.67
C	6	6.65
O	8	5.80
Si	14	4.15
N	7	9.36

Table 1 Neutron scattering lengths of some elements.

Note the large difference in b values between H and D in Table 1. It is this property of neutron scattering that renders it such a useful technique for the study of organic materials, making it possible for large levels of contrast to be built into a particular molecule, or even parts of a molecule, within the system under study.

For most of the elements relevant to this work, the contribution to b from incoherent scattering is negligible. The exception is hydrogen, where it is the coherent contribution to b that is by far the smaller.

3.2.3 Scattering Length Density.

Scattering lengths only apply to individual atoms. To apply the theory to bulk systems we must use scattering length densities, ρ, which take into account the number density of each scattering atom. Thus for a pure element:

$$\rho = Nb \qquad \text{for neutrons} \qquad (3.9)$$

$$\rho = NZa_e \qquad \text{for X-rays.} \qquad (3.10)$$

N is the number of atoms per unit volume, i.e. the number density, and it is typically given as the number per $Å^3$.

For a compound with several types of atom,

$$\rho = \sum_i N_i b_i \qquad \text{for neutrons} \qquad (3.11)$$

$$\rho = a_e \sum_i N_i Z_i \qquad \text{for X-rays} \qquad (3.12)$$

where

N_i is the number density of atom type i,

b_i is the neutron scattering length of atom type i

Z_i is the atomic number of atom type i.

Examples of scattering length densities of some relevant compounds for both neutrons and X-rays are given in Table 2.

Compound	ρ (neutrons) /10^{-5} Å^{-2}	ρ (X-rays) /10^{-5} Å^{-2}
H_2O	-0.05	0.94
D_2O	0.64	0.94
$-CH_2-$	-0.06	0.65
$-CD_2-$	0.61	0.65

Table 2 Scattering length densities (SLDs) of some relevant materials, showing the neutron contrast of deuterated compounds.

3.2.4 Scattering from a Bulk Material.

Each portion of the whole makes its own contribution to the total scattered amplitude. These contributions may be calculated for each portion, summed over the whole and converted to intensity, for direct comparison with the intensity that is measured by the apparatus.

The scattering length of each portion = $\rho(\mathbf{r})\ d\mathbf{r}$, where $\rho(\mathbf{r})$ is the scattering length density of the portion and $\mathbf{r}$ is the vector representing the position of that portion within the whole.

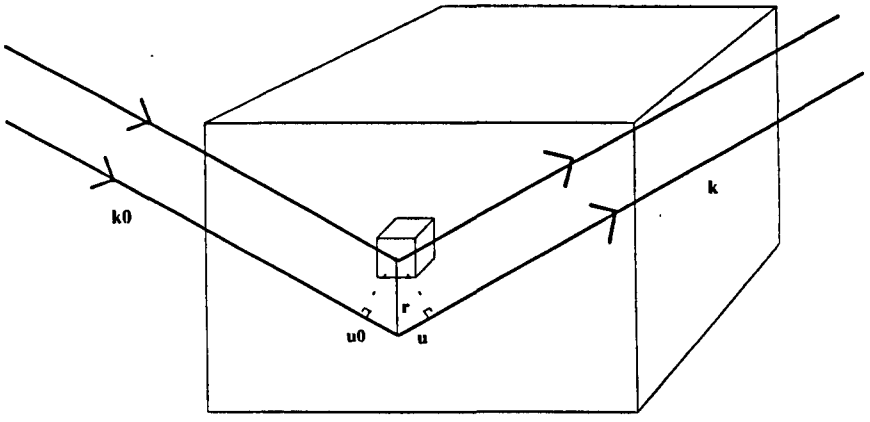

Figure 2 Illustration of the vectors that must be considered to calculate scattering amplitudes.

The amplitude of the scattered wave from each portion is therefore

$$dA = \rho(\mathbf{r})\, d\mathbf{r} \tag{3.13}$$

In summing these contributions, we must consider phase and path differences. These are illustrated in Figure 2, where the incoming wave has the vector

$$\mathbf{k}_0 = \frac{2\pi}{\lambda}\mathbf{u}_0 \tag{3.14}$$

and the scattered wave has the vector

$$\mathbf{k} = \frac{2\pi}{\lambda}\mathbf{u} \tag{3.15}$$

Path difference = $\mathbf{r}.\mathbf{u} - \mathbf{r}.\mathbf{u}_0 = \mathbf{r}\,(\mathbf{u} - \mathbf{u}_0)$

Phase difference = $\frac{2\pi}{\lambda} . \mathbf{r}\,(\mathbf{u}-\mathbf{u}_0) = \mathbf{r}\,(\mathbf{k} - \mathbf{k}_0) = \mathbf{r}.\mathbf{Q}$, since $\mathbf{Q} = \mathbf{k} - \mathbf{k}_0$ and where $|\mathbf{Q}|$ is as given in Equation 3.5.

Therefore

$$dA = \rho(\mathbf{r}) d\mathbf{r}\, e^{i\mathbf{Q}\,\mathbf{r}} \tag{3.16}$$

where $e^{i\mathbf{Q}\cdot\mathbf{r}}$ is the phase term, representing a phase shift of $\mathbf{Q}\cdot\mathbf{r}$ radians. Hence a variation in $\mathbf{r}$ yields a sinusoidal amplitude.

The scattered amplitude is given by

$$A(\mathbf{Q}) = \int_v dA = \int_v \rho(\mathbf{r})\, e^{i\mathbf{Q}\cdot\mathbf{r}}\, d\mathbf{r} \tag{3.17}$$

where v is the sample volume.

To convert amplitude to intensity, use $I = |A|^2$ and express $I(\mathbf{Q})$ relative to a unit scattering length at the origin:

$$I(\mathbf{Q}) = |\int_v \rho(\mathbf{r})\, e^{i\mathbf{Q}\cdot\mathbf{r}}\, d\mathbf{r}\,|^2 \tag{3.18}$$

In practice, the volume is infinite compared to the portion of interest. With $\int_\infty$ we have the Fourier Transform.

3.3 Reflectivity.

3.3.1 Basic Concepts.

The technique of reflectivity involves radiation which is incident to the sample at a grazing angle. This is illustrated in Figure 3, along with some of the main variables used.

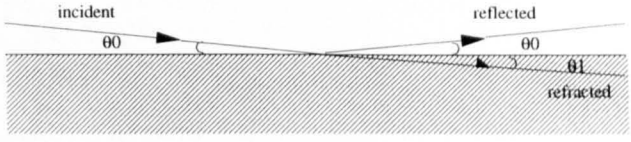

Figure 3 Showing the principle of reflectivity. θ_0 is the (glancing) angle of incidence and reflection, θ_1 is the angle of the refracted beam.

I is measured as a function of angle, θ, or wavelength, λ. The momentum transfer, Q, is related to the measured θ or λ according to Eq. 3.5:

$$Q = \frac{4\pi \sin\theta}{\lambda} \tag{3.5}$$

From the measured I we determine

$$R(Q) = \frac{I_{reflected}}{I_{incident}} \tag{3.19}$$

Hence reflectivity is always less than or equal to 1.

We can use classical optical formulae to understand X-ray and neutron behaviour at interfaces. In particular, the refractive index, n, is given by

$$n = 1 - \frac{\lambda^2 \rho}{2\pi} \tag{3.20}$$

where

λ is the incident wavelength and

ρ is the scattering length density of the material.

It is also conventional to use angles measured with respect to the surface, rather than with respect to the normal to the surface.

From classical optics, Fresnel's Law for a single interface gives

$$R = \left| \frac{n_0 \sin\theta_0 - n_1 \sin\theta_1}{n_0 \sin\theta_0 + n_1 \sin\theta_1} \right|^2 \qquad (3.21)$$

where n_0, n_1, θ_0 and θ_1 are as given in Figure 4.

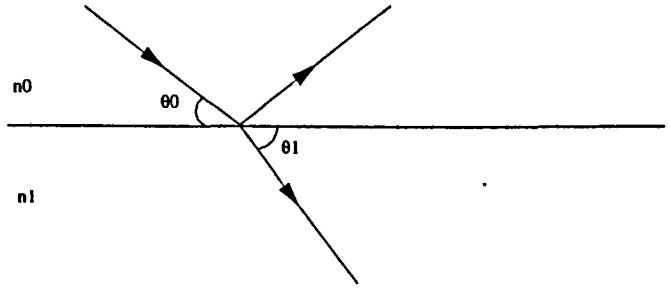

Figure 4 Diagram illustrating Fresnel's Law. n_0 and n_1 are the refractive indices of the two media, θ_0 is the angle of incidence (and reflection) and θ_1 is the angle of refraction.

An incident angle θ_c exists such that, when $\theta_0 < \theta_c$, $n_1 \sin\theta_1$ is imaginary. This is the evanescent wave and it decays exponentially into the bulk. $R \sim 1$.

Similarly, when $\theta_0 = \theta_c$, $n_1 \sin\theta_1 = 0$ and $R=1$.

Finally, when $\theta_0 > \theta_c$, $n_1 \sin\theta_1$ is real and reflectivity is observed, $R < 1$.

Thus, that part of the scattering which is due to the layer structure of the sample is only observed above Q_c. This is defined as

$$Q_c = 2k\sin\theta_c \qquad (3.22)$$

where

$$k = \frac{2\pi}{\lambda}$$

$$\theta_c = \lambda\sqrt{\frac{\rho}{\pi}}$$

and hence

$$Q_c = 4\sqrt{(\pi\rho)}$$

(since θ_c in radians $\equiv \sin\theta_c$ for low θ_c , i.e. grazing angles.)

The point at which R becomes less than 1 is termed the critical edge and its position in Q, λ or θ may be used to calculate the SLD of the substrate, or of the film if it is thick enough to produce a discernible edge of its own. It can thus be seen that allowing for the supporting substrate is a straightforward part of the data analysis, and this is one of the main reasons why these techniques are so useful for studying organic systems.

There are different approaches to generating a model to fit the data: the kinematic approximation is the easiest to visualise, while the optical matrix method is the most accurate.

3.3.2 The Kinematic Approximation.

This approach calculates approximate reflectivity profiles using Fourier transforms to represent changes in SLD through the sample.

$$I(Q) = |\int \rho(\mathbf{r})\, e^{i\,Q.r}\, d\mathbf{r}\,|^2 \qquad (3.23)$$

where $\rho(\mathbf{r})$ is independent of x and y, i.e. it only varies perpendicular to the substrate, in the z direction.

The Fourier transform (FT) of a constant is a δ-function, and in this case it is given by $2\pi\ \delta\ (Q_\perp)$. A sharp peak is seen at $Q_\perp = 0$, i.e. reflection is only seen if Q is exactly perpendicular to the surface. Hence

$$I(Q) = (2\pi)^2 \left| \int \rho(z)\, e^{iQ_z \cdot z}\, dz \right|^2 \delta\ (Q_\perp) \qquad (3.24)$$

The delta function, $\delta\ (Q_\perp)$, defines the specular peak in the scattered beam. To calculate the reflectivity we must convert this to a function of scattered beam direction and then integrate over the peak. These steps introduce a factor of $(2\pi)^2$ (from integration over a 2D δ-function) and a factor of $\frac{4}{Q_z^2}$ (the Jacobian arising from integration over dθ, dϕ, i.e. the conversion factor when changing from rectangular to polar coordinates).

$$R(Q_z) \approx (2\pi)^2 \frac{4}{Q_z^2} \left| \int \rho(z)\, e^{iQ_z \cdot z}\, dz \right|^2 \qquad (3.25)$$

Simplifying:

$$R(Q_z) \approx \frac{16\pi^2}{Q_z^2} \left| \int \rho(z)\, e^{iQ_z \cdot z}\, dz \right|^2 \qquad (3.26)$$

The kinematic approximation is not valid in the low Q region around Q_c , where total external reflection is approached. However, it has the advantage that it provides a simple formula to relate surface structure to reflectivity, and interface roughness can be built in to the model very readily. It is extremely useful for the ease with which the contribution to the reflectivity profile from given parts of the structure can be visualised. This is now illustrated with a worked example.

The reflectivity profile from a film is modulated by a cosine wave. Consider neutron reflection from a monolayer of surfactant on air-contrast-matched (acm) water, i.e. a mixture of H_2O and D_2O such that the resultant neutron SLD is zero (92% H_2O and 8% D_2O). This is illustrated in Figure 5.

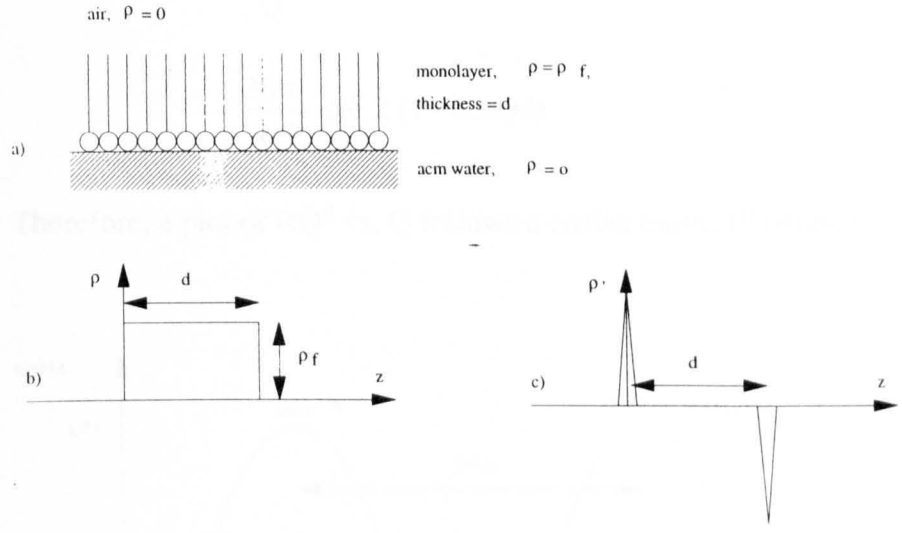

Figure 5 a) Showing a surfactant monolayer on acm water, b) SLD profile of the system, c) differential of the SLD profile.

To obtain R in this instance, we need to calculate the integrals of the two δ-functions in Fig. 5c), multiplied by e^{iQz}. This is done using integration by parts:

$$R(Q_z) \approx \frac{16\pi^2}{Q^4} \left| \int \frac{\partial \rho}{\partial z} e^{iQz} \, dz \right|^2 \tag{3.27}$$

Since the integral of the δ-function at the origin in Fig. 5c) is 1 and that of the δ-function at z = d is e^{iQd},

$$R = \frac{16\pi^2}{Q^4} \cdot | \rho_f + (-\rho_f) e^{iQd} |^2 \tag{3.28}$$

$$= \frac{16\pi^2}{Q^4} \cdot \rho_f^2 \, | \, 1-(\cos Qd + i \cdot \sin Qd) |^2$$

$$= \frac{16\pi^2}{Q^4} \cdot \rho_f^2 \, | \, 1- \cos Qd - i \cdot \sin Qd \, |^2$$

$$= \frac{16\pi^2}{Q^4} \cdot \rho_f^2 \, (1- \cos Qd)^2 + (\sin Qd)^2$$

$$= \frac{16\pi^2}{Q^4} \cdot \rho_f^2 \, (1 - 2\cos Qd + \cos^2 Qd + \sin^2 Qd)$$

$$= \frac{16\pi^2}{Q^4} \cdot \rho_f^2 \, 2 \, (1 - \cos Qd) \qquad (3.29)$$

Therefore, a plot of RQ^4 vs. Q follows a cosine curve, illustrated in Figure 6.

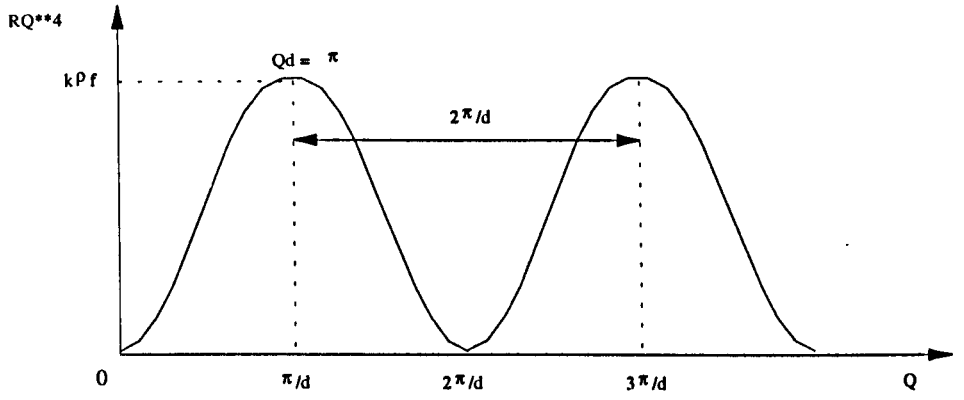

Figure 6 Plot of RQ^4 vs. Q for reflectivity data from a monolayer. Note that at the first maximum $Q = \pi/d$ and at the first minimum $Q = 2\pi/d$. It is also possible to obtain ρ_f from the position of the first maximum against the y-axis: $k\rho_f = 64\pi^2\rho_f^2$.

At $Q > Q_c$, the reflectivity is subject to Fresnel decay. This occurs with all samples. For a single interface, the kinematic approximation can be used to show that this causes R to decay at the rate of Q^4 [1] according to:

$$R(Q) = \frac{16\pi^2}{Q^4} \Delta\rho^2 \qquad (3.30)$$

3.3.3 The Optical Matrix Method.

This method uses classical optics, and a matrix to describe each layer within the film in terms of thickness and SLD. It is therefore an exact method, but one which cannot generally be expressed as a simple formula.

The refractive index of a material for neutrons and X-rays was given in Eq. 3.20, Section 3.3.1:

$$n = 1 - \frac{\lambda^2 \rho}{2\pi} \tag{3.20}$$

In all other respects the beams may be treated as visible light.

Referring back to Figure 4 for definitions, for a single uniform layer:

$$R = \left| \frac{r_{01} + r_{12} e^{-2i\beta}}{1 + r_{01} r_{12} e^{-2i\beta}} \right|^2 \tag{3.31}$$

where

$r_{ij} = \frac{P_i - P_j}{P_i + P_j}$, the reflection coefficient at each boundary

$P_i = n_i \sin\theta_i$

$\beta = \frac{2\pi n_1 d \sin\theta_1}{\lambda}$.

β is the phase difference across the layer.

This expression for R may be restated as

$$R = \frac{r_{01}^2 + r_{12}^2 + 2 r_{01} r_{12} \cos^2\beta}{1 + r_{01}^2 r_{12}^2 + 2 r_{01} r_{12} \cos^2\beta} \tag{3.32}$$

For a multilayer film, a matrix M_j is defined for the jth layer as follows:

$$M_j = \begin{pmatrix} \cos\beta_j & -(i/P_j)\sin\beta_j \\ -iP_j\sin\beta_j & \cos\beta_j \end{pmatrix} \tag{3.33}$$

and the resultant reflectivity for 2 layers is given by:

$$R = \left| \frac{(M_{11} + M_{12}P_s)P_a - (M_{21} + M_{22}P_s)}{(M_{11} + M_{12}P_s)P_a + (M_{21} + M_{22}P_s)} \right|^2 \tag{3.34}$$

where the subscripts s and a refer to substrate and air respectively. The reflectivity for a multilayer is obtained by multiplying the matrices for each layer in the same way.

To include roughness at the interfaces, r_{ij} is replaced by the following expression [1]:

$$r_{ij} = \frac{P_i - P_j}{P_i + P_j} \exp\left[-0.5(Q_iQ_j \langle\sigma^2\rangle)\right] \tag{3.35}$$

The optical matrix method was used for all the modelling in the present work. Some simulations using the optical matrix method are now presented, for illustrative purposes.

In addition to the common features discussed above, the factors which affect the shape of the reflectivity profile from a particular individual sample are substrate and sample roughnesses and SLDs, overall thickness, and internal structure, such as repeat distances within a multilayer sample.

Roughness affects the reflected intensity by scattering the incident beam more widely than would a smooth surface, causing the measured intensity to fall off more rapidly in Q.

$$I = I_0 \exp(-Q^2\sigma^2) \tag{3.36}$$

where

I_0 = incident intensity

I = reflected intensity

$Q = 2k\sin\theta$

$$k = \frac{2\pi}{\lambda}$$

σ = rms Gaussian roughness.

SLD values also affect the intensity of the reflected beam, and the effects of coherent and incoherent scattering have already been mentioned in Section 3.2.2. For instance, a deuterium-labelled sample will give a higher reflected intensity in a neutron beam than will a straightforward hydrocarbon sample. The presence of a heavy metal such as Cd will introduce similar contrast in X-ray reflectivity, while it will absorb strongly in a neutron beam. The difference in SLD values between the various components of the sample is also important - if two adjacent parts of the sample have very similar SLDs, they will be difficult to distinguish. This is why neutron reflectivity is so useful for studying scrambling in H and D LB films - if the layers have mixed, their SLDs will be averaged out, and the reflected intensity will be very much less than for unmixed layers.

The SLD of the substrate also affects the profile over the very low Q range where total external reflection takes place, i.e. where R = 1.

The overall thickness of the sample and internal layer order affect the reflected intensity via interference effects. Chief among these is the Bragg relation,

$$n\lambda = 2d \sin\theta \qquad (3.37)$$

where

n = order of Bragg peak

λ = incident wavelength

d = layer thickness

θ = angle of incidence

Given that

$$Q = \frac{4\pi \sin\theta}{\lambda} \qquad (3.5)$$

it is straightforward to show that at a Bragg peak,

$$Q = \frac{2n\pi}{d} \tag{3.38}$$

Similarly, interference from the entire sample thickness also gives rise to fringes, known as Kiessig fringes. Since Q is inversely proportional to d, these fringes are narrow for thick (~1000 Å) films and broad for thin (~50 Å) films.

These two separate sets of fringes are superimposed on each other in the measured reflectivity profile and this must be taken into account when analysing the data.

The influence of each of these factors on the shape of an example reflectivity profile is shown in Figure 7a) - 7d). These are simulations, using values of SLD for film and substrate which are applicable to neutrons.

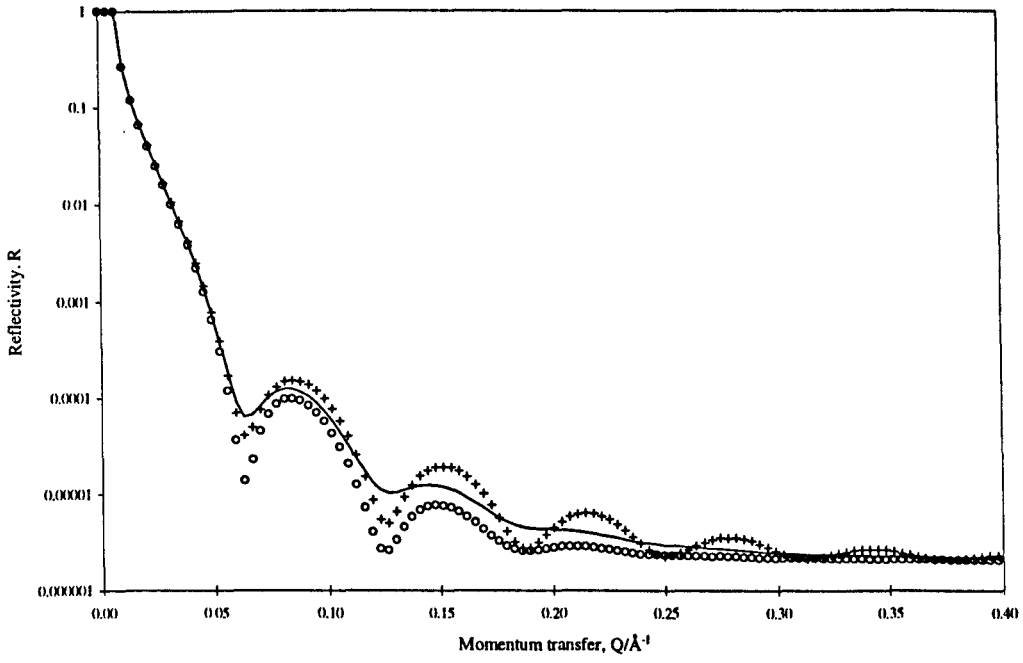

Figure 7a) Showing the effect of roughness on the reflectivity profile. ++++ substrate and film both with zero roughness; —— substrate roughness 10 Å, film roughness zero; oooo substrate roughness zero, film roughness 10 Å. The substrate SLD is 2.01×10^{-6}Å^{-2}, the layer SLD is 5.0×10^{-6}Å^{-2} and the layer thickness is 100Å. The background neutron intensity for the simulation is 2×10^{-6}.

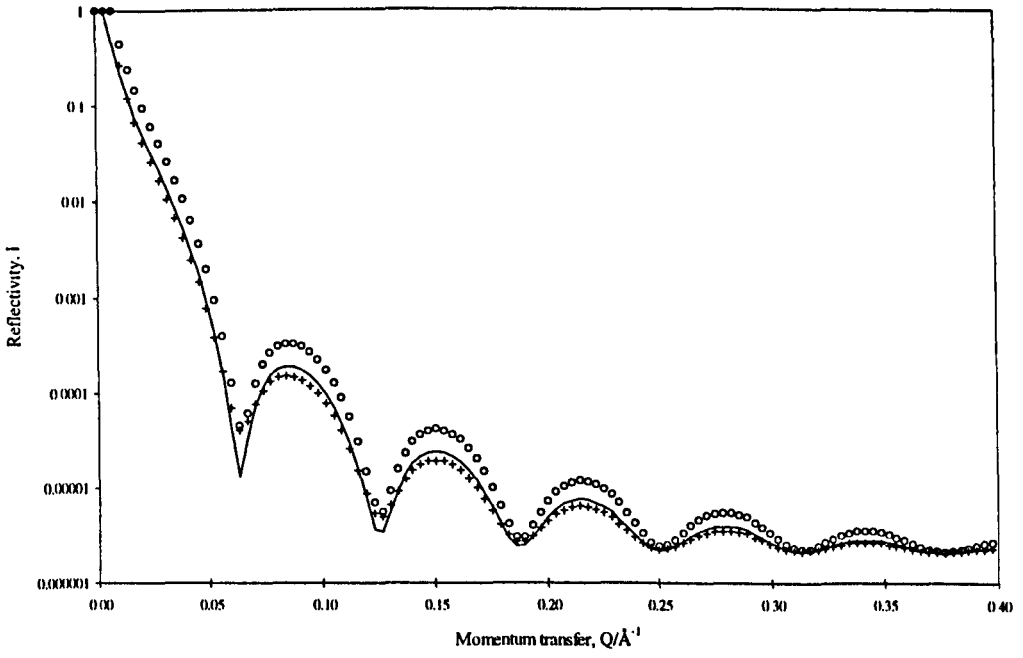

Figure 7b) Showing the effect of sld variation. ++++ substrate sld 2.01 x 10^{-6} $Å^{-2}$, film sld 5 x 10^{-6} $Å^{-2}$; —— substrate sld 1 x 10^{-6} $Å^{-2}$, film sld 5 x 10^{-6} $Å^{-2}$; oooo substrate sld 2.01 x 10^{-6} $Å^{-2}$, film sld 7 x 10^{-6} $Å^{-2}$. Film thickness 100Å, all roughnesses zero. Background 2×10^{-6}.

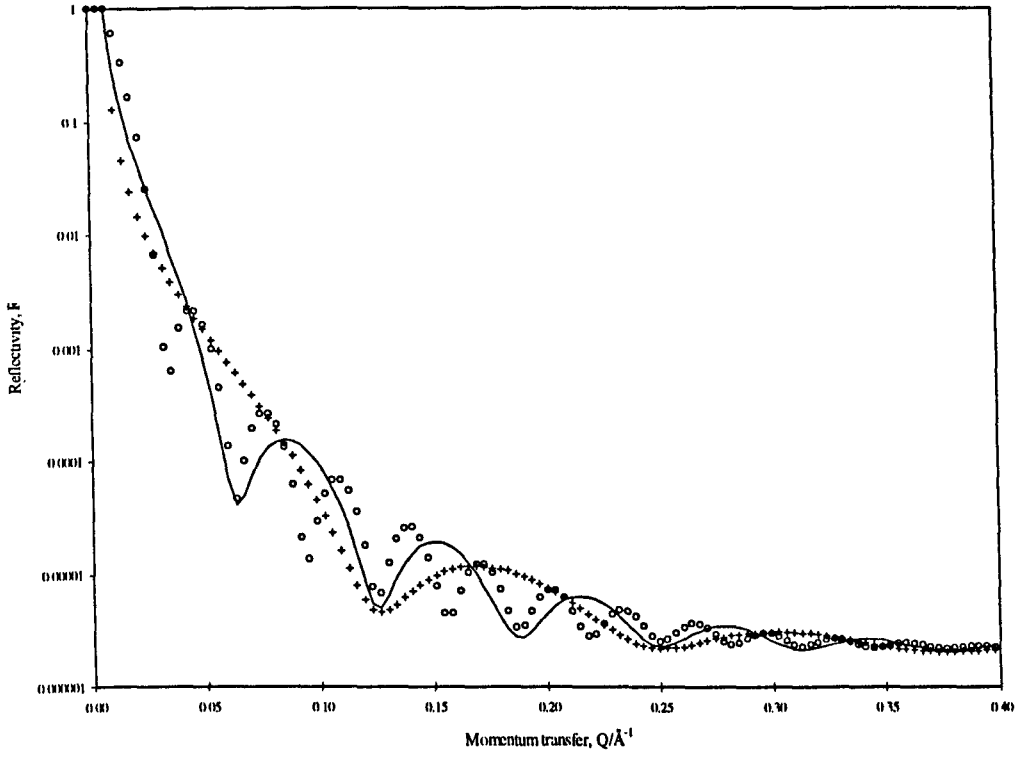

Figure 7c) Showing the effect of total film thickness. ++++ film 50 Å thick; —— film 100 Å thick; oooo film 200 Å thick. Roughnesses zero; film and substrate SLDs and background as in Figures 7a) and 7b).

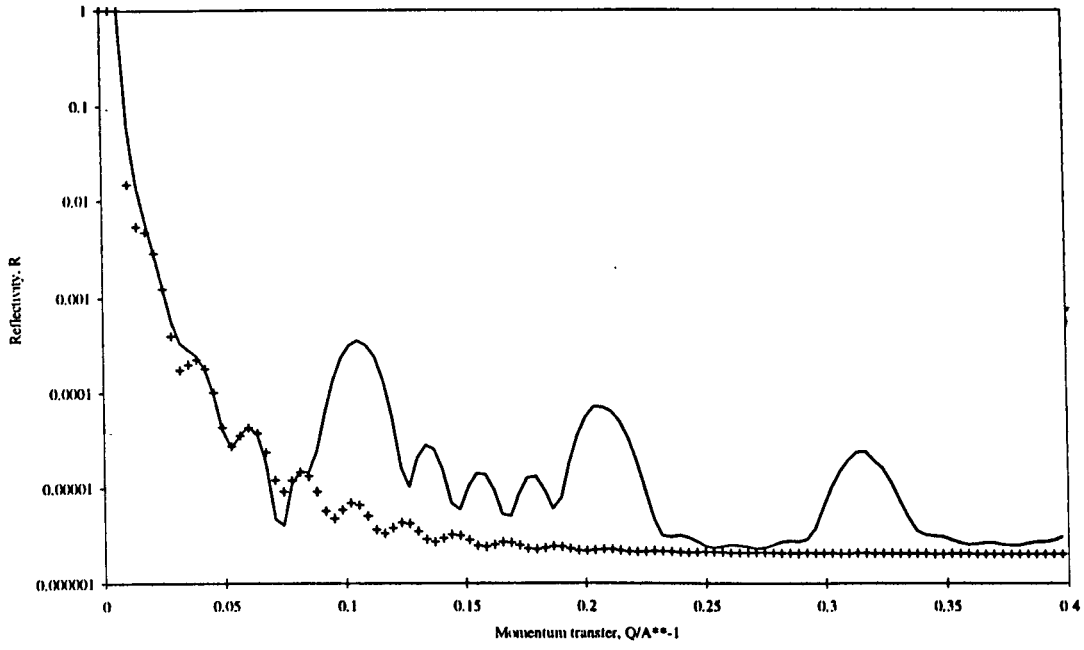

Figure 7d) Showing how internal repeats produce Bragg peaks. ++++ single film 297.5 Å thick, sld = 1.57 x 10^{-6} $Å^{-2}$; —— 11-layer film, similar to a fatty acid LB film, with a 26 Å tail region, sld = 1 x 10^{-6} $Å^{-2}$, and a 7.5 Å double headgroup region, sld = 5.5 x 10^{-6} $Å^{-2}$. Roughnesses zero; substrate SLD and background as in Figures 7a) - 7c). The dipping process results in only the first and final tail regions being 26 Å thick: the remainder are bilayers, and therefore 52 Å thick. The three large (first, second and third order) Bragg peaks arise from this 52 Å repeat distance. The Kiessig fringes are particularly clear between the first and second order Bragg peaks.

3.4 Summary of Approaches to Interpreting the Data.

As has been seen, direct inversion of the data to yield a sample structure is not generally possible, because of the large number of possible solutions to each reflectivity profile, even given restrictions based on *a priori* knowledge of the system being studied. A theoretical profile is therefore generated, as in the above examples, from estimates of parameters such as layer thickness, roughness and scattering length density (SLD), compared with the data and refined by adjusting the input parameters until a fit with the data is obtained. However, even a good fit cannot be assumed to represent a unique solution, since it might only be a local minimum. Solution space must be explored thoroughly to look for other minima before any confidence can be placed in a particular structure.

There are currently four main methods used to generate the theoretical profiles needed for this fitting process. These are the kinematic approximation [2] and the optical matrix method [3], both of which have already been discussed in detail, the maximum entropy method, MaxEnt [4] and the cubic splines method [5]. The third method, MaxEnt, starts from a fixed sample thickness and substrate SLD which have been chosen by the user, assumes the sample is a one-layer slab and explores roughnesses and film SLD on this basis. If no fit is found it then assumes the sample is made up of two distinct layers consistent with the fixed total thickness and again explores roughnesses and film SLDs. It can continue up to a maximum of 20 layers. Even disregarding the very long computing times required for this process, 20 layers proved insufficient to fit the data in this work, so after a brief trial MaxEnt was not used in the present work. Similarly for the method of cubic splines - it generated an excellent fit, but with an SLD profile involving physically unreasonable SLD values given the known nature of the samples, so it too was not used and will not be discussed further. The kinematic approximation and the optical matrix method therefore formed the backbone of the modelling approach used to analyse the data from the present work. Further details may be found in [2] and [3], and the evolution of the particular method used here is described in Chapter 5.

3.5 References

[1] L. Névot and P. Crocé, Phys. Appl. **15**, 761 (1980) and R. A. Cowley and T. W. Ryan, J. Phys. D: Appl. Phys. **20**, 61 (1987).

[2] J. Penfold and R. K. Thomas, J. Phys.: Condensed Matter, **2**, 1369 (1990).

[3] M. Born and E. Wolf, Principles of Optics, Pergamon, Oxford (1970) and O. S. Heavens, Optical Properties of Thin Films, Butterworth ,London (1955).

[4] D. S. Sivia, W. A. Hamilton and G. S. Smith, Physica B, **173**, 121 (1991).

[5] J. S. Pedersen, J. Appl. Cryst. **25**, 129 (1992).

Chapter 4. Experimental

4.1 Introduction

This chapter gives details of all the apparatus and techniques used in the present work. It starts by describing the necessary preparation of the equipment prior to experimentation, then discusses the procedures required for the formation and manipulation of Langmuir films and the dipping of Langmuir-Blodgett films, and finally details the techniques which have been used in this work to characterise the LB films which have been prepared.

4.2 Preparation and Cleaning

Since Langmuir films consist of a one-molecule-thick layer of an amphiphile floating on water, it will be clear that contamination is to be avoided and that cleanliness is paramount. To this end, the amphiphiles used were obtained at the highest available purity (99+%, Fluka or Larodan). Water was first distilled, and then filtered by an Elgastat Spectrum B water purification system (Elga) to provide water with a resistivity in the range 16-18 MΩm and a surface tension between 70-71.9 mN/m. The pure water thus obtained has a pH of 5.5 due to dissolution of atmospheric carbon dioxide and it is a potent cleaning solvent in its own right. The chloroform used was Aristar grade, ex Merck, and all other solvents were HPLC grade ex Aldrich. The Langmuir troughs themselves were housed in cabinets to minimise airborne contamination, although obviously working in a clean room is the ideal, if facilities are available. Troughs were cleaned immediately before embarking on a series of experiments and on a weekly basis for the duration of that series. Glassware and other implements were cleaned at the end of a series of experiments and stored in a clean, segregated cupboard. If necessary, they were cleaned again immediately before use. All the procedures for these cleaning arrangements will be given in detail in subsequent sections. Schematic diagrams of the Langmuir trough used for the bulk of this work are shown in Figure 1. A diagram of the two-compartment trough used for alternating films will be given later, in the section on dipping (Section 4.5).

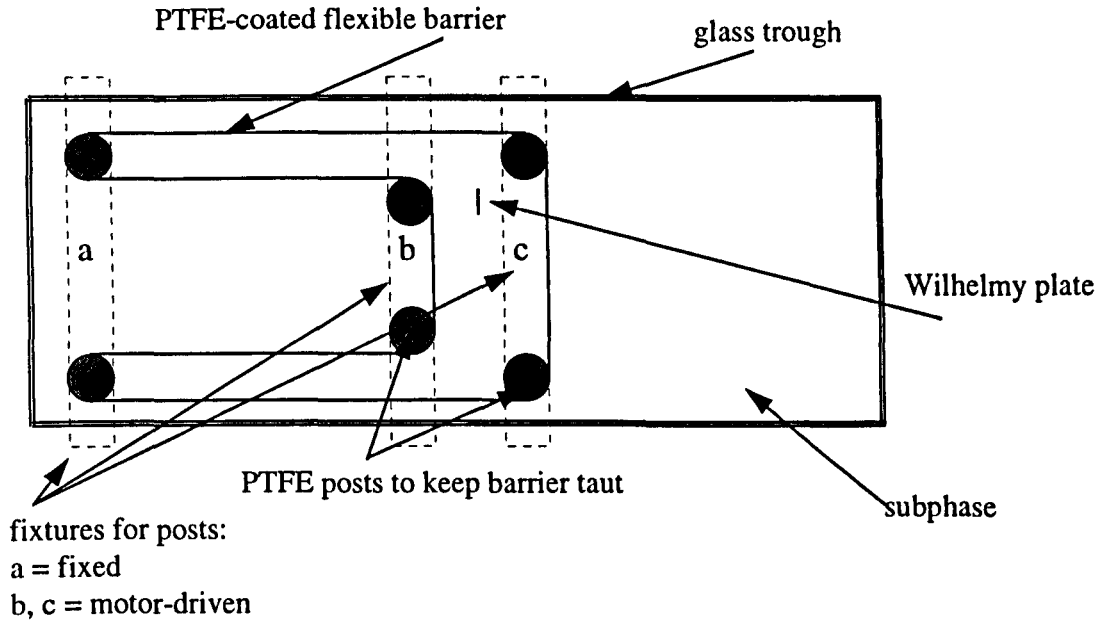

Figure 1 a) Schematic plan view of a Langmuir trough with the barriers closed.

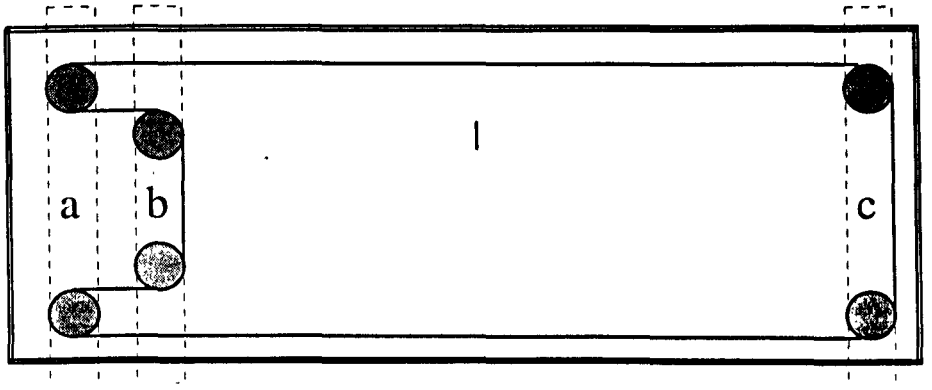

Figure 1 b) Schematic plan view of a Langmuir trough with the barriers open.

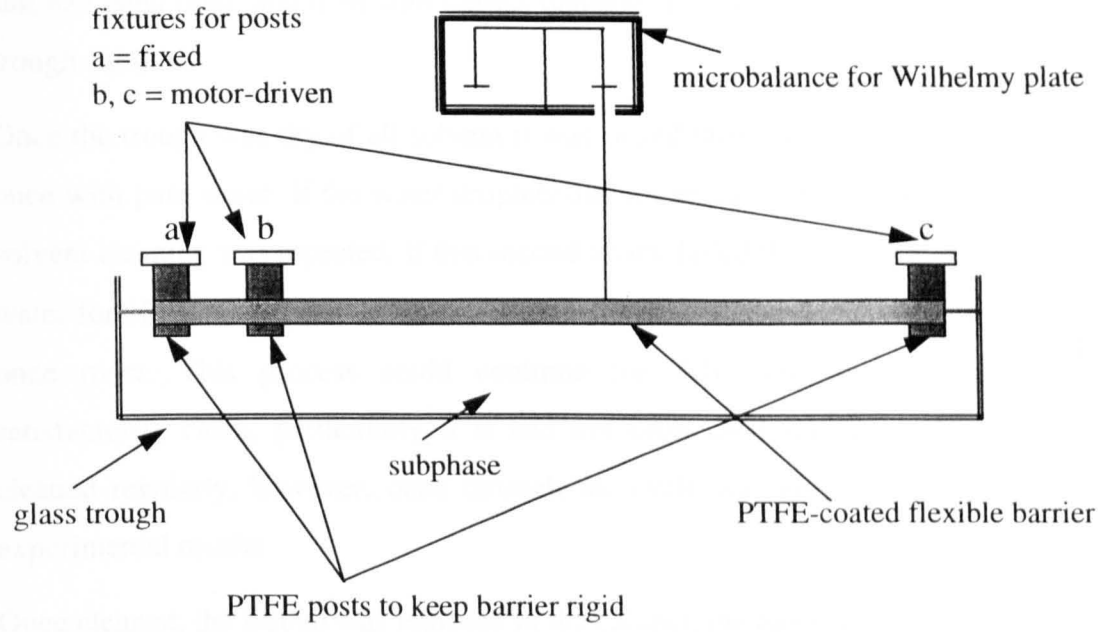

Figure 1 c) Schematic elevation view of a Langmuir trough with the barriers open.

4.2.1 Trough Cleaning

The trough was first emptied and the heating/cooling coil, if used, was removed from the trough and left in the cabinet. If a metal salt had been used the trough was rinsed out twice with pure water. It was then dried off with paper tissues. In a fume cupboard 10-15 ml of propan-2-ol was poured into the trough and this was used to clean the trough with the aid of a succession of lint-free cotton wipes (Radio Spares). The worker wore frequently-changed polythene gloves throughout (Fisons). Propan-2-ol was used to remove any water-soluble or water-miscible contamination. The procedure for propan-2-ol was repeated with dichloromethane to remove non-polar contamination and the trough was allowed to dry off. While the trough was drying, the cabinet was wiped down, using a clean-room tacky duster to prevent re-deposition of dust, and the band and posts were cleaned using paper tissues dampened with chloroform, to remove all traces of amphiphile. If the amphiphile was particularly stubborn it could be removed by sonicating the band and posts in a beaker of chloroform or other suitable solvent. If a heating/cooling coil was being used to control the subphase temperature, it was dried off at this stage and wiped down, firstly with tissues dampened with pure water, if a metal

salt had been used, and then with tissues dampened in chloroform, and left to dry in the trough cabinet.

Once the trough was dry of all solvent it was rinsed three times with distilled water and once with pure water. If the water droplets did not reveal a hydrophilic glass surface the solvent cleaning was repeated. If this second attack failed the trough was left full of pure water for 12-24 hours to leach out contaminants, rinsed, dried and cleaned with solvents once more. This process could continue for 7-10 days before the trough was satisfactorily clean, particularly if it had not been used for some time. If used and cleaned regularly, however, once through the cycle was enough to give reproducible experimental results.

Once cleaned, the trough was replaced in the cabinet, the band was fitted, it was checked with a spirit level to make sure it was level and filled with freshly-drawn pure water. On a monthly basis the microbalance and plotter signals were calibrated, including the ratio of the barrier-potentiometer volts to the trough area (this mV/cm^2 ratio was required for calculation of deposition ratios). If required, the subphase pH was adjusted to the desired value, e.g. pH3 using Aristar hydrochloric acid (Merck). If a metal salt was to be used it was added at this stage, e.g. 0.25 mM cadmium chloride (AnalaR, Merck) and the pH adjusted to 6.3 or above using AnalaR sodium hydroxide (May and Baker). The temperature of the subphase was allowed to stabilise, to room temperature or according to the heating/cooling coil, as appropriate. The trough was then ready for use.

The dimensions of the trough used for the bulk of the samples prepared here were 1.20 × 0.20 × 0.09 m. It was a gift from ICI Corporate Colloid Science Group and had been made there. The alternating trough used for ABAB samples was 0.80 × 0.40 × 0.12 m. It had been made and provided by DERA, Malvern (formerly RSRE). Both troughs consisted of a U-shaped piece of glass, with two glass end pieces held in place using a metal frame which could be tightened as necessary. A watertight seal was provided by mouldable expanded PTFE strip, 3-4mm diameter. All microbalances used had been purchased from CI Instruments. Motors and electronic components were standard off-the-shelf items, of good quality, and the circuitry, in particular the feedback loops, had been optimised for monolayer experiments through trial and error.

4.2.2 Cleaning of Glassware and Other Implements

The 2 ml volumetric flasks used to make up solutions of the amphiphiles were cleaned by sonicating for 30 minutes in a beaker containing a 2% solution of Decon90 (Merck) in distilled water. They were then rinsed by sonicating, in the same beaker, for 10 minutes in each of six changes of water, the first four being distilled water and the final two being pure water, and left to dry upside-down. Using the same beaker for all the sonicating steps helps to minimise contamination, especially from the stainless steel of the ultrasonic bath itself. The plastic tops were cleaned by soaking in a beaker of dichloromethane - since they float they were weighed down by a smaller beaker. They were then left to dry.

Spatulae used for weighing out were cleaned with a scouring powder such as Ajax and rinsed thoroughly with distilled water before being left to dry.

Larger items of glassware were soaked in a bucket filled with a 2% solution of Decon90 in distilled water for at least 12 hours, rinsed thoroughly under running distilled water and left to dry upside-down. All traces of surfactant had to be removed by rinsing: once dried on they were difficult to remove, even by sonicating.

The glass Agla micrometer syringes (Wellcome) were cleaned immediately after use by repeatedly drawing up and expelling clean chloroform, and then dried by drawing up and expelling air. Syringe needles were cleaned by sonicating for 10-15 minutes in each of three batches of chloroform and left to dry.

Wilhelmy plates were cut to the required size (1 cm x 2 cm) in large batches from Whatman filter paper, Qualitative grade. Each was rinsed in chloroform immediately prior to use and air-dried before immersion in the trough.

If drying of any of the above needed to be accelerated, cylinder nitrogen was used.

If any spatula or item of glassware was not uniformly hydrophilic after two or three cleans it was discarded from use in Langmuir trough experiments.

4.2.3 Cleaning of Substrates for Dipping.

The two most common dipping substrates are glass slides and silicon wafers. The former have a hydrophilic surface, and hence only pick up an odd number of layers, since no pick-up occurs on the first downstroke. The latter have a hydrophobic surface and so pick up an even number of layers.

Glass slides were purchased unwashed (e.g. Chance-Propper, UK), since residual surfactant from the manufacturer's cleaning process is too difficult to remove. They were first degreased by wiping with dichloromethane and then sonicated for 10 minutes in a bath of pure solvents, in the following order:

dichloromethane - propan-2-ol - water - propan-2-ol - dichloromethane - propan-2-ol - water - water.

Note that each solvent was miscible with the previous and the next in the sequence.

The slides were then sonicated for 30 minutes (or soaked overnight) in a 0.1M solution of sodium hydroxide. After this treatment the slides should be completely hydrophilic. If any were not they were discarded, as a second run through the procedure does not remove any further contamination. Finally, they were rinsed by sonicating for 10 minutes in each of 6 changes of water and dried with cylinder nitrogen before storing in a dust-free box.

Silicon wafers were purchased as reclaimed (e.g. Speedfam, UK) and all used in the present work were 4", (100) orientation, polished on one side only and doped n-type. First they were trimmed, to optimise the use of the compressed monolayer given the sampling area required by the neutrons and X-rays. They were then degreased, by rubbing first with chloroform and then with propan-2-ol, using lint-free wipes, before rinsing with distilled water. They were then etched for 10 minutes in 5% hydrofluoric acid to remove any remaining contaminants and the native oxide layer. A final rinse in water was used as the test to see how effective the cleaning had been - the surface should be completely hydrophobic, with no drops of water adhering at all. Note that the rear face of the wafers was ground and would therefore always be hydrophilic due to

capillary action. Each wafer was cleaned immediately before use, since the oxide would re-form over a period of about 10 minutes.

4.3 Langmuir Film Isotherms

Monolayers and their isotherms were produced as follows. Firstly, the water surface within the barrier was cleaned to remove surface-active contamination. This was done using a glass Pasteur pipette connected to a vacuum line and a water trap. The bulk of the surface was "hoovered" first, then all around the edges. The barrier was opened and closed rapidly, to dislodge any clinging dirt, and the "hoovering" was repeated. A fresh Wilhelmy plate was pierced at the top with a clean needle, cleaned in chloroform, dried in a paper tissue or in the air, attached to the microbalance using a length of cotton with wire hooks at each end and suspended into the water. It was handled throughout with clean tweezers. A final quick "hoover" removed any loose fibres of paper. The barrier was expanded, and on closing rapidly the microbalance signal was recorded. If the surface pressure increased by more than 0.1 mN/m the surface was re-hoovered and rechecked. It might be necessary to change the Wilhelmy plate or the chloroform it was cleaned in, or to clean the syringe needle used to make the hole for attachment to the microbalance. If the surface contamination persisted it might be necessary to empty the trough and clean it again, paying special attention to cleaning the flexible barrier (see section 4.2.1), and to check the quality of the pure water from the filters.

Once the water surface was satisfactory, the Langmuir film could be spread. A solution of the molecule under study was made up in chloroform or whatever solvent or mixture of solvents was appropriate. More than 10% alcohol in the mixture should be avoided, though, otherwise the material would be dissolved into the subphase by the alcohol and no monolayer would be formed. The solutions should be stored in the refrigerator, or the freezer for preference, to minimise concentration changes due to solvent evaporation from the flask. Next, the amount to be applied to the trough had to be calculated, using the simple formula shown below:

$$\text{Amount} = \frac{\text{initial trough area in square Angstroms} \times \text{RMM of molecule}}{\text{Avogadro's number} \times \text{initial area per molecule in square Angstroms}}$$

The initial area per molecule should be chosen so that the monolayer is well into the liquid-expanded region (Chapter 2, Section 2.2), and it should ideally be twice the close-packed area per molecule.

This equation gives the amount, in litres, of 1mg/ml solution to be applied to the trough. Use of an Agla micrometer syringe minimised errors in this process, since one complete turn of the micrometer (= a half-division) has been calibrated by the manufacturer to be 0.01 ml; this calibration was readily confirmed gravimetrically. The syringe needle was held about 3-5mm above the water surface and the solution was added dropwise. Each drop was allowed to spread (this was easily visible from the correct angle) before adding the next. If the needle was held too far above the water, the drops would fall straight through to the bottom of the trough without spreading, and thus introduce unknown errors in the intended area per molecule. If a drop failed to spread it was usually because there was already too much material on the surface. This would be confirmed by a significant surface pressure being observed, and would be the result of a wrongly-chosen initial area per molecule. Alternatively, the molecule may be sufficiently water-soluble to dissolve straightaway without spreading, and no amount of material would generate a significant surface pressure. Both situations are common when investigating unknown molecules.

Once the required amount of solution had been applied to the water surface, a minimum of 5 minutes was allowed for the solvent to evaporate. A longer time, say 10-15 minutes, might be needed if the subphase was below room temperature or if the solvent evaporated more slowly than chloroform. The barriers were then compressed slowly, typically 10% of the maximum area per minute, with area and surface pressure signals constantly monitored on the plotter. The resulting surface pressure versus area plot is termed an isotherm, since the data are collected at a constant subphase temperature. As discussed in Chapter 2, it reveals a wealth of information about the behaviour of the molecule under study. It must be stressed, however, that all experimental conditions

should be recorded for each isotherm, as this greatly simplifies the identification of any problems that may occur, such as with reproducibility. For example, a subphase temperature change of a few degrees or a difference of 0.5 pH units could have a marked effect on monolayer behaviour, with serious consequences for the understanding of a novel molecule. Similarly, irreproducible isotherms might be caused by trapped solvent, arising from inconsistent evaporation times. Rigorous attention to detail is therefore required at all times.

4.4 Surface Potential Measurement.

In addition to the information provided by isotherms, a further technique for studying monolayers is the use of surface potential [1], since fatty-acid monolayers floating on water are charged due to ionisation by the water. This technique measures the potential of a floating monolayer, using an ionised air gap. The circuit is completed by an $Ag/AgCl_2$ electrode immersed in the trough. A diagram of the apparatus is shown in Figure 2.

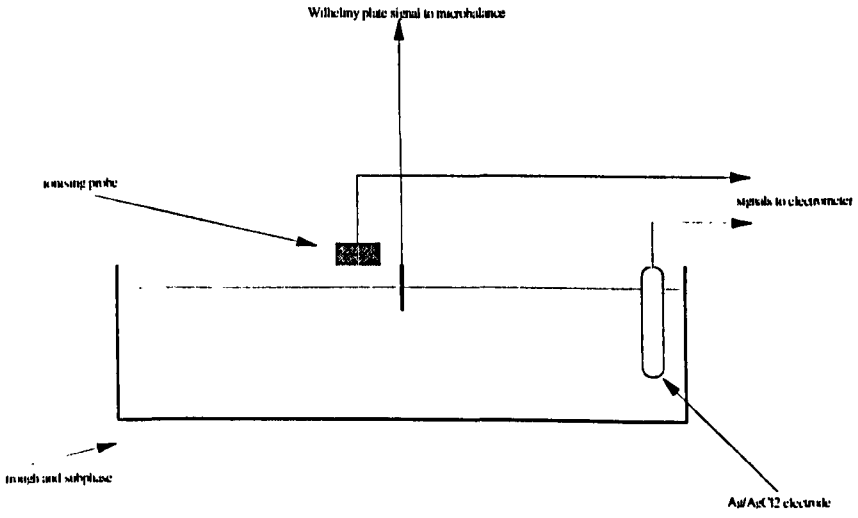

Figure 2 . Schematic diagram (elevation view) of the apparatus used for the measurement of surface potential. For clarity, the monolayer compression barriers have been omitted.

The air gap was ionised by an ^{241}Am α-source, which was used in preference to other radioactive elements because its γ-rays are very weak and so shielding and handling are comparatively straightforward. The trough was cleaned as usual and the probe was positioned over the centre of the trough, close to the Wilhelmy plate, at a height of 5 - 10 mm from the water surface, using a clamp and stand. It must stay at the same height throughout an experiment, in order to maintain the air gap at a constant thickness. If the probe is too close to the water, condensation affects the measurements.

The $Ag/AgCl_2$ electrode was filled with fresh electrolyte, rinsed thoroughly and placed in the trough. It was removed from the trough at the end of an experiment in order to minimise ions leaching into the subphase. A Keithley electrometer, model 610C, was used to provide the necessary resistance in the circuit, and the signal was recorded on an x-y-t plotter. One further point which must be made is that even with a low-noise coaxial cable connecting the probe to the electrometer, the movement of the operator close by can give rise to spikes in the signal, so it is important to remain at least 2m from the cable during an experiment, and to indicate any such artefacts on the plotter trace.

A measurement was first made of the clean water surface and typically this is -300 mV, although any steady value is acceptable, within the range ±500mV. The monolayer was then spread in the usual way, and after evaporation was complete, compression was started at the usual rate for an isotherm. There are two main ways to record the surface potential characteristics of a monolayer. The first is a surface potential isotherm, and the second is to monitor the surface potential, ψ, with time at a series of fixed surface pressures. The latter is more useful for providing data which will tie in with dipping results, and was the approach used here. The procedure used in the present work, and the results obtained, will be discussed in Chapter 5.

4.5 Langmuir-Blodgett Films.

Once a molecule had been well characterised as a monolayer and at least two isotherms were obtained which gave reproducible results within experimental error (typically 0.1 mN/m and 0.5 - 1.0 $Å^2$), LB film formation might be attempted. This level of reproducibility also shows that the trough is satisfactorily clean. First of all, a suitable surface pressure (π) value was chosen. This was usually a region of the isotherm where the monolayer was neither too fluid nor too stiff. For a fatty acid, this is in the S or LS region (see Chapter 2, section 2.2) and so π is generally 30 mN/m, at least for initial investigations. For dipping experiments it was not necessary to have an initial area per molecule as large as that used for isotherms - a value that was just in the liquid-expanded region was sufficient. This maximised the area available for dipping before a fresh monolayer needed to be spread, an important consideration for large substrates if they were not to take too long to dip. In order to establish the suitability of the material for dipping, the monolayer was compressed slowly to the chosen π (set point) using the Forward setting and held there using the Control setting (negative feedback loop) in the trough control box. Note that the Control dial setting is in mg, not mN/m (mg = 2 x mN/m for a 1 cm-wide filter paper Wilhelmy plate [1]).

If compression was too fast, or the Control setting was switched in too soon, the feedback loop would become unstable, since it was designed so that the speed which the Control setting used to approach the set point was directly proportional to the difference between the current π and the set point. For instance, if a fatty acid was being used and a set point of 35 mN/m was required, the Control setting must not be switched in before 30-33 mN/m. If it were switched in earlier, compression would be too rapid since the π difference would be too great. The set point would then be overshot, since the monolayer would be in its most rigid region where very little change in area produces a very large change in π, and the feedback loop would try to compensate, oscillating about the final π value. Under these circumstances the loop could easily go from negative feedback to positive. This would render the monolayer useless, since the amplitude of the

oscillations would have been sufficient to compress it into its collapsed region, so that it would no longer be homogeneous. For very rigid monolayers it might not be possible to reach equilibrium at all.

The pressure and trough area were monitored over time using an x-y-t plotter and the drift in area over, say, 30 - 60 minutes was noted. If this was significant, i.e. > 3 - 5 cm^2/min, the monolayer would be too unstable. It might be collapsing, or it might be dissolving into the subphase. If the latter, the trough surface would be difficult to clean, since the dissolved material would re-appear at the surface once the pressure was reduced. If the former, the barrier would be difficult to clean. Either way, it would be unsuitable for dipping at that pressure and alternatives would have to be investigated.

For some molecules, there is no pressure at which a monolayer is stable, even if subphase temperature, pH or metal ion concentration are altered. For the remainder, stability may usually be achieved under a variety of different experimental conditions, and may be enhanced further by "annealing". This is the process whereby a monolayer is compressed to a low π, say 5 mN/m, expanded again and allowed to relax for 10 minutes before being compressed up to the dipping π. It makes the monolayer more stable by gently forcing it into a loosely-packed version of the configuration it will adopt later. It is then relaxed at π = 0, to minimise the formation of microcrystallites, before being compressed up to the final pressure, at which it is now more stable. This treatment of the monolayer is particularly important when dipping fatty amines or phospholipids, and was used for the amines in the present work.

Once a suitable π had been determined, the first few samples could be dipped. The dipping speed was the next factor to optimise - some molecules need a very slow speed, of the order of 1-2 mm/min, while others might need to be dipped fast, at 20mm/min or faster. The meniscus was an excellent qualitative guide to the evenness of transfer. On the downstroke it should be downwards, on the upstroke it should be upwards, and in both directions it should be smooth - if there was any unevenness, static or moving, it was indicative of poor deposition and this would be borne out by the transfer ratio and any subsequent film characterisation.

Once all these parameters had been optimised, samples could be prepared in earnest. For a full list of those prepared in the present work, see Table 1 in Chapters 5 and 6.

To prepare films with one labelled bilayer, all the lower H-layers were deposited first across the whole batch, then all the D-layers, and then the final H-layers. This minimised the number of monolayer changes required on the trough, and hence minimised the risk of cross-contamination. Typically, it was possible to prepare seven 10-layer samples in two days.

To prepare ABAB films, a two-compartment trough was used, a schematic diagram of which is shown in Figure 3. Full details of the trough design are provided in [2]. The substrate must be fully immersed, so that the narrow section of the holder is the part that passes through the gate, otherwise the gate is opened too far and monolayer leaks from one side to the other. The speed at which the substrate was passed from one compartment to the other was about 20mm/min (0.18 on the control box dial). Typically, it was possible to prepare seven 10-layer samples in four days. ABAB samples require more time to prepare as there is far less monolayer area available, and so the monolayers must be replenished far more frequently than is required for the single-compartment trough.

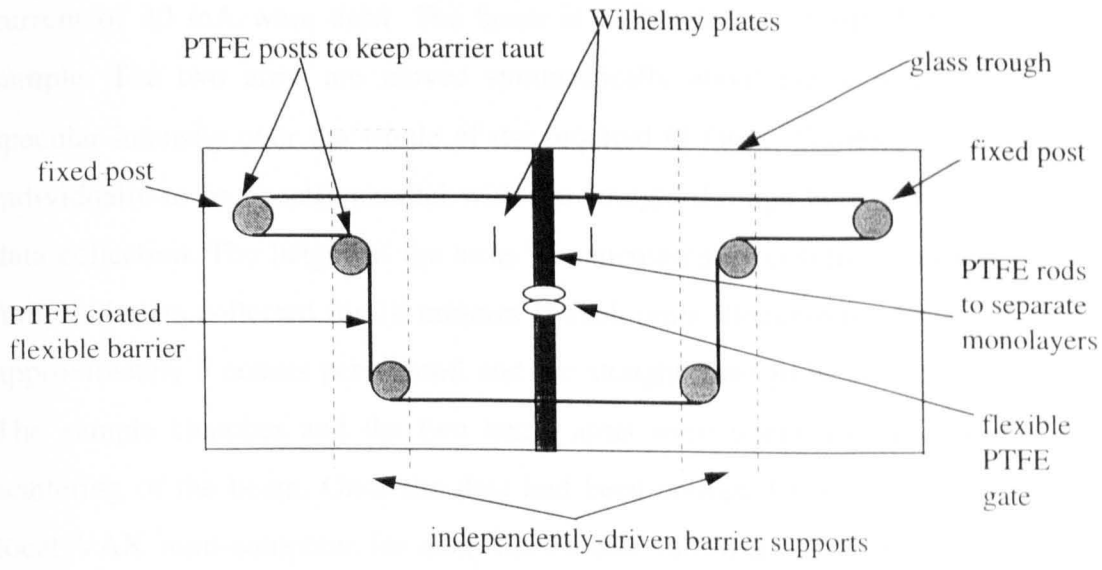

(caption overleaf)

Figure 3 Plan view of a two-compartment Langmuir trough, showing the two independent barriers at intermediate positions.

LB films should be totally dry on withdrawal, but some molecules form films which may be partially wet. These must be allowed to dry before re-immersion, otherwise the trapped water will carry the top layer from the substrate back onto the monolayer and further deposition will be patchy. Some molecules may only deposit one layer on a hydrophilic substrate, or two on a hydrophobic one, and the top layer will peel off on re-immersion, to redeposit on withdrawal, i.e. no further deposition can be achieved.

To conclude, LB dipping is a fundamentally simple process, but one affected by a bewildering variety of parameters. Close attention to detail is needed at all stages of preparation and film formation if the character and structure of a dipped film are to be understood.

4.6 X-ray Reflectivity.

The reflectometer used in this work was custom built in Bristol. Figure 4 shows a schematic diagram of the apparatus. For the present samples, a voltage of 30 kV and a current of 30 mA were used. The beam is collimated by 2 slits before reaching the sample. The two arms are moved symmetrically about the sample so as to record specular intensity over the whole of the required Q range. Samples were each aligned individually to be exactly parallel with the straight-through beam, before commencing data collection. The height of the arms was increased from 0 to 30 mm in steps of 0.2 mm, with data collected for 10 minutes at each point. Background for the instrument is approximately 5 counts per second and the straight-through beam is about 10 000 cps. The sample chamber and the two beam arms were under vacuum to minimise air-scattering of the beam. Once the data had been collected they were transferred to the local VAX mini-computer for analysis. Further information on the use of the Bristol reflectometer is contained in [3].

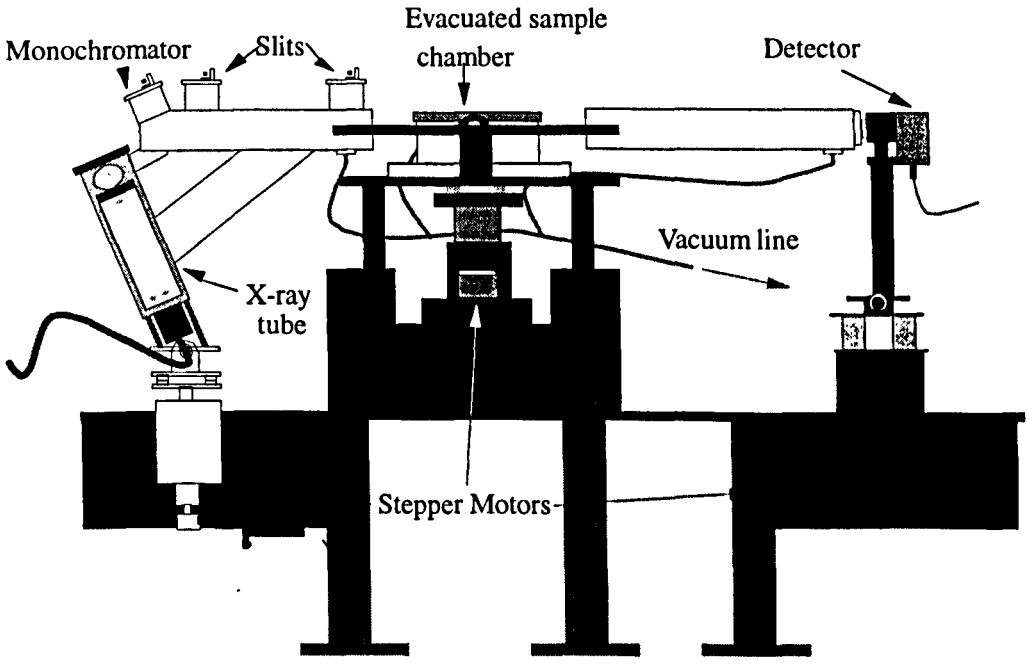

Figure 4 Diagram of the X-ray reflectometer at Bristol, courtesy of Neil Phillips, Bristol.

4.7 Neutron Reflectivity.

If a beam of protons is fired at a tantalum or uranium target, neutrons are produced with high energies and hence very short wavelengths. At the Rutherford Appleton Laboratory, UK, the pulsed neutron spallation source, ISIS, directs these neutrons at a variety of instruments which are used to study atomic and molecular structure. The moderator used by each instrument determines the wavelengths available to it. For the two reflectometers used in this work, CRISP [4] and the new instrument SURF [5], the moderator is liquid hydrogen (25K) and the beamlines have a wavelength range of 0.5 - 6.5 Å when a 50Hz chopper is used. Since the beam is white, the sample does not need to be moved during an experiment. The pulsed nature of the beam means that the time-of-flight of the neutrons enables their energy, and hence their wavelength, to be calculated. Slow neutrons are removed from the beam using a chopper and a frame-overlap mirror, thus preventing them from overlapping with neutrons in the next pulse. The beam is collimated using two slits before the sample, and off-specular neutrons are eliminated by two slits after the sample (not shown in Figure 5). The widths of these slits must be adjusted for each incident angle to ensure that the experimental resolution remains constant throughout the experiment. The reflected beam is normalised against the incident beam to obtain reflectivity values. Figure 5 shows a generic diagram of a reflectometer at the Rutherford Appleton Laboratory (RAL). In practice, for LB film systems there is very little difference between CRISP and SURF and the use thereof.

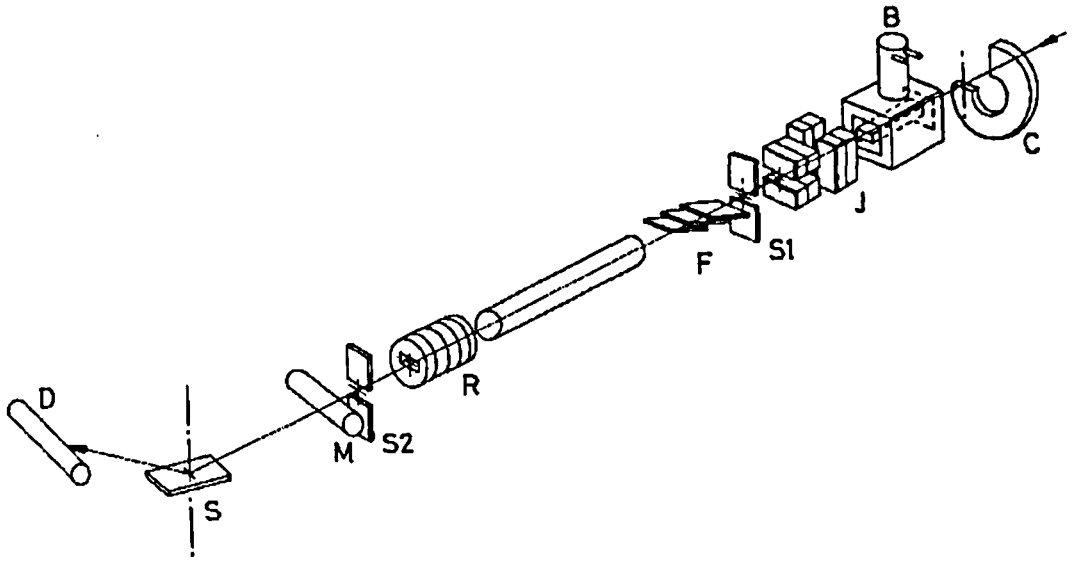

Figure 5 Diagram of a neutron reflectometer at RAL. C is the chopper, B the beryllium filter, J the coarse collimating jaws, S1, S2 the collimating slits, F the frame overlap mirrors, R the downstream collimation, M the neutron beam monitor, S the sample and D the He detector. Diagram courtesy of RAL.

Each sample is aligned individually on the sample changer before starting data collection. In order to sample the whole Q range, data must be collected at several different incident angles. For LB films these are typically 0.25°, 0.6° and 1.5°, giving a Q range of 0.008 - 0.6 $Å^{-1}$. Once collected, data must first be reduced and normalised with respect to the incident beam, and subsequent analysis was done either on the computers at RAL or locally in Bristol. Details of the data analysis are given in Chapters 5 and 6, the relevant theory having been discussed in Chapter 3.

4.8 References

[1] G. L. Gaines, Monolayers at Liquid-Gas Interfaces, p.46 (Wiley, New York, 1966).

[2] M. F. Daniel, J. C. Dolphin, A. J. Grant, K. E. N. Kerr and G. W. Smith, Thin Solid Films, **133**, 235 (1985).

[3] A. Zarbakhsh, Instructions for Using the Bristol X-ray Reflectometer, 1995.

[4] J. Penfold, R. C. Ward and W. G. Williams, J. Phys E, **20**, 1411 (1987).

[5a] D. G. Bucknall, J. Penfold, J. R. P. Webster, A. Zarbakhsh, R. M. Richardson, A. Rennie, J. S. Higgins, R. A. L. Jones, P. Fletcher, R. K. Thomas, S. Roser and E. Dickinson. "SURF - A Second Generation Neutron Reflectometer". Paper presented at the 13th Meeting of the International Collaboration on Advanced Neutron Sources, Switzerland, October 11th - 14th, 1995.

[5b] J. Penfold, R. M. Richardson, A. Zarbakhsh, J. R. P. Webster, D. G. Bucknall, A. R. Rennie, R. A. L. Jones, T. Cosgrove, R. K. Thomas, J. S. Higgins, P. D. I. Fletcher, E. Dickinson, S. J. Roser, I. A. McLure, A. R. Hillman, R. W. Richards, E. J. Staples, A. N. Burgess, E. A. Simister and J. W. White, J. Chem. Soc. Faraday Trans. **93**, 3899 (1997).

Chapter 5. Simple Fatty Acid Films.

5.1 Introduction.

This chapter describes the work done with simple fatty acids, and illustrates the importance of dipping conditions in determining the quality and structural integrity of an LB film. It also illustrates the inadequacies of using over-simplified modelling approaches to analysing the data and describes the evolution of a satisfactory model to fit the data more completely than has hitherto been achieved for LB films.

5.2 Experimental.

As mentioned in Chapter 2, section 2.3, a total of seven parameters were varied independently: dipping speed, dipping pressure, position of labelled layer, subphase pH, temperature and ions, and time under water. Table 1 lists the samples prepared for this part of the work. All were examined by both neutron and X-ray reflectivity, with the exception of S8 and S9 which were prepared on nickel substrates for instrument scientists at ISIS studying polarised neutrons. They are mentioned here simply for the sake of completeness. In addition, due to time constraints at ISIS there are no neutron data for samples S5 and S6, although the structure of S5 was repeated at a later date as S12. The polymer referred to as P in Table 1, illustrated diagrammatically in Figure 1, was used in this work with the aim of linking in to previous work done by Dr Richardson's group. [1]

All samples were dipped onto silicon wafer substrates, prepared as described in Chapter 4, Section 4.2.3. The subphase used was 18 MΩ water, with the pH adjusted to pH ~3 and at ambient temperature, i.e.17-19°C, with the following exceptions:

S10 and S11 were dipped over a subphase containing 2 x 10^{-4} M cadmium chloride at pH 6.3. S6, S14 and S15 were left underwater for 10 minutes between the downstroke and upstroke of the deuterated bilayer. S24 was dipped over a subphase at 30°C.

Sample number	Structure	Dipping pressure, mN/m.	Dipping speed, mm/min
S1	HHDHH	40	15
S2	HHHHD	40	15
S3	HHDHH	30	5
S4	HHHHDHHHH	40	15
S5	HHDHH	40	15
S6	HHHHDHHHH	40	15
S7	DHHHH	40	15
S8 (Ni)	HHHHD	40	15
S9 (Ni)	DHHHH	40	15
S10	HHHHD	40	15
S11	DHHHH	40	15
S12	HHDHH	40	15
S13	HHHHDHHHH	35	15
S14	HHDHH	35	15
S15	HHHHDHHHH	35	15
S16	HHDHH	40	5
S17	HHDHH	30	15

...cont.

Sample number	Structure	Dipping pressure, mN/m.	Dipping speed, mm/min
S18	PPPPD	P 11, D 40	15
S19	PPDPP	P 11, D 40	15
S20	DPPPP	P 11, D 40	15
S21	DDDDP	P 11, D 40	15
S22	DDPDD	P 11, D 40	15
S23	PDDDD	P 11, D 40	15
S24	HHHHD	40	15
S25	HHHHD	25	15
S26	HHHHD	25	5
S27	HHHHD	20	15
S28	HHHHD	20	5
S29	HHHHD	15	15
S30	HHHHD	15	5
S31	PPPPD	P 11, D 20	15
S32	PPDPP	P 11, D 20	15
S33	DPPPP	P 11, D 20	15

...cont.

Sample number	Structure	Dipping pressure, mN/m.	Dipping speed, mm/min
S34	HHHHH	30	15
S35	**DDDDD**	30	15
S36	**DDDDD**	30	5
S37	**DDDDD**	35	15
S38	**DDDDD**	25	15
S39	PPPPP	11	15

Table 1. The fatty acid samples prepared. Each letter in the Structure column represents a bilayer. H - docosanoic acid, **D** - perdeuterated docosanoic acid, P - side-chain liquid crystal polymer shown in Figure 1.

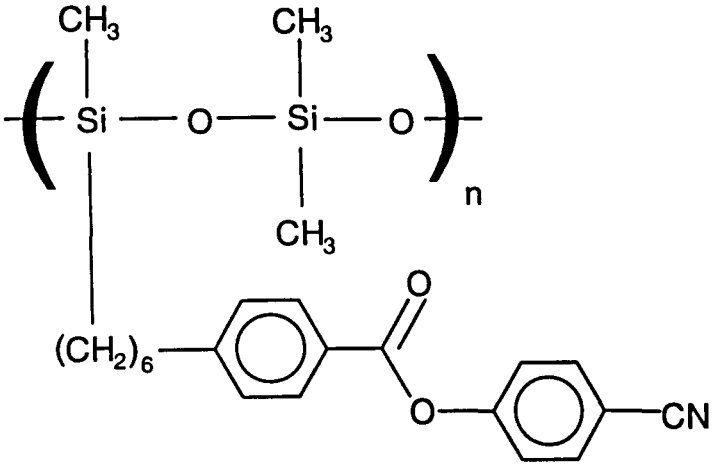

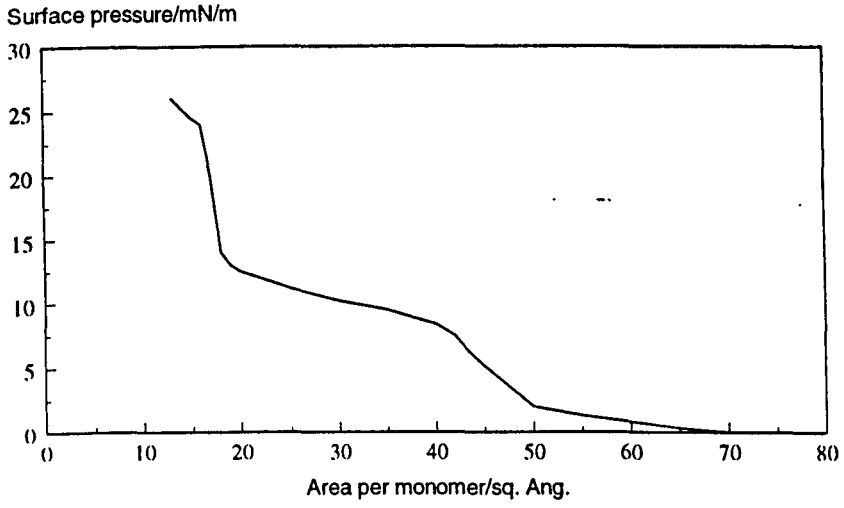

Figure 1 a) Showing the structure of the polysiloxane referred to as P in Table 1. n is approximately 6; b) the isotherm of the polymer on pure water, pH5.5, at 18°C.

5.3 Modelling.

Reference [2] gives an excellent overview of the main problems encountered in fitting reflectivity data. The discussion here will be restricted to those problems relating solely to LB film-type structures.

The MULF multi-layer fitting routine in the Genie suite of programs at ISIS was used initially to try to fit the neutron data, but proved inadequate due to the limitations of the slab-wise approach to SLD profiles. If the SLD of each slice is left to float independently, there are not enough constraints available to keep the model within the bounds of reasonable film and layer thickness and SLD values, given the known nature of the LB films. MULF proved extremely cumbersome even for fitting the X-ray data, where there is less complexity in the structure than with neutrons; again, it was difficult to constrain the model to reasonableness. This is illustrated in Figure 2, which shows clearly how limited the modelling is.

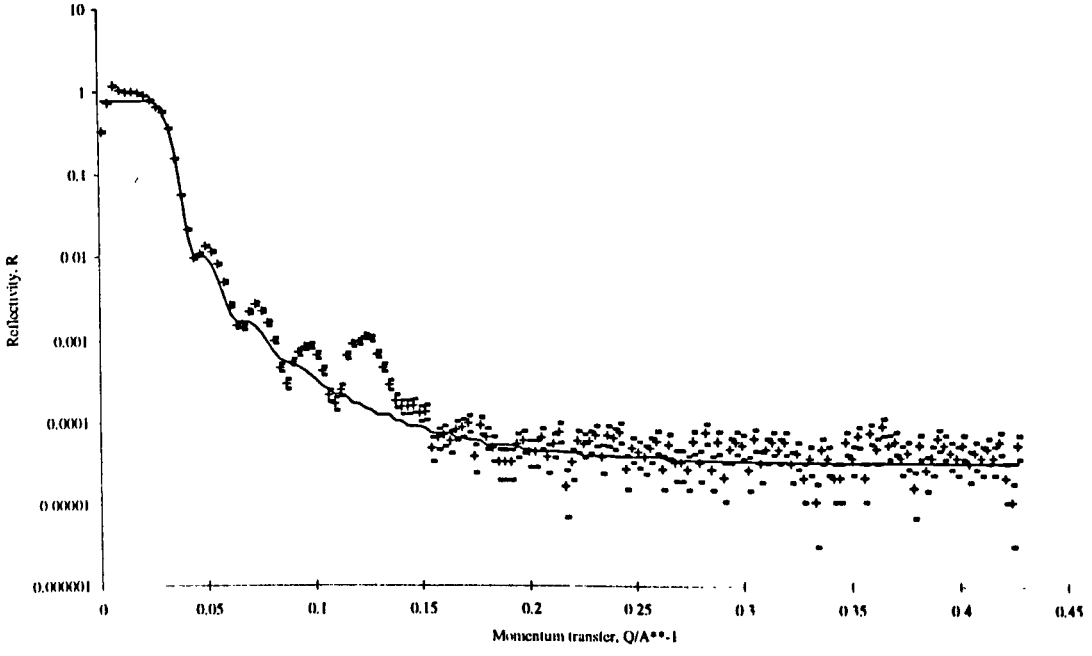

Figure 2a) Showing the best fit (solid line) obtainable using MULF to fit X-ray reflectivity data for S2 (points) using a single-layer model. Errors are shown by the small dashes above and below each data point.

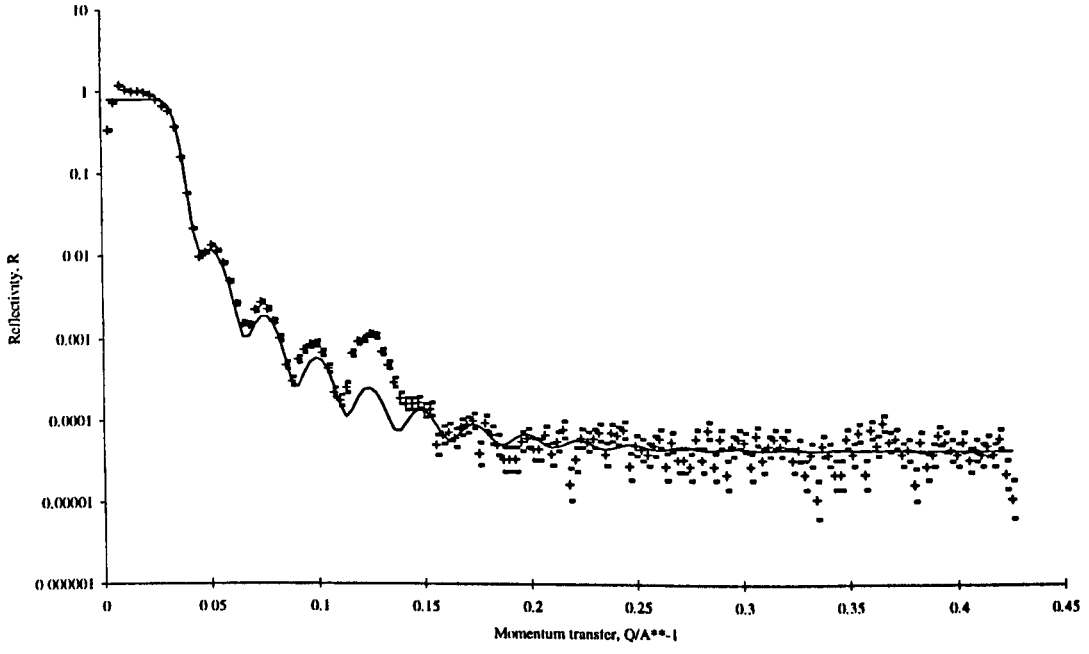

Figure 2b) Showing the best fit (solid line) obtainable using the single-layer fitting routine in Fitnew to fit X-ray reflectivity for S2 (points). Errors are shown by the small dashes above and below each data point.

Fitnew is an in-house suite of routines written by Dr. R.M. Richardson, initially for the analysis of X-ray and neutron reflectivity data from polymer films. It uses optical matrix formalisms to calculate reflectivity profiles (see Chapter 3, section 3.3.3) and is based on the same VA05a least-squares fitting engine as MULF. Its strength is due both to far greater flexibility of input parameters and whether they are fixed or floating than is possible with the MULF, and also to the possibility of fitting data within a particular Q-range where the data are good, rather than the whole profile. It has been enlarged and diversified to cover the fitting requirements of a variety of systems, including LB films. The evolution of the modelling approaches used for LB films, which culminated in the successful modelling of the data in this present work, will now be described. The Fortran programming itself was done by Dr. Richardson.

Using the same approach as Chapter 3, to facilitate comprehension the kinematic approximation will be used to describe and illustrate the evolution of the model used in this work. The Fitnew suite itself, as stated above, uses optical matrix methods exclusively for the calculations and the results are, therefore, valid over the entire Q range. Where the gaussian model was used, the number of discrete layers for the optical matrix model was optimised to give a smooth variation in scattering length from step to step without requiring excessive computer processing time. This was of the order of 100 layers for a 250Å thick film, i.e. each layer encompasses approximately two CH_2 units. Typical times to run a model on the DEC Alpha VAX in the University of Bristol Physics Department varied from one or two minutes to several hours, depending on how many parameters were floating. Most of the models were chosen and set up so as only to require computing times of the order of 2 - 5 minutes, since a large number of rapid results such as these enabled faster solution overall than a few models floating several parameters at once and waiting rather longer per model, as well as enabling the author to maintain close control over the ranges of the parameters, given the known isotopic composition of the films.

The first step was the introduction of a repeating nature within the model, enabling hydrocarbon chains and headgroups to be more easily fitted. In addition, the percentage of deuterated chain in each monolayer could be varied and floated. However, the model still assumed that the deutero-layer was a definite slab, and so no satisfactory fits to neutron data were obtained, although X-ray data were fittable with this model.

Having established that a slab approach did not allow close fitting of LB film neutron reflectivity data, the next idea was to try to model the deutero-layer as a triangular function in SLD. This looked promising and was made more realistic by using a gaussian to describe the SLD profile around the deutero-layer and smaller gaussians to describe the SLD profile of the headgroups. Figure 3 defines the parameters used and the mathematics of the model are given below.

The equation for a gaussian curve has the general form

$$y = \exp -\left(\frac{x^2}{2\sigma^2}\right) \qquad (5.1)$$

where σ is as defined in Figure 3 and is given below.

Where a gaussian of width σ is used to approximate a block function of width d, the relationship between their respective widths is given by

$$\sigma = \frac{d}{\sqrt{12}} \qquad (5.2)$$

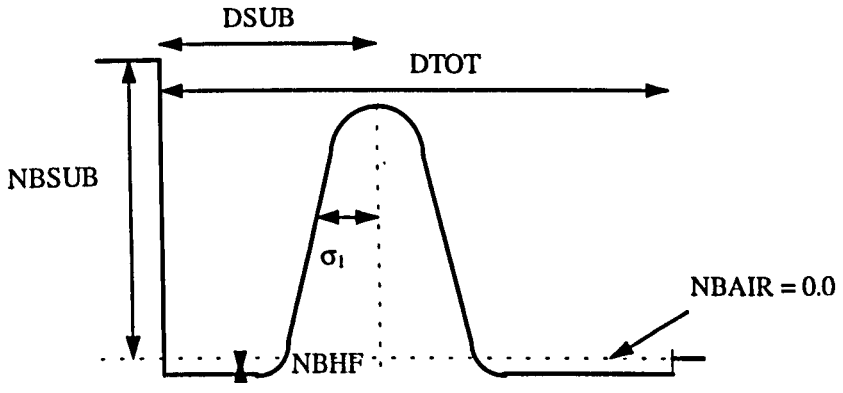

Figure 3a) Schematic diagram defining the parameters used in the gaussian model for fitting LB film reflectivity data. NBSUB is the SLD of the substrate, NBHF is the SLD of the non-deuterated component of the film, DSUB is the distance from the substrate to the centre of the gaussian, DTOT is the total thickness of the film and σ_1 is the parameter for the width of the gaussian.

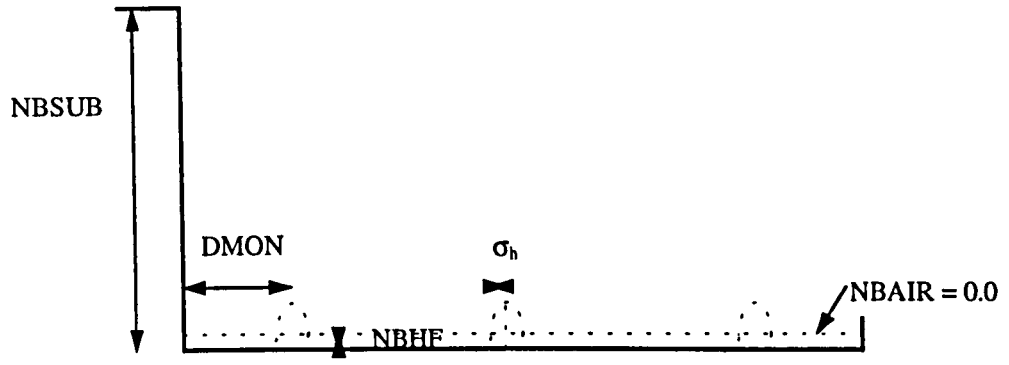

Figure 3b) Schematic diagram defining the parameters used to model the headgroups. NBSUB and NBHF as in Figure 3a). DMON is the monolayer height, i.e. half the Bragg repeat distance. σ_h is the parameter describing the width of the gaussians representing the headgroup regions. This model is superimposed on the one in Figure 3a) to give a full description of the structure of the LB film.

First define the SLD profile of the film, $\rho(z)$:

$$\rho(z) = \rho^0_S \tfrac{1}{2}[1 - H(z)] + \rho_H(z) + \rho_D(z) \qquad (5.3)$$

where

ρ^0_S is the SLD of the substrate

$\tfrac{1}{2}[1 - H(z)]$ is the Heaviside function describing the drop in SLD between the substrate and the LB film

$\rho_H(z)$ is the SLD of the non-deuterated part of the film, calculated in two parts as follows:

If there is no scrambling and the H-film is pure, $\rho_H(z)$ is given by

$$\rho_H(z) = \left(\frac{\Sigma b_H}{A}\right) \times \frac{1}{DMON} \qquad (5.4)$$

where

Σb_H is the sum of scattering lengths for the H-molecule and

A is the area per molecule within the film.

If some of the H-molecules have been displaced by D-molecules, $\rho_H(z)$ is given by

$$\rho_H(z) = \left(\frac{\sum b_H}{A}\right) \times \left\{ \frac{1}{DMON} - \frac{1}{\sigma\sqrt{2\pi}} \exp - \left(\frac{(z-d)^2}{2\sigma^2} \right) \right\} \qquad (5.5)$$

where d is the position of the maximum of the gaussian in the z-direction.

$\rho_D(z)$ is the SLD of the deuterated part of the film, and is given by

$$\rho_D(z) = \left(\frac{\sum b_D}{A}\right) \frac{1}{\sigma\sqrt{2\pi}} \exp - \left(\frac{z^2}{2\sigma^2} \right) \otimes \delta(z-d) \qquad (5.6)$$

where Σb_D is the sum of scattering lengths over the D-molecule and

$\delta(z-d)$ is the delta-function at the centre of the gaussian.

Hence

$$\rho_D(z) = \left(\frac{\sum b_D}{A}\right) \frac{1}{\sigma\sqrt{2\pi}} \exp - \left(\frac{(z-d)^2}{2\sigma^2} \right) \qquad (5.7)$$

and $\rho(z)$ is given by

$$\rho(z) = \rho_S^0 \tfrac{1}{2}[1 - H(z)] + \frac{\sum b_D - \sum b_H}{A} \frac{1}{\sigma\sqrt{2\pi}} \exp - \left(\frac{(z-d)^2}{2\sigma^2} \right) + \frac{\sum b_H}{A} \frac{1}{DMON} \qquad (5.8)$$

The term $\frac{\sum b_D - \sum b_H}{A}$ is denoted by B_A in the parameter lists and is the quantity that determines the area under the gaussian.

The term $\frac{1}{\sigma\sqrt{2\pi}}$ is required to keep the area under the gaussian constant for a particular fit, regardless of how σ changes in the course of that fit.

The term $\frac{\sum b_H}{A} \frac{1}{DMON}$ is the SLD of the pure H-film and is denoted by NBHF in the parameter lists.

The reflectivity from this SLD profile is given by the kinematic approximation, as follows:

$$R(Q) = \frac{16\pi^2}{Q^2}|\hat{\rho}(Q)|^2 \qquad (5.9)$$

where $\hat{\rho}(Q)$ denotes the one-dimensional Fourier Transform of $\rho(z)$ and $\hat{\rho}(Q)$ is given by

$$\hat{\rho}(Q) = \int_{-\infty}^{\infty} \exp(iQz)\, \rho(z)\, dz \qquad (5.10)$$

Substituting for $\rho(z)$ in the above integral, and using the standard result for the Fourier Transform of a gaussian,

$$\hat{\rho}(Q) = \rho_s\left\{2\pi\delta(Q) - \pi\delta(Q) + \frac{i}{Q}\right\} + \frac{\sum b}{A}\exp -\left(\frac{Q^2\sigma^2}{2}\right)\exp - iQd \qquad (5.11)$$

Using de Moivre's theorem, namely $e^{i\theta} = \cos\theta + i\sin\theta$,

$$\hat{\rho}(Q) = \rho_s\pi\delta(Q) + \frac{\sum b}{A}\exp -\frac{Q^2\sigma^2}{2}\cos(Qd) - i\left(\frac{\rho_s}{Q} - \frac{\sum b}{A}\exp -\left(\frac{Q^2\sigma^2}{2}\right)\sin(Qd)\right) \qquad (5.12)$$

Hence

$$|\hat{\rho}(Q)|^2 = \left(\rho_s^0\pi\delta(Q) + \frac{\sum b}{A}\exp-\left(\frac{Q^2\sigma^2}{2}\right)\cos Qd\right)^2 + \left(\frac{\rho_s}{Q} + \frac{\sum b}{A}\exp-\left(\frac{Q^2\sigma^2}{2}\right)\sin Qd\right)^2 \qquad (5.13)$$

The term $\rho_s^0\pi\delta(Q) = 0$ at $Q > 0$, giving

$$|\hat{\rho}(Q)|^2 = \left(\frac{\sum b}{A}\right)^2 \exp-(Q^2\sigma^2) + \left(\frac{\rho_s}{Q}\right)^2 + 2\frac{\rho_s}{Q}\frac{\sum b}{A}\exp-\frac{Q^2\sigma^2}{2}\sin Qd \qquad (5.14)$$

substituting for $|\hat{\rho}(Q)|^2$ in the equation for R(Q),

$$R(Q) = \frac{16\pi^2\rho_s^2}{Q^4} + \frac{16\pi^2}{Q^2}\left\{\left(\frac{\sum b}{A}\right)^2 \exp -\left(Q^2\sigma^2\right) + 2\frac{\rho_s}{Q}\frac{\sum b}{A}\exp -\frac{Q^2\sigma^2}{2}\sin Qd\right\}$$

(5.15)

$\frac{16\pi^2\rho_s^2}{Q^4}$ is the substrate term

$\left(\frac{\sum b}{A}\right)^2 \exp -\left(Q^2\sigma^2\right)$ is the monotonic term arising from the D-labelled layer

$2\frac{\rho_s}{Q}\frac{\sum b}{A}\exp -\frac{Q^2\sigma^2}{2}\sin Qd$ is the term describing the damped fringes from the interference between the substrate and the D-layer.

A further refinement was the two-sided gaussian model, where the deutero-layer is described by a non-symmetrical function consisting of two half-gaussians of the same height and the headgroup gaussians are again superimposed. Figure 4 shows the extra definitions introduced. This proved much better for the acid-amine data discussed in Chapter 6, where the deutero-layer was deposited as a single monolayer, but still did not give close fits over the whole Q-range for samples with the deuterated material deposited as a bilayer. For these samples, the two-sided gaussian model proves somewhat insensitive to whether σ_1 or σ_2 is the larger, unless the difference in size is greater than 8 - 10 Å, and so the symmetrical gaussian model has been used for preference, except for those samples where the D-layer is at the air-film interface. In the case of these, σ_2 was fixed at a value representing one monolayer while σ_1 was floated independently.

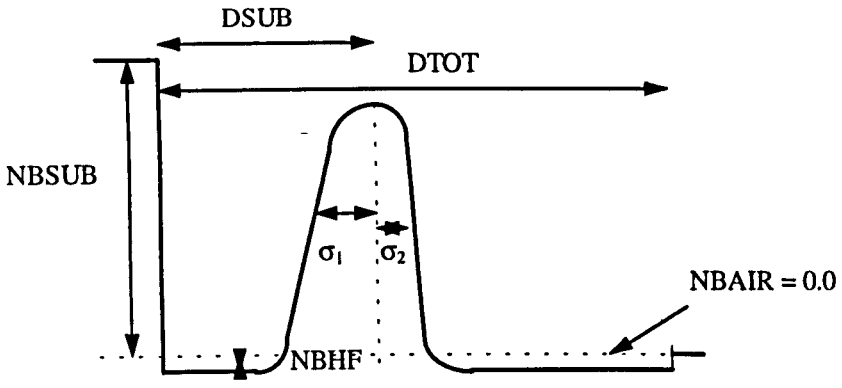

Figure 4 Showing the definitions used for the two-sided gaussian model.

The final refinement was the introduction of a block of variable width between the two half-gaussians of the previous model, i.e. regarding the half-gaussians as error functions on either side. This has so far given encouraging results for close fits to reflectivity data from samples with a deutero-bilayer but has not yet been exhaustively tested.

There are two clear limitations to using a gaussian modelling approach. The first is that the model is inherently unable to deal with the case of the D-layer positioned at the substrate, although it is envisaged that the block model with two half-gaussians will be more appropriate for this type of sample, with σ_1 set to a vanishingly-small value. Hence, unfortunately, it has not been possible to model those samples prepared here with the D-layer at the silicon. The second limitation is due to the shape of the Fourier Transform of the differential of a gaussian. The differential is a broad function, and hence its Fourier Transform is a damping function, and therefore the model cannot be expected to model high-Q data (above Q ~ 0.1 $Å^{-1}$) since the modelled reflectivity will be too damped to match the observed reflectivity. Nevertheless, the data up to Q ~ 0.1 $Å^{-1}$ contain much information on the internal structure of the LB film, so the limitation is not a serious one at this stage. This damping effect is illustrated in Figure 5. Note that, damping notwithstanding, the model has still generated all the features seen in the data. Below Q = 0.1Å, the fit is excellent. (χ^2 is defined in the next Section.)

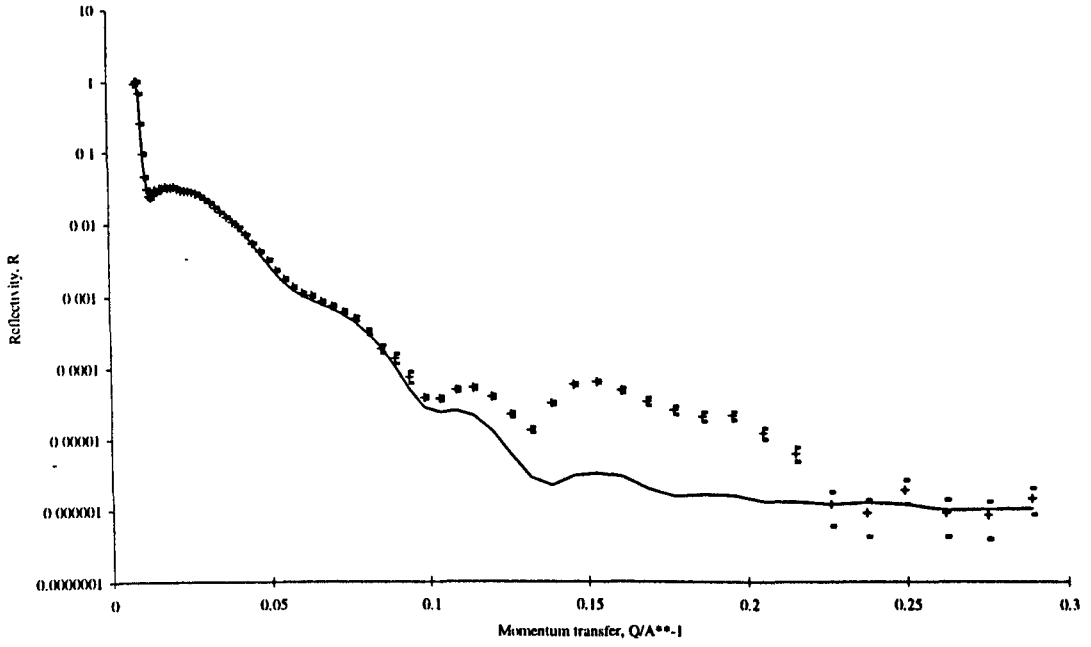

Figure 5 Showing the damping inherent in the gaussian model above Q = 0.1 $Å^{-1}$. Neutron data from S1 (points), fit (solid line). Errors are shown by the small dashes above and below each data point. Details of the parameters which gave this fit are in Tables 2 and 3. $\chi^2 = 1.8$ in the Q region 0 - 0.1$Å^{-1}$.

5.4 Results.

5.4.1 X-ray and Neutron Results.

The X-ray data were fitted using the single-layer option in the Fitnew suite, to keep the models extremely simple and therefore extract the required information more easily. The details of the large-scale structure of the films, such as the total thickness DTOT and the mean electron density NBHF, are contained in the low-Q part of the reflectivity profile, owing to the reciprocal relationship between Q and feature size. Thus DTOT and NBHF may be extracted by fitting X-ray data in the Q region 0.0 to 0.1 $Å^{-1}$.

The neutron data were fitted over the same Q-range, for the reason discussed at the end of the previous section. The symmetrical gaussian model was used to extract information on DSUB and neutron B_A.

Examples of the quality of fit obtained are shown in Figures 6 and 7 for X-ray data and Figures 8 and 9 for neutron data. DTOT values are shown in Table 2 along with DSUB values, while X-ray NBHF and neutron B_A values are shown in Table 3, along with the film densities calculated therefrom.

The errors quoted in the tables are a measure of confidence in the fits - if a small change in a particular parameter causes the quality of the fit (as measured by the least-squares method) to deteriorate significantly, the confidence in that fit is high and the error concomitantly low. This may be rephrased as the contours around that particular minimum in solution space being very steep, increasing the confidence in that minimum being a global one for the sample concerned. Conversely, if a small change in a parameter has no significant effect on the quality of the fit then confidence in that fit is low and the error large - the minimum in solution space is shallow and broad and therefore unlikely to be global. For comparison, χ^2 values are given for each fit in the respective figures. χ^2 is the value of $\frac{\sum(\text{observed} - \text{expected})^2}{\text{number of data points}}$. For a perfect fit between model and data, $\chi^2=1$.

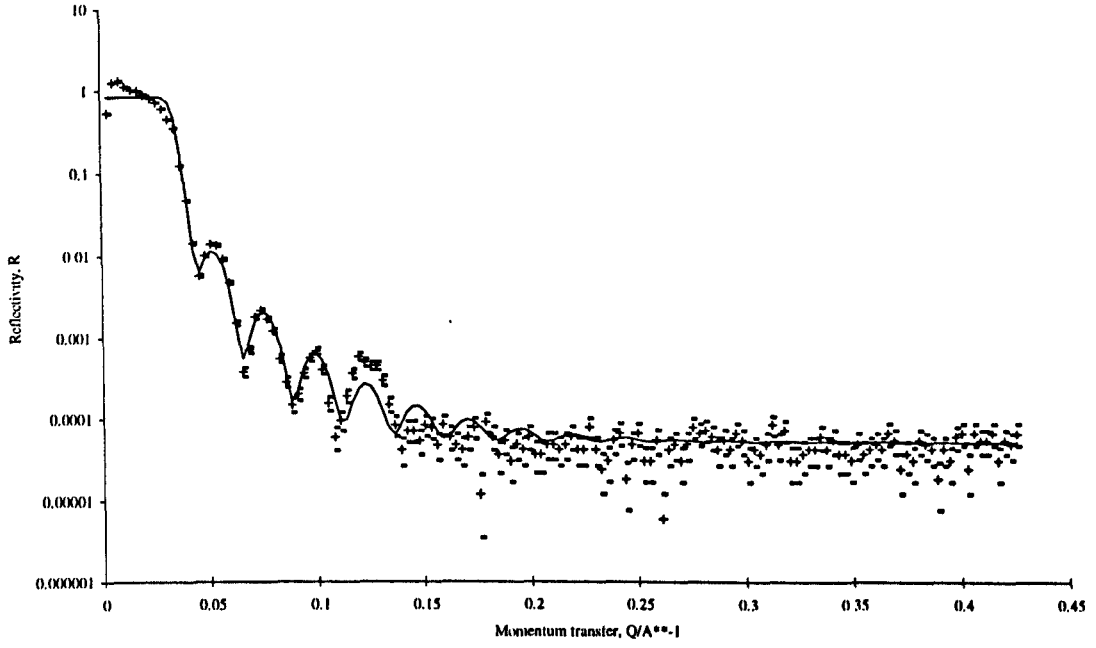

Figure 6 Showing the high quality fit (solid line) obtained using a single-layer model, for the X-ray data from S14 (points). χ^2=13.5. Errors are shown by the small dashes above and below each data point.

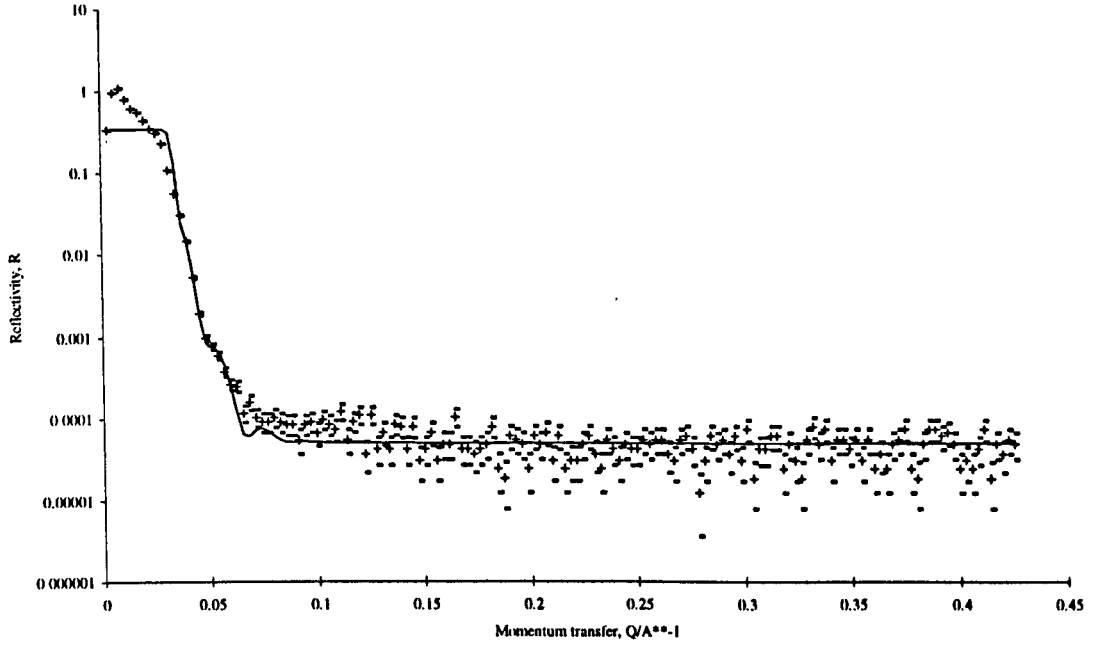

Figure 7 Showing the best fit obtained (solid line) using a single-layer model for X-ray data for S23 (points). Note how poor alignment has resulted in poor data around Q_c , and how this has been prevented from being a problem by de-emphasising the data in that region within the model. χ^2=21.8. Errors are shown by the small dashes above and below each data point.

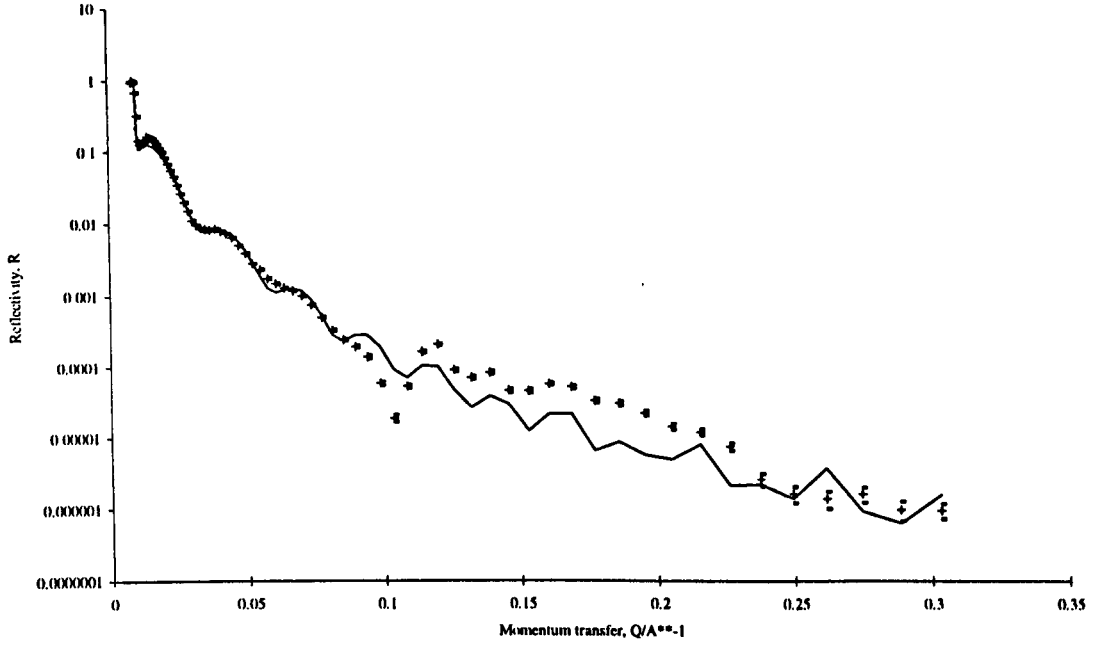

Figure 8 Showing the high quality fit (solid lines) obtained using the symmetrical gaussian model to fit the neutron data from S4 (points), within the limited Q-range over which the model is valid. χ^2=12.2. Errors are shown by the small dashes above and below each data point.

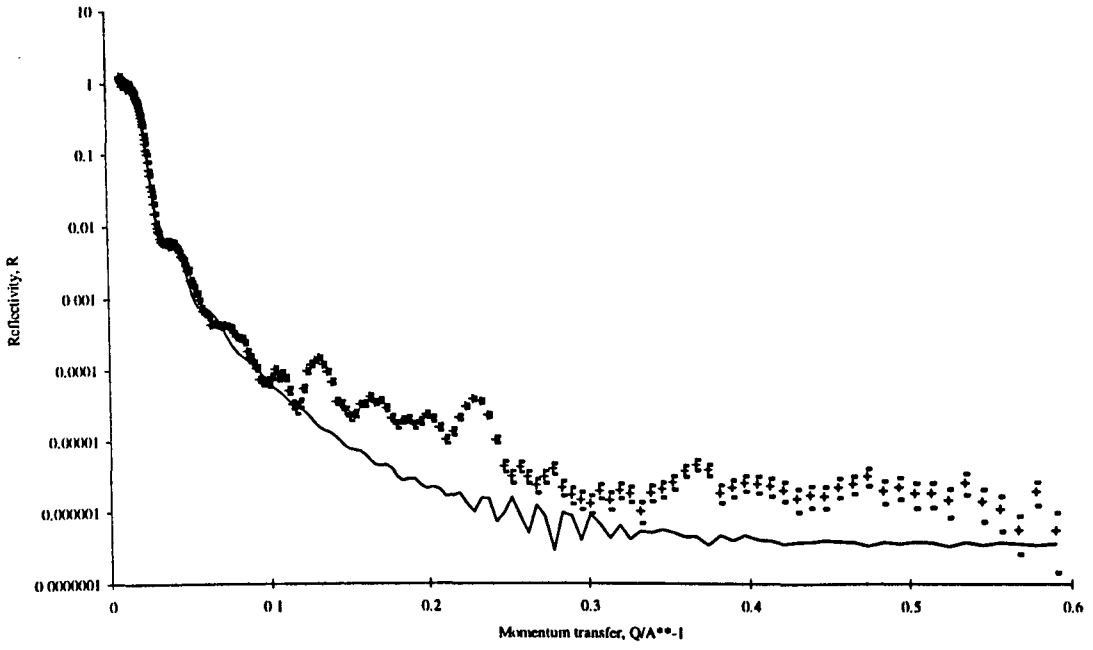

Figure 9 Showing the best fit obtainable (solid line) using the symmetrical gaussian model to fit the neutron data from S21 (points), within the limited Q-range over which the model is valid. Note how the fringe period is not matched and hence the fit cannot be regarded as a good one; χ^2 is not meaningful. Errors are shown by the small dashes above and below each data point.

Sample number	DTOT/ Angstroms	DSUB/ Angstroms	SIGMA/ Angstroms
S1	253 ± 15	136.0 ± 0.7	18.6 ± 0.4
S2	255 ± 3	271.0 ± 2.3	38 ± 3.0, 8.1
S3	256 ± 4	135.0 ± 0.9	18.4 ± 0.4
S4	441 ± 8	272.0 ± 18.5	37.3 ± 7.5, 8.1
S5	257 ± 5	n/a	
S6	444 ± 11	n/a	
S7	271 ± 6	n/a	
S8	n/a	n/a	
S9	n/a	n/a	
S10	266 ± 14	n/a	
S11	273 ± 14	n/a	
S12	264 ± 3	n/a	
S13	441 ± 8	265.0 ± 8.6	32.7 ± 3.2, 8.1
S14	259 ± 2	152.0 ± 0.5	18.3 ± 0.2
S15	455 ± 42	263.0 ± 6.6	33.4 ± 3.1, 8.1
S16	258 ± 5	153.0 ± 0.7	21.7 ± 0.2
S17	256 ± 3	150.0 ± 0.8	18.5 ± 0.1
S18	409 ± 120	149.0 ± 0.6	39.2 ± 1.9, 8.7
S19	271 ± 10	127.0 ± 0.5	20.7 ± 0.2
S20	304 ± 94	n/a	
S21	569 ± 882	260.0 ± 1.8	9.4 ± 1.4, 5.5
S22	250 ± 10	132.0 ± 14.2	9.69 ± 5.1
S23	273 ± 12	n/a	
S24	322 ± 78	381.0 ± 6.3	60.8 ± 2.9, 8.1
S25	244 ± 2	265.0 ± 6.6	30.3 ± 2.1, 8.1

cont.

Sample number	DTOT/ Angstroms	DSUB/ Angstroms	SIGMA/ Angstroms
S26	253 ± 3	277.0 ± 13.0	35.6 ± 4.3, 8.1
S27	253 ± 6	256.0 ± 0.7	27.3 ± 0.2, 8.1
S28	244 ± 5	263.0 ± 1.2	30.6 ± 0.5, 8.1
S29	n/a	227.0 ± 1.0	32.4 ± 0.7, 8.1
S30	266 ± 4	248.0 ± 1.3	32.1 ± 0.5, 8.1
S31	312 ± 9	141.0 ± 0.4	25.0 ± 1.3, 8.1
S32	298 ± 6	131.0 ± 0.4	18.5 ± 0.06
S33	407 ± 209	n/a	
S34	258 ± 2	n/a	
S35	246 ± 2	n/a	
S36	256 ± 3	n/a	
S37	253 ± 5	n/a	
S38	243 ± 10	n/a	
S39	247 ± 10	n/a	

Table 2. DTOT values from fits to the X-ray data and DSUB and SIGMA values from fits to the neutron data. Where two values are given in the SIGMA column, the two-sided gaussian model was used; otherwise the symmetrical gaussian model was used. Where no error is quoted in SIGMA, the value was fixed during the fit.

Sample number	X-ray NBHF/ x 10^{-5} Å^{-2}.	Coverage determined by X-rays/%	Neutron B_A/ x 10^{-3} Å^{-1}.	Coverage determined by neutrons/%.
S1	0.893 ± 0.391	79 ± 35	0.339 ± 0.002	75.7 ± 0.4
S2	0.865 ± 0.049	76 ± 4	0.353 ± 0.002	78.8 ± 0.4
S3	1.07 ± 0.394	95 ± 35	0.331 ± 0.002	73.9 ± 0.4
S4	0.915 ± 0.122	81 ± 11	0.372 ± 0.007	83.0 ± 2
S5	1.17 ± 0.200	103 ± 18	n/a	
S6	1.21 ± 0.322	107 ± 28	n/a	
S7	1.70 ± 0.084	150 ± 7	n/a	
S8	n/a		n/a	
S9	n/a		n/a	
S10	1.30 ± 0.471	103 ± 37	n/a	
S11	1.71 ± 0.133	136 ± 11	n/a	
S12	0.830 ± 0.037	73 ± 3	n/a	
S13	1.22 ± 0.127	108 ± 11	0.453 ± 0.006	101.1 ± 1.0
S14	1.08 ± 0.050	96 ± 4	0.358 ± 0.001	79.9 ± 0.2
S15	1.23 ± 0.590	109 ± 52	0.407 ± 0.004	90.8 ± 0.9
S16	1.14 ± 0.184	101 ± 16	0.442 ± 0.002	98.7 ± 0.4
S17	1.01 ± 0.064	89 ± 6	0.417 ± 0.002	93.1 ± 0.4
S18	1.65 ± 0.062	169 ± 6	0.254 ± 0.002	127.6 ± 1.0
S19	1.32 ± 0.965	135 ± 99	0.275 ± 0.001	138.2 ± 0.5
S20	2.17 ± 0.195	223 ± 20		
S21	1.69 ± 0.159	155 ± 15	-0.079 ± 0.003	39.7 ± 1.5
S22	1.33 ± 0.251	122 ± 23	-0.459 ± 0.001	230.6 ± 0.5
S23	2.02 ± 0.174	185 ± 16		
S24	1.35 ± 0.099	119 ± 9		

...cont.

Sample number	X-ray NBHF/ x 10^{-5} Å^{-2}.	Coverage determined by X-rays/%	Neutron B_A/ x 10^{-3} Å^{-1}.	Coverage determined by neutrons/%.
S25	1.14 ± 0.067	101 ± 6	0.407 ± 0.003	90.8 ± 0.7
S26	0.885 ± 0.040	78 ± 3	0.340 ± 0.004	75.9 ± 0.9
S27	1.20 ± 0.279	106 ± 25	0.368 ± 0.001	82.1 ± 0.2
S28	1.16 ± 0.230	103 ± 20	0.370 ± 0.001	82.6 ± 0.2
S29	n/a		0.190 ± 0.002	42.4 ± 0.4
S30	1.10 ± 0.048	97 ± 4	0.295 ± 0.003	65.8 ± 0.7
S31	1.06 ± 0.046	109 ± 5	0.302 ± 0.002	151.8 ± 1.0
S32	1.27 ± 0.074	130 ± 8	0.323 ± 0.001	162.3 ± 0.5
S33	1.58 ± 0.173	162 ± 18	n/a	
S34	0.699 ± 0.031	62 ± 3	n/a	
S35	0.567 ± 0.017	50 ± 1	n/a	
S36	0.622 ± 0.030	55 ± 3	n/a	
S37	0.763 ± 0.045	67 ± 4	n/a	
S38	1.38 ± 0.554	122 ± 49	n/a	
S39	1.99 ± 0.168	213 ± 18	n/a	

Table 3. Values for NBHF and B_A and the film densities they represent. The values for NBHF were obtained from the X-ray data and for B_A from the neutron data.

It will be noticed that several samples do not have their values filled in in the tables. This is because a physically reasonable fit could not be obtained for these samples and this is most likely to be due to poor film quality, which gives rise to incomplete coverage, excessive interlayer roughness and, in the case of the neutron data, a resultant lack of detectable contrast in the SLD profile.

In order to illustrate the reproducibility of samples, X-ray data from 3 samples (S2, S14 and S17) are shown in Figure 10.

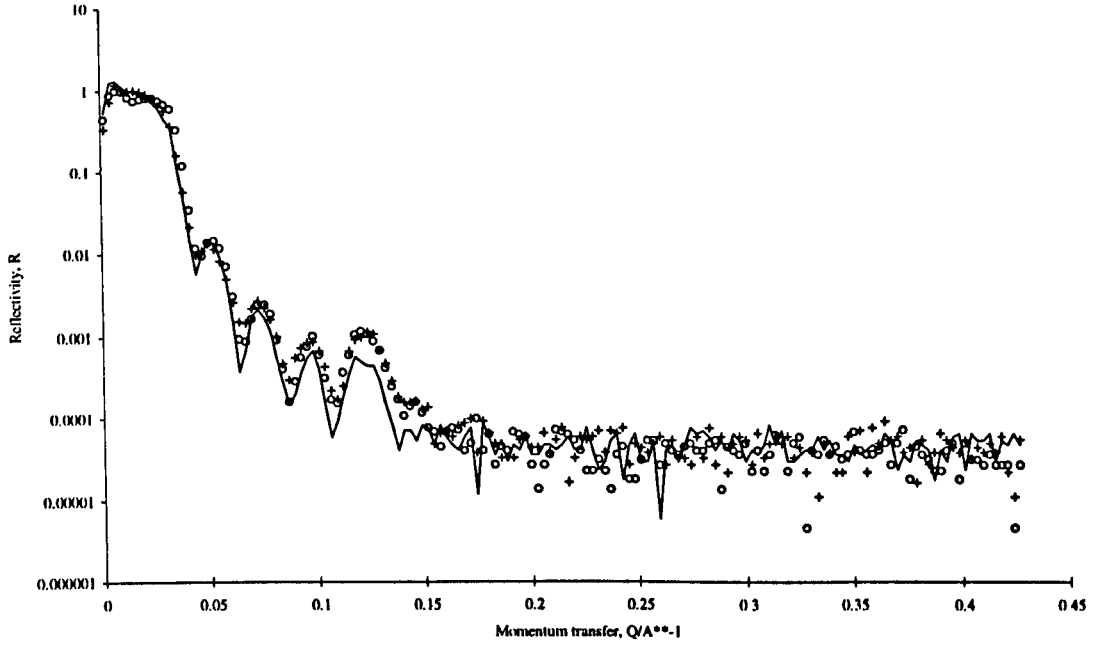

Figure 10 Showing the reproducibility of S2 (++++), S14 (——) and S17 (oooo). X-ray data.

A selection of neutron reflectivity profiles are shown in Figures 11 - 15. These show the sensitivity of the technique to the effects of different dipping speeds (Figure 11), different dipping pressures (Figure 12), the presence of cadmium ions (Figure 13), time under water (Figure 14) and the position of the D-labelled layer (Figure 15). Figure 5 has already illustrated the limitations of the gaussian model when data above $Q = 0.1 Å^{-1}$ are included in the fit, showing clearly how the calculated reflectivity is damped.

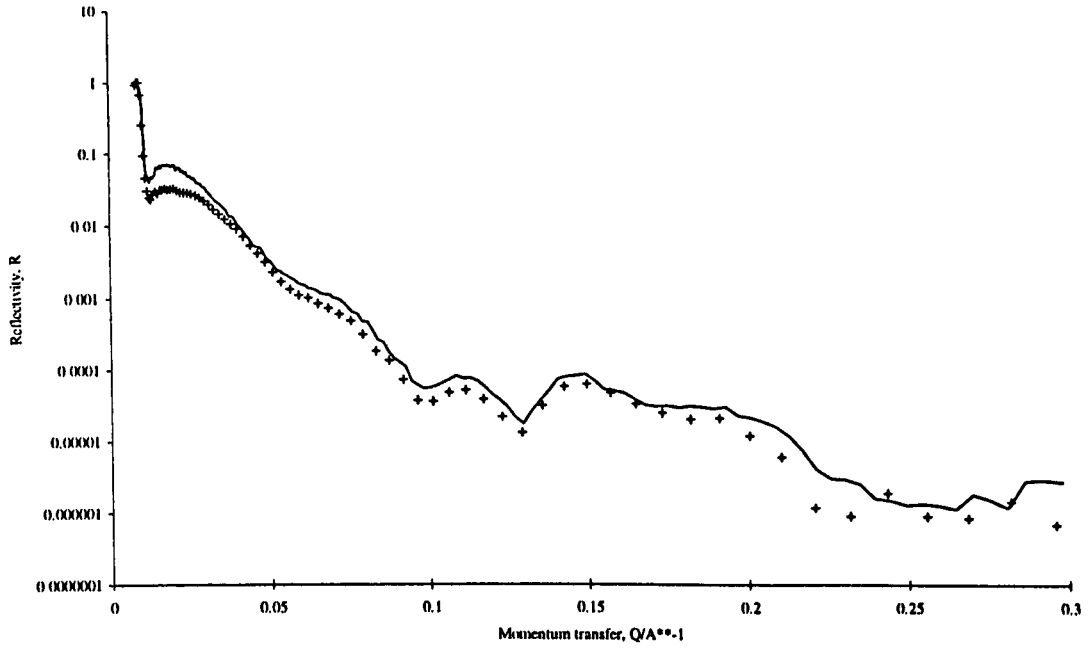

Figure 11 Neutron data from S1 (+++) and S16 (—), showing the effect of dipping speed. S1 was dipped at 40mNm^{-1} and 15 mm/min; S16 was dipped at 40mNm^{-1} and 5 mm/min. Both sample structures HHDHH (nomenclature as in Table 1).

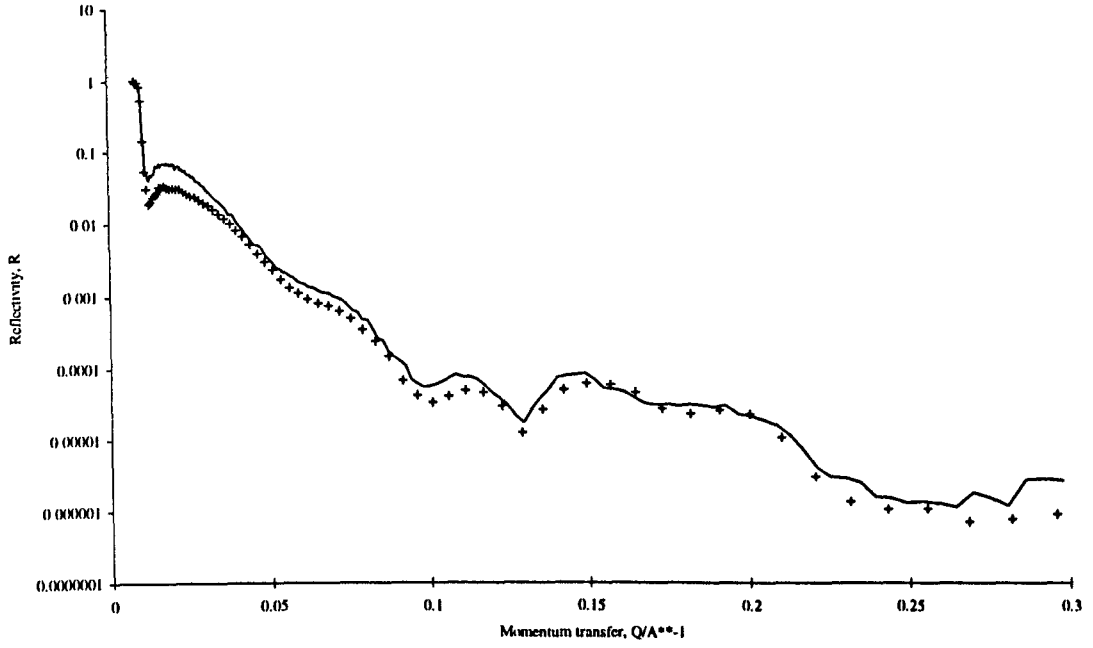

Figure 12 Neutron data for S3 (+++) and S16 (—), showing the effect of dipping pressure. S3 was dipped at $30mNm^{-1}$ and 5 mm/min. S16 was dipped at $40mNm^{-1}$ and 5 mm/min. Both sample structures HHDHH (nomenclature as in Table 1).

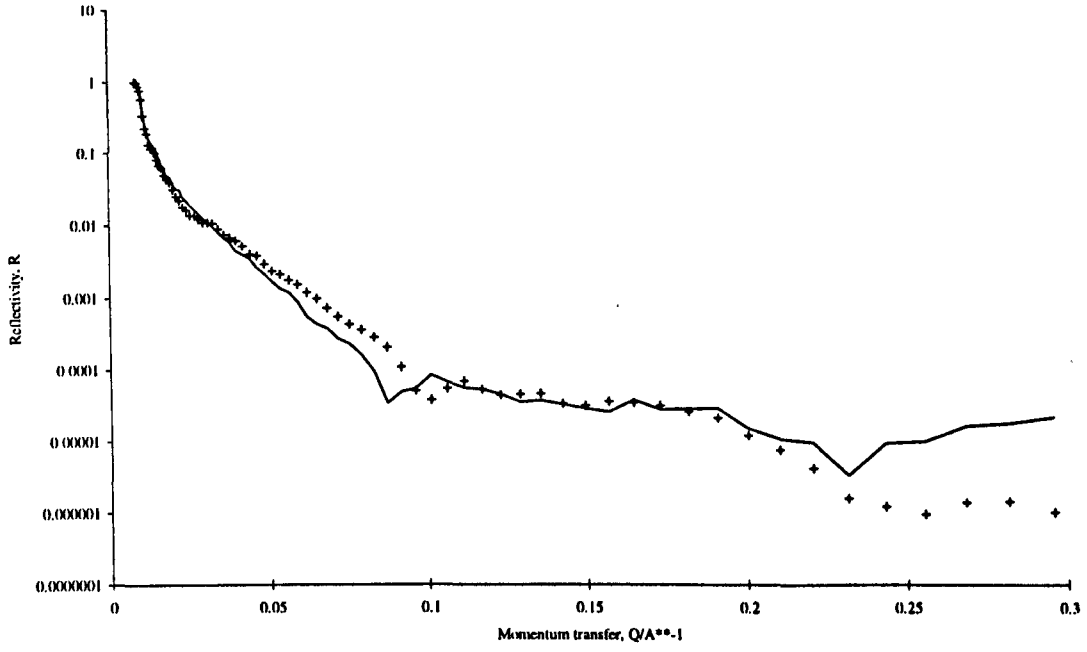

Figure 13 Neutron data from S7 (++++) and S11 (——), showing the effect of cadmium ions on the film thickness and hence on the Kiessig fringes. Both S7 and S11 were dipped at 40mNm^{-1} and 15 mm/min. Both sample structures **DHHHH** (nomenclature as in Table 1).

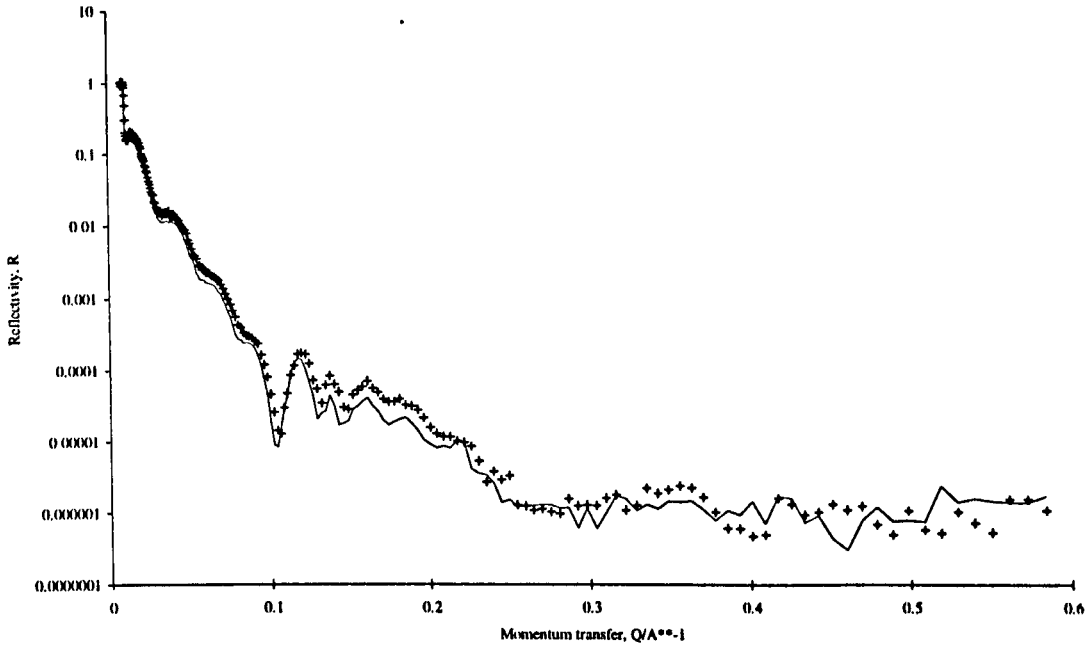

Figure 14 Neutron data from S13 (+++) and S15 (—), showing the negligible effect of time underwater on intensity or fringe spacing. Both S13 and S15 were dipped at 35mNm^{-1} and 15 mm/min; S15 was left under water for 10 minutes between dipping the two deuterated monolayers. Both sample structures HHHHDHHHH (nomenclature as in Table 1).

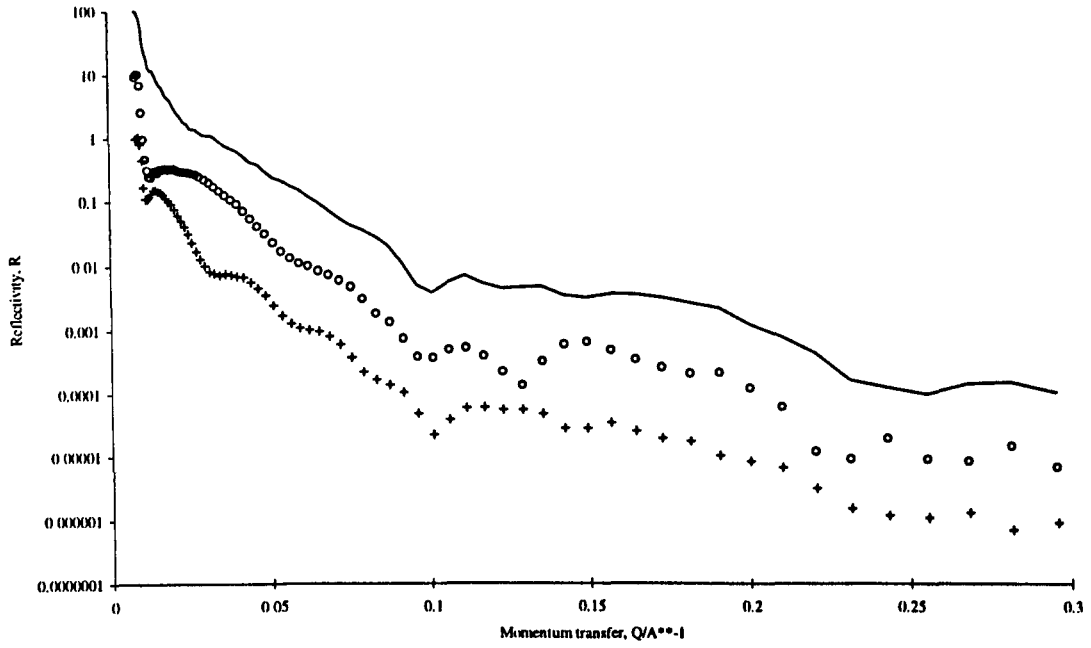

Figure 15 Neutron data from S2 (+++), S1 (oooo) and S7 (—), showing the effect of the position of the D-layer on the fringe period. All were dipped at 40mNm^{-1} and 15 mm/min. The data have been shifted for clarity, S1 by a factor of 10, S7 by a factor of 100. Sample structures: S1 HHDHH, S2 HHHHD, S7 DHHHH (nomenclature as in Table 1).

5.4.2 Surface Potential Measurements.

Section 4.4 outlined the basics of the experimental procedure required for surface potential (ψ) measurement. Further details of the experiment performed are given here.

A very simple experiment was carried out, to investigate whether any extra information about monolayer states could be gleaned from a study of ψ at various values of π. A monolayer of docosanoic acid was spread on pure water, pH3, 20°C. It was compressed to 25mN/m and left there for approximately 35 minutes, with the Control setting keeping π constant, and ψ was monitored throughout on the x-y-t plotter. The monolayer was then compressed to 30mN/m and again ψ was recorded for 35 minutes. Finally, it was compressed to 40mN/m and ψ was again recorded for 35 minutes. The layer was very stable in π for each of these measurements, but distinct differences may be observed in the ψ-traces. Due to the nature of the data record, a photocopy of the plotter traces is the clearest way of presenting the results, and this is shown in Figure 16.

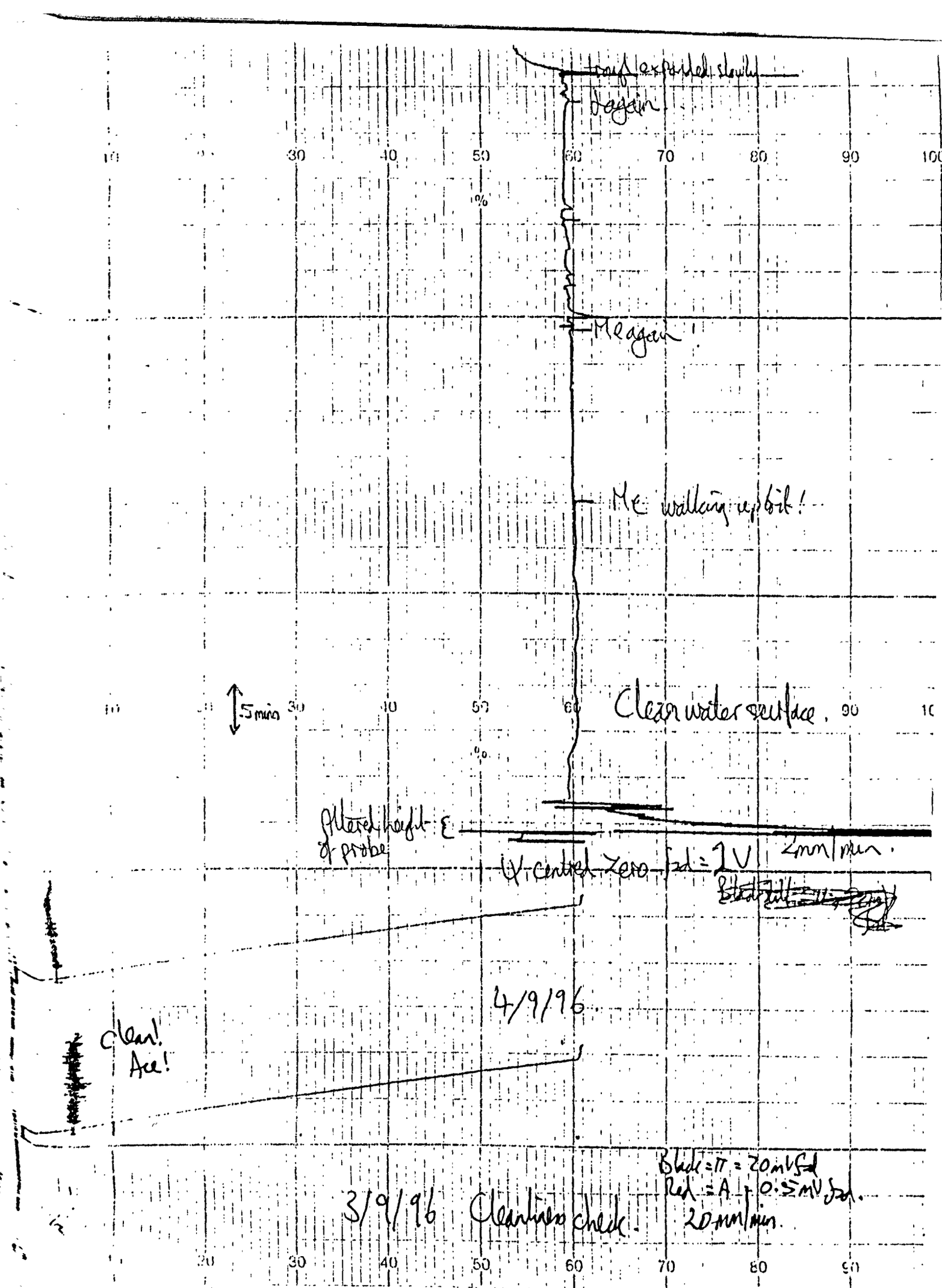

Figure 16 a) surface potential data for the clean water surface.

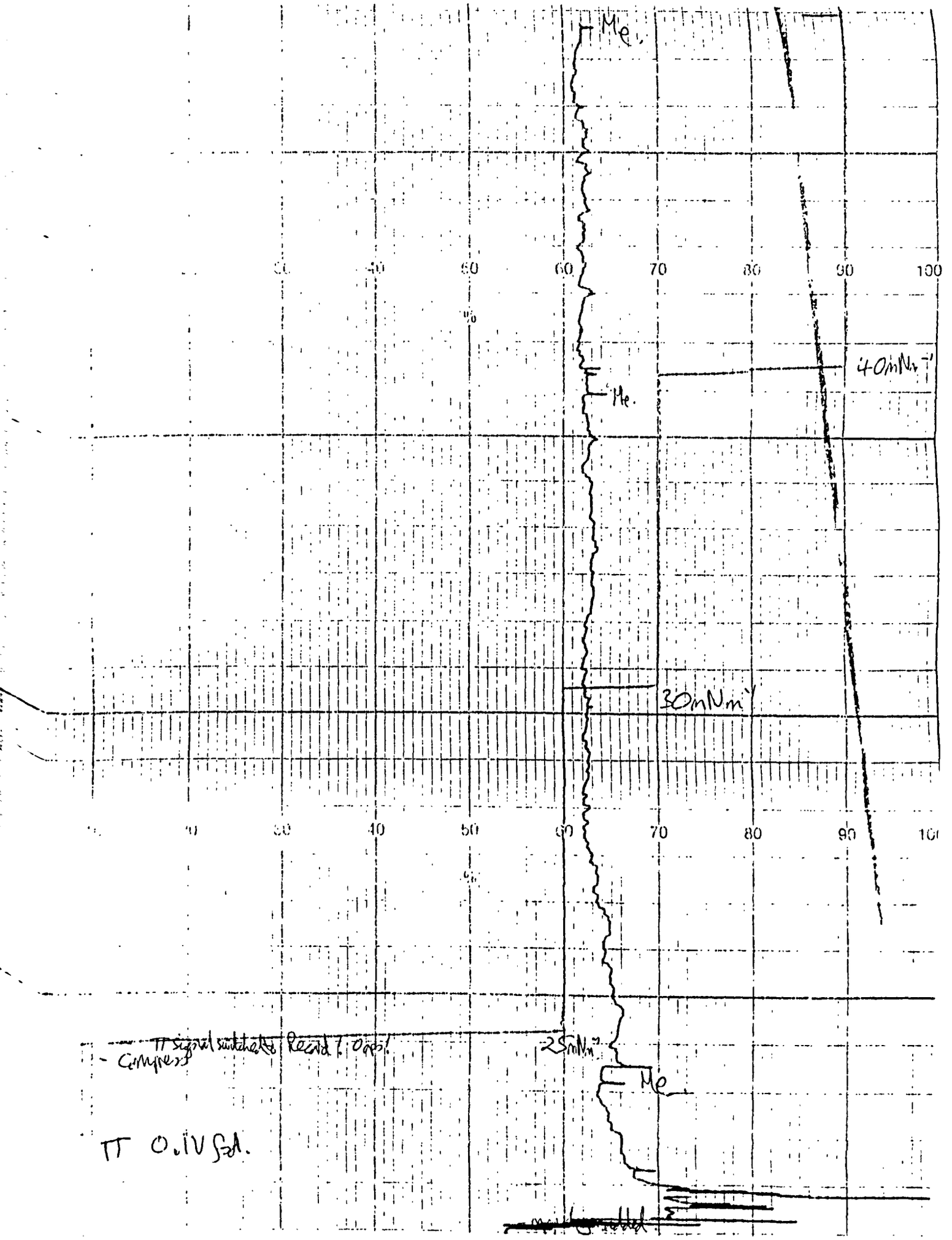

Figure 16 b) surface potential data for the monolayer at the various surface pressures discussed in the text.

It will be seen that the signal from the clean water surface is very steady (Figure 16a), at +200mV. Once the monolayer has stabilised at 25mN/m (Figure 16b), the ψ signal has an average value of +250mV, with fluctuations of the order of $\pm$10mV, and the time scale of these fluctuations is of the order of 30 - 60s. At 30mN/m, ψ is much steadier, at +260 $\pm$ 5mV, with a time scale for the fluctuations of approximately 5 minutes. At 40mN/m, ψ has an average value of +240 $\pm$ 20mV, with a time scale for the fluctuations of 1 minute.

These observations are readily understood in terms of the monolayer phases discussed in Chapter 2 [4]. At 25mN/m, the monolayer is in the L_2' phase, where the chains are at an angle of 15° and the monolayer is fluid, displaying Newtonian behaviour [5a-c]; it is rapidly mobile, on a scale visible to the surface potential technique, which is in the 5mm size range. At 30mN/m, the monolayer is just into the S phase: the chains are upright and the film close-packed; its mobility is noticeably less in size terms, and slower in time. At 40mN/m, the monolayer is well into the S^{-}phase and displays non-Newtonian flow characteristics (Chapter 2, Section 2.2.3, [5a-c]); it is rigid and appears to be susceptible to all vibrations, mirroring them with large and rapid fluctuations. Thus previous work [4; 5a-c] is confirmed, lending support to these surface potential data. Therefore, this simple and non-invasive technique provides a qualitative picture of the monolayer at these three surface pressures, and this picture is consistent with the observations and conclusions of previous workers.

5.5 Discussion and Conclusions.

5.5.1 Film Thickness.

The values for DTOT from the X-ray fitting were used to calculate layer thickness (DMON) values for each all-acid sample, for comparison with the literature value. Given that X-rays will not be sensitive to the outermost hydrocarbon layer, due to the low electron density contrast with air, the DTOT values were taken to represent 9 monolayers, plus the headgroup region of the 10^{th}. From CPK space-filling molecular models, the headgroup region is measured to be 3.1Å. Ten headgroups will therefore account for 31Å of DTOT, with the remainder representing 9 hydrocarbon chain regions. The DTOT values from the all-H and all-D samples (S34 - S38) are very close within their errors and yield a mean DTOT of 250.5Å. This gives a value of 24.5Å for each chain, and hence 27.6Å for each acid molecule, on average. The error in this value for the length is 0.4Å. Since the length of docosanoic acid is 30Å [3], this implies the molecules are tilted by 23 ± 2° from the surface normal. This is intermediate between the L_2 and L_2' phase tilts of 30° and 15°, respectively (see Chapter 2, section 2.2.2), and it is clear that the film packing has relaxed from the S phase in the Langmuir film as a consequence of the dipping process.

This value of 27.6Å for DMON agrees very well with the values from the other samples, as can be seen from Table 2, implying a good degree of reproducibility between samples prepared under similar dipping conditions, and no appreciable differences in the packing of those films which were prepared under different dipping conditions. This is to be expected, given the samples were all dipped at pH3, where all the headgroups are fully protonated and where the isotherm shows no phase change over the π-range used. The exceptions are S29 and S30, which were dipped at 15mN/m. S29 could not be fitted, and given the sample was dipped at π = 15mNm^{-1}, the phase change on dipping will have been from the L_2' phase. What this packing would have changed to on the substrate is

not clear, although one probable conclusion is that the monolayer has become disordered or has collapsed, and this would explain the inability to fit this particular sample.

S30 yielded anomalous values for DTOT and hence for DMON, and given this sample was also dipped at π = 15 mNm^{-1}, although at a much slower speed (5 mm/min vs 15 mm/min for S29) an element of disorder is again probable. It is interesting that the slower dipping speed used for S30 has apparently yielded a slightly more ordered film at this very low π. Unfortunately, time did not allow for this observation to be addressed in more depth; this could be a fruitful experiment in the future.

These two results lend support to the conclusion that the monolayer changes phase on dipping. No firm conclusion can be inferred from the results from S24. This sample was dipped at 30°C and 40 mNm^{-1}. Even at this π, the monolayer was not stable, making dipping difficult and the data unreliable. At this temperature the monolayer will have gone straight from L_2 to S [4] with no L_2' phase (see Fig. 17), and the effect this would have on the dipping behaviour is an unknown. Clearly, an apparent film thickness of 322 ± 78 Å is a meaningless result for a film nominally 276 ± 7 Å thick, and some other mechanism, most likely severe disorder, must be involved.

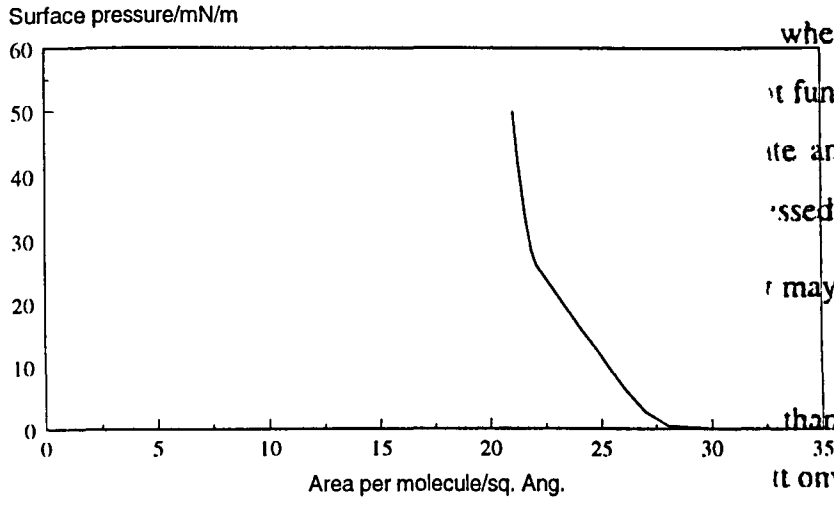

Figure 17 The isotherm of docosanoic acid on pure water, pH3, 30°C.

S14 and S15 both yield values of DMON (28.4Å and 26.6 Å respectively) which, within errors, show no appreciable deviation from the other samples, despite these two having been left under water for 10 minutes between the down- and up-strokes of the D-layer deposition. Thus, swelling of the films due to trapped water may be ruled out, as confirmed by [6]. This is a surprising result in the light of the conclusions of previous workers discussed in Chapter 2, Sections 2.3.2 and 2.4.1, but it is a very encouraging observation for the present thesis.

Using the figure of 27.6Å for the length of the acid in the film, the thicker samples (S4, S6, S13 and S15) would have an actual thickness of approximately 471Å, and therefore an expected X-ray DTOT of 446Å. They are found to have actual X-ray DTOT values of 441, 444, 441 and 455Å, respectively, giving a mean of 445 ± 17Å, which is a very close agreement between theory and practice. This suggests that the phase change on dipping and the subsequent packing remain constant over several layers, which in turn suggests that the structure of the LB film is determined at the point of dipping, rather than by any later treatment of the film, such as time under water. It would be interesting to study still thicker films in order to confirm this.

To calculate DMON for the polysiloxane shown in Figure 1, for comparison with the value obtained in [1], the X-ray value for DTOT from S39 (the all-polymer sample) was taken to be the true thickness of the dipped film, yielding a value for the polysiloxane of 24.7Å, which compares favourably with the value from a Langmuir film of the molecule in [1] of 17 - 28Å over a π-range which includes the dipping pressure used here (11mN/m). This approach was taken due to the fact that the electron density of the pendant chain regions of this molecule is much higher than that of a hydrocarbon chain (X-ray SLD 1.69×10^{-5}Å^{-2}, compared with 0.85×10^{-5}Å^{-2} for a hydrocarbon chain) and so the outermost layer is detected by the X-rays.

5.5.2 Film Density.

The expected values for X-ray NBHF and neutron B_A were calculated from molecular structure and volume, using isotherm values for the area per molecule and the DMON values calculated in the previous section. NBHF values for mixed films, i.e. those incorporating P or D molecules, were calculated as a weighted average. These were then used as one of the starting parameters in the fitting of each data set, and allowed to float to give a measure of film density, i.e. of coverage of the substrate, and these are tabulated in Table 3. Table 4 shows the relative amount picked up on each dip and the total coverage, both in cm^2, and the mean % coverage overall, for qualitative comparison with the X-ray and neutron data. It must be stressed that these deposition ratio data can only be used to compare sample with sample, or molecule type with molecule type. They can in no way be said to represent actual coverage, due to the fact that deposition on the rear (i.e. the ground and therefore macroscopically uneven) face of the Si wafers is uncertain, and was not measured in this work. Therefore, quantitative comparison with NBHF and B_A is not meaningful. The data are presented here simply for ease of qualitative comparisons, which is perfectly valid since the Si wafers used all had the same morphology. The reason why wafers polished on both sides were not used was simply one of cost: single sided wafers cost only £5 each, whereas wafers polished on both sides cost around £100 each. Unfortunately, insufficient funds were available to this project to purchase one of the latter in order to investigate an absolute value for the deposition ratio. It is to be hoped that this issue can be addressed by a future project.

Despite the caveat above, there are some general trends that may be observed in Table 4, as follows:

a) deposition on the first downstroke is generally poorer than on subsequent dips, in line with observations from other workers, from Blodgett onwards.

b) deposition is generally higher on the upstroke than on the downstroke This is extremely supportive evidence in favour of the various literature theories, discussed

in Chapter 2, on why scrambling occurs, suggesting as it does that, whilst individual layers might be incomplete, holes in one layer are filled in by the subsequent layer.

c) the mean % coverage is frequently less than 100%, sometimes as much as 50% less, but it does not greatly exceed 100%: the largest value observed here was 113%. This is a very wide range of values, and even given the inherently qualitative nature of the data, it suggests a wide range of film qualities should be expected.

d) the effect of increased temperature has had a very large effect on the dipping behaviour of the monolayer in S24 (30°C).

e) on the whole, the polysiloxane does not deposit as effectively as the fatty acid, presumably due to the differences in head-to-head interactions. It dips better on the upstroke than on the downstroke, although the precise reason for this is not clear.

There are nine samples with errors in NBHF that are unreasonably large (>20%), indicating that more parameters need to be floated to allow a fit to these samples with any degree of confidence, or that a more sophisticated model than the Volume Fraction one needs to be used. Alternatively, excessive disorder has resulted in extremely uneven films. These nine samples are S1, S3, S6, S10, S15, S19, S22, S27 and S38, and they will be discussed in Section 5.5.4.

Of the remaining 30, all but seven show very good agreement between the neutron and X-ray results. This is a very encouraging result in terms of further highlighting the complementarity of the two techniques, and it justifies a high degree of confidence in using data from one as starting points for the other. The discrepancies are most likely to arise from interfacial roughnesses, especially at the air-film interface where the electron density contrast is greatly reduced for a rough surface, thus increasing the error in the X-ray fits. As already mentioned, this should be a solvable problem given greater use of more flexible models, for all but the roughest films.

Sample	1↓ cm^2	2↑ cm^2	3↓ cm^2	4↑ cm^2	5↓ cm^2	6↑ cm^2	7↓ cm^2	8↑ cm^2	9↓ cm^2	10↑ cm^2	Total cm^2	Mean Coverage %
S1	44.6	100.4	92.1	96.2	**86.5**	**72.5**	85.1	106.0	76.7	73.9	834	108
S2	55.8	68.4	113.0	68.4	108.8	68.4	97.7	92.1	**108.8**	**76.7**	858	111
S3	54.4	72.5	97.7	92.1	**104.6**	**76.7**	92.1	76.7	78.1	75.3	820	106
S4	61.4	64.2	104.6	89.3	75.3	65.6	76.7	73.9	**73.9**	**76.7**	762	98
S5	61.4	108.8	78.1	75.3	**108.8**	**72.5**	92.1	100.4	71.1	67	836	108
S6	60	80.9	80.9	103.2	78.1	75.3	75.3	79.5	**85.1**	**72.5**		
	11↓ cm^2	12↑ cm^2	13↓ cm^2	14↑ cm^2	15↓ cm^2	16↑ cm^2	17↓ cm^2	18↑ cm^2				
	103.2	78.1	89.3	100.4	80.9	72.5	96.3	83.7			1495	107
S7	**90.7**	**76.7**	87.9	113	72.5	72.5	99.0	80.9	32.3	100.4	876	113
S10	53.0	65.6	101.8	62.8	67.0	62.8	76.7	83.7	**68.4**	**62.8**	705	91
S11	**61.4**	**53.0**	79.5	51.6	76.7	54.4	79.5	61.4	72.5	58.6	649	84

cont.

Sample	1↓ cm^2	2↑ cm^2	3↓ cm^2	4↑ cm^2	5↓ cm^2	6↑ cm^2	7↓ cm^2	8↑ cm^2	9↓ cm^2	10↑ cm^2	Total cm^2	Mean Coverage %
S12	78.1	82.3	78.1	90.7	**99.0**	**92.1**	76.7	78.1	75.3	79.5	830	107
S13	82.3	83.7	76.7	79.5	71.1	75.3	71.1	76.7	**75.3**	**78.1**		
	11↓	12↑	13↓	14↑	15↓	16↑	17↓	18↑				
	76.7	79.5	76.7	79.5	75.3	78.1	76.7	76.7			1393	100
S14	76.7	86.5	80.9	80.9	**73.9**	**78.1**	73.9	79.5	72.5	75.3	778	101
S15	69.8	78.1	72.5	78.1	67.0	69.8	69.8	75.3	**73.9**	**76.7**		
	11↓	12↑	13↓	14↑	15↓	16↑	17↓	18↑				
	75.3	82.3	72.5	78.1	72.5	75.3	75.3	78.1			1340	96
S16	72.5	80.9	76.7	78.1	**85.1**	**85.1**	64.2	65.6	72.5	72.5	753	97
S17	73.9	80.9	72.5	80.9	**75.3**	**82.3**	72.5	82.3	73.9	79.5	774	100
S18	51.6	68.4	43.2	62.8	46	57.2	48.8	40.5	**82.3**	**82.3**	583	75

Cont.

Sample	1↓ cm^2	2↑ cm^2	3↓ cm^2	4↑ cm^2	5↓ cm^2	6↑ cm^2	7↓ cm^2	8↑ cm^2	9↓ cm^2	10↑ cm^2	Total cm^2	Mean Coverage %
S19	53	68.4	41.9	64.2	**80.9**	**83.7**	43.2	68.4	57.2	68.4	629	81
S20	**72.5**	**72.5**	30.7	39.1	61.4	76.7	54.4	73.9	48.8	61.4	591	76
S21	**76.7**	**85.1**	**103.2**	**86.5**	**78.1**	**75.3**	**71.1**	**75.3**	55.8	72.5	780	101
S22	**75.7**	**83.7**	**96.3**	**80.9**	46.0	64.2	**72.5**	**75.3**	**72.5**	**72.5**	741	96
S23	57.2	72.5	**76.7**	**80.9**	**101.8**	**80.9**	**69.8**	**72.5**	**72.5**	**72.5**	757	98
S24	83.7	27.9	33.5	29.3	19.5	25.1	27.9	33.5	**55.8**	**55.8**	392	51
S25	75.3	80.9	72.5	78.1	71.1	79.5	69.8	78.1	**78.1**	**87.9**	771	100
S26	71.1	83.7	71.1	76.7	69.8	76.7	69.8	76.7	**75.3**	**83.7**	755	98
S27	72.5	83.7	76.7	79.5	72.5	78.1	72.5	78.1	**76.7**	**83.7**	774	100
S28	72.5	85.1	73.9	80.9	72.5	80.9	72.5	78.1	**75.3**	**80.9**	773	100
S29	68.4	86.5	72.5	33.5	71.1	27.9	72.5	39.1	**73.9**	**55.8**	601	78
S30	67.0	75.3	68.4	73.9	68.4	41.9	68.4	53	**71.1**	**61.4**	649	84

Cont.

Sample	1↓ cm^2	2↑ cm^2	3↓ cm^2	4↑ cm^2	5↓ cm^2	6↑ cm^2	7↓ cm^2	8↑ cm^2	9↓ cm^2	10↑ cm^2	Total cm^2	Mean Coverage %
S31	33.5	27.9	30.7	36.3	32.1	33.5	32.1	30.7	**78.1**	**86.5**	421	54
S32	26.5	27.9	25.1	29.3	**75.3**	**86.5**	54.4	39.1	53.0	43.2	460	59
S33	**76.7**	**87.9**	54.4	71.1	53.0	68.4	51.6	67.0	55.8	67.0	653	84
S34	86.5	92.1	80.9	86.5	80.9	90.7	82.3	89.3	80.9	87.9	858	111
S35	**73.9**	**85.1**	**76.7**	**87.9**	**72.5**	**75.3**	**72.5**	**76.7**	**73.9**	**79.5**	774	100
S36	**83.7**	**92.1**	**80.9**	**100.4**	**82.3**	**89.3**	**82.3**	**85.1**	**80.9**	**86.5**	864	112
S37	**86.5**	**87.9**	**80.9**	**93.5**	**78.1**	**82.3**	**78.1**	**83.7**	**78.1**	**82.3**	831	107
S38	**80.9**	**94.9**	**82.3**	**89.3**	**78.1**	**85.1**	**79.5**	**86.5**	**79.5**	**86.5**	843	109
S39 (all P)	39.1	43.2	26.5	46.0	36.3	51.6	36.3	50.2	40.5	48.8	419	54

Table 4. Relative coverage for each layer of each sample (cm^2), the total relative coverage (cm^2) and the mean relative coverage (%). As in Table 1, bold type indicates a deuterated layer.

5.5.3 DSUB and σ.

If no mixing has occurred between layers, DSUB is expected to be in the centre of the D-layer, and σ to be in agreement with the thickness of a bilayer. Hence, for a 10-layer film of docosanoic acid, DSUB is expected to be 138Å, i.e. 5 x 27.6Å, and σ to be 15.9Å, i.e. (27.6 x 2)/√12. (from Eq. 5.2)

Deviations from these values would indicate that the centre of gravity of the gaussian, i.e. DSUB, has been shifted within the LB film due to scrambling, most likely due to D-molecules filling up holes in the H-layer immediately below [7]. The next D-layer may well fill in holes in the first, so that the centre of gravity of the gaussian is not at the geometrical centre of the D-bilayer. This does, therefore, mean that the symmetrical gaussian model is only an approximation to the structure, and further work on the block model with two half-gaussians will be needed to clarify the picture further.

If DSUB is significantly lower in the structure than expected, then the integrity of the dipped layers below the D-layer must be questioned, since the most logical explanation for such a value of DSUB is that the D-molecules are distributed thoroughly through the film via holes in each layer, some of which must be large enough to overlap layer-to-layer. If σ remains low, the D-layer has remained in a region approximately a bilayer in width. However, if σ becomes large the D-layer is distributed through a much wider region and the scrambling is more extreme. This is illustrated clearly by S24: DSUB is at the air-film interface, as expected from the film structure, but σ is 60.8Å, representing a breadth of 211Å for the extent of the D-layer, which implies significant penetration into the film. This may be contrasted with S25, where again DSUB is at the air-film interface but σ is only 30.3Å, representing a depth of 105Å, i.e. approximately four layers, for penetration of the D-layer.

Referring to Table 2, it will be seen that most values of DSUB are very close to the expected positions, whilst most σ are slightly larger than expected. For instance for S1, DSUB is 136Å, compared with the expected 138Å, whereas σ is 18.6Å, representing a distribution of the D-layer 64.4Å thick, compared with the expected value of 55Å,

suggesting that the deuterated material has spread slightly beyond the dipped bilayer. This is readily explained by the first D-layer being diluted into the preceding H-layer, while the second D-layer fills in any holes in the first, resulting in a defect-free D-layer. The second D-layer will in turn be diluted by H-molecules from the subsequent layer. The broader-than-expected σ simply reflects this mixing into the preceding H-layer. As has been mentioned above, a symmetrical gaussian is not a strictly accurate representation of this, and more work on the block model with two unsymmetrical half-gaussians is needed.

Having described the interpretation of DSUB and σ, the discussion will now consider how they are affected by different dipping conditions, if at all.

5.5.3.1 Dipping Pressure.

Consider samples S2, S13, S17, S25, S27, and S29, covering π from 15mN/m to 40mN/m but keeping the dipping speed constant at 15mm/min. S17 has been included as the only sample dipped at 30mN/m at this speed, although its structure does not match the others directly. For ease of reference the relevant figures are given again in Table 5 below. S24 has been omitted from this particular part of the discussion because of the temperature difference in the dipping conditions; it will be covered in Section 5.5.3.3.

Sample number and dipping pressure, mN/m.	DTOT / Angstroms.	DSUB / Angstroms. Actual & Expected		SIGMA / Angstroms. Actual & Expected	
S2, 40	255 ± 3	271.0 ± 2.3	248	38 ± 3.0, 8.1	8, 8
S13, 35	441 ± 8	265.0 ± 8.6	248	32.7 ± 3.2, 8.1	8, 8
S17, 30	256 ± 3	150.0 ± 0.8	138	18.5 ± 0.1	16
S25, 25	244 ± 2	265.0 ± 6.6	248	30.3 ± 2.1, 8.1	8, 8
S27, 20	253 ± 6	256.0 ± 0.7	248	27.3 ± 0.2, 8.1	8, 8
S29, 15	n/a	227.0 ± 1.0	248	32.4 ± 0.7, 8.1	8, 8

Table 5 Comparing data at different dipping pressures.

In order to equate the σ values in the two models, it must be remembered that where the two-sided gaussian has been used the effective width of the D-labelled layer will be $\frac{(\sigma_1+\sigma_2)\sqrt{12}}{2}$. Thus the effective penetration depth of the D-layer in S2 is 80Å, in S13 71Å, in S17 64Å, in S25 66Å, in S27 61Å and in S29 70Å. The expected thickness of the D-layer is that of a bilayer in all six cases, i.e. 55 Å. Thus it is clear that different dipping pressures allow the penetration depth into the film to vary within a range of 19Å, which is 69% of the width of a monolayer. This significant variation is most likely due to different defect densities within the Langmuir films at the different surface pressures,

thus presenting different numbers or sizes of holes for the subsequent dipped layer to fill. This is consistent with the theory on monolayer phases discussed in Chapter 2, and also with the experiment done in the course of the present work, on surface potential measurement. This will be discussed in Section 5.5.4.

It will be noted, however, that even within errors, DSUB is approximately one monolayer thickness higher than expected, for all samples except S17 and S29. The central position of the D-layer in S17 is clearly modelled more closely by the gaussian model than is the D-layer at the air interface, except in the case of S29, where the very low dipping pressure has perhaps resulted in a more open film structure for the D molecules to penetrate, giving a D-layer as wide as in the other samples, but lower down in the film and hence easier for the gaussian profile to model. The fact that no DTOT value could be obtained for this sample lends support to this theory of an open film structure, as it suggests there was insufficient electron density contrast for the X-rays to be affected. However, see Section 5.5.3.2 for further comment on this matter. As to the remaining four samples, it must be inferred that the gaussian model used here is still not quite satisfactory for completely modelling a D-layer at the air interface, although the basic approach shows considerable promise.

Despite this limitation, much useful information has been extracted from the data, in terms of the distribution of the D-layer and hence the structure and integrity of the films at the various dipping pressures, and these results are consistent with the previous work discussed in Chapter 2.

5.5.3.2 Dipping Speed.

Consider S1 against S16, i.e. 40mN/m and 15 and 5 mm/min, and S3 against S17, i.e. 30mN/m and 5 and 15mm/min. All four samples have the structure HHDHH (nomenclature as in Table 1).

S1 has a DSUB of 136 Å and a σ of 18.6 Å.

S16 has a DSUB of 153 Å and a σ of 21.7 Å.

S3 has a DSUB of 135 Å and a σ of 18.4 Å.

S17 has a DSUB of 150 Å and a σ of 18.5 Å.

These figures show that, whilst σ is relatively unaffected by dipping π and speed, DSUB is profoundly affected, to the extent of 15 - 17 Å. Being much closer to the air/film interface implies greater order in the layers underneath, since the deuterated material will truly be in a bilayer, best represented by a block, and the gaussian model cannot reflect the consequent delta-functions in SLD very accurately. Indeed, this author was able to produce a model for S17, using a block model in an early version of Fitnew. This used an 11 layer model for the LB film, with a tail thickness of 25.6Å and a headgroup thickness of 1.89Å, both of which are rather smaller than the values from the X-ray data given in Section 5.5.3. However, the block model also required a sublayer of silicon dioxide, 11.9 Å thick, which the later gaussian models did not need. Thus the total film thickness is 277.4Å, which is very close to the value expected for a ten-monolayer sample. It is possible that the block model requires this "sublayer" in order to match overall thickness and mean SLD values to the data, highlighting a limitation of this rigid approach.

The fit obtained by the block model to S17 is shown in Figure 18a), while that obtained using the gaussian model is shown in Figure 18b). In confirmation of the acknowledged limitation of the gaussian approach beyond $Q = 0.1Å^{-1}$, it will be noted that Figure 18a) illustrates a model which has the potential to fit the data over the whole Q range, whereas Figure 18b) shows a more limited model. The overriding advantage of the

gaussian approach, though, is in its ability to model scrambled layers, which the block model cannot do. This is illustrated in Figure 19, which shows the block model fit to S1, assuming 24% mixing of the lower D-layer into the H-layer immediately below, other parameters being the same as for S17. The model in this figure is clearly not as close as those in Figures 5 and 8, which show the results from the gaussian model.

Figures 20 a) - d) illustrate further the similarities and differences that are apparent from the above considerations of DSUB and σ: S1 and S3 show very similar structures, and likewise S16 and S17 show very similar structures.

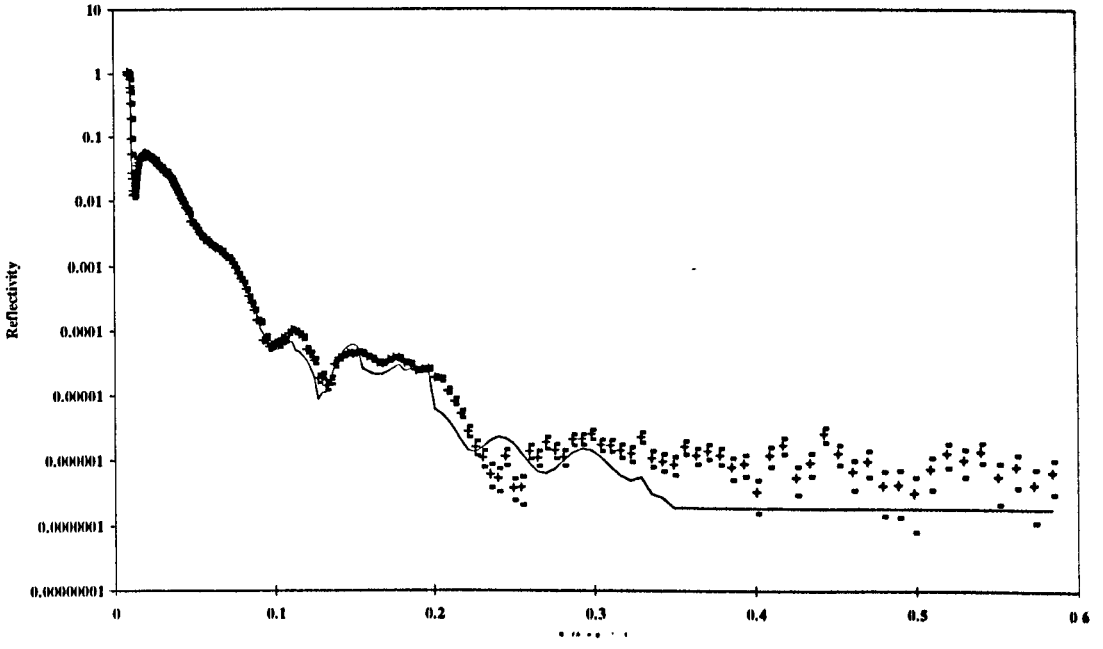

Figure 18a) Showing the best fit that could be obtained for S17 using a block model. χ^2 is not available. Errors are shown by the small dashes above and below each data point.

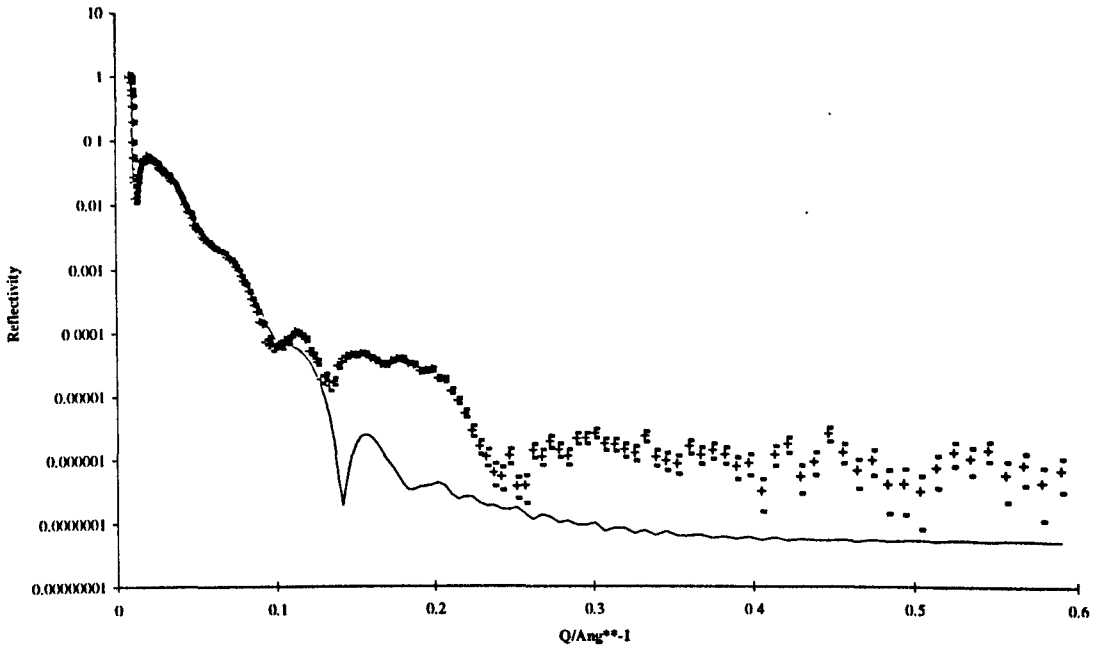

Figure 18b) Showing the excellent fit to S17 obtained using the gaussian model, within the limits of this approach as discussed in the text. $\chi^2 = 2.65$, for the fit below Q = $0.1 Å^{-1}$. Errors are shown by the small dashes above and below each data point.

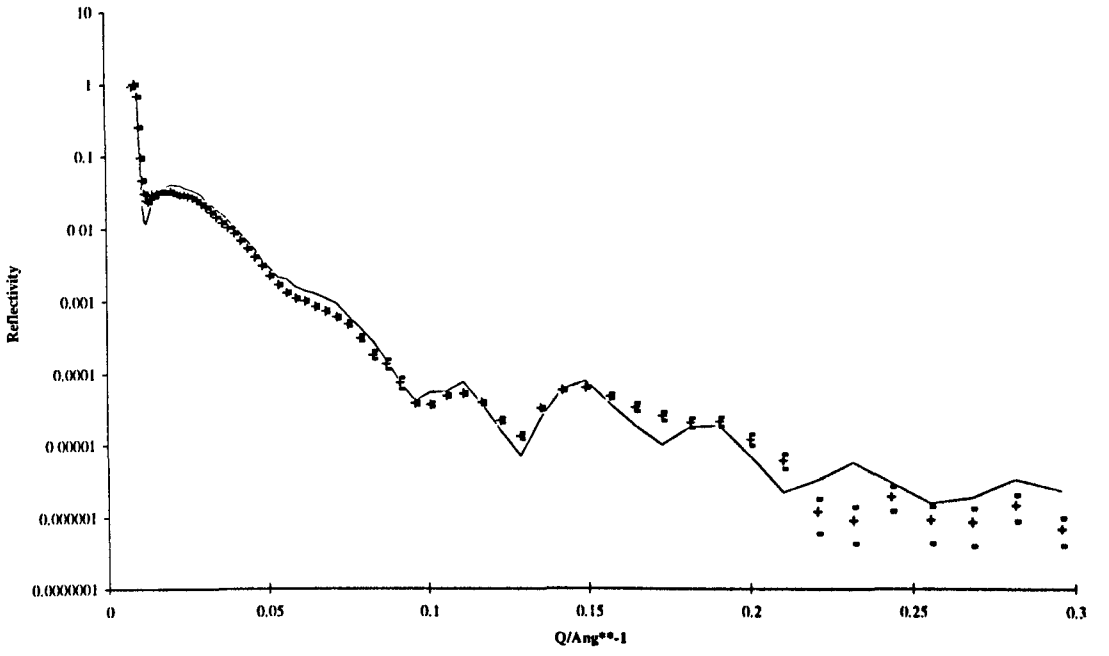

Figure 19 Showing the fit available to S1, using the block model and assuming 24% mixing, as detailed in the text. χ^2 is not available. Errors are shown by the small dashes above and below each data point.

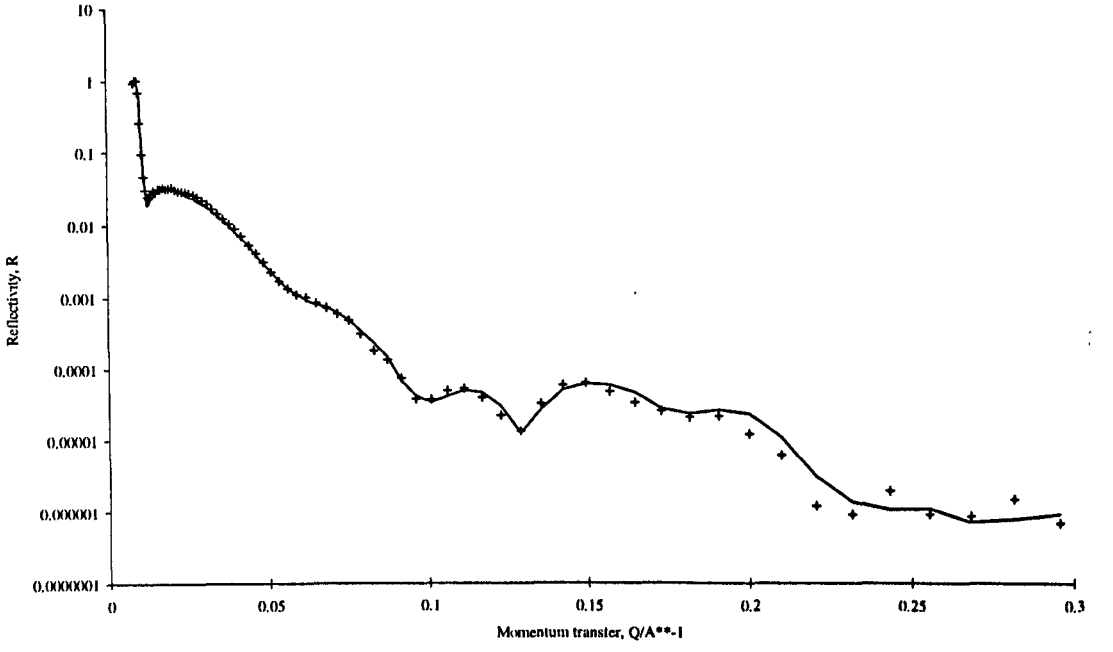

Figure 20a) Comparison of neutron data from S1 (++++) and S3 (——). See text for discussion.

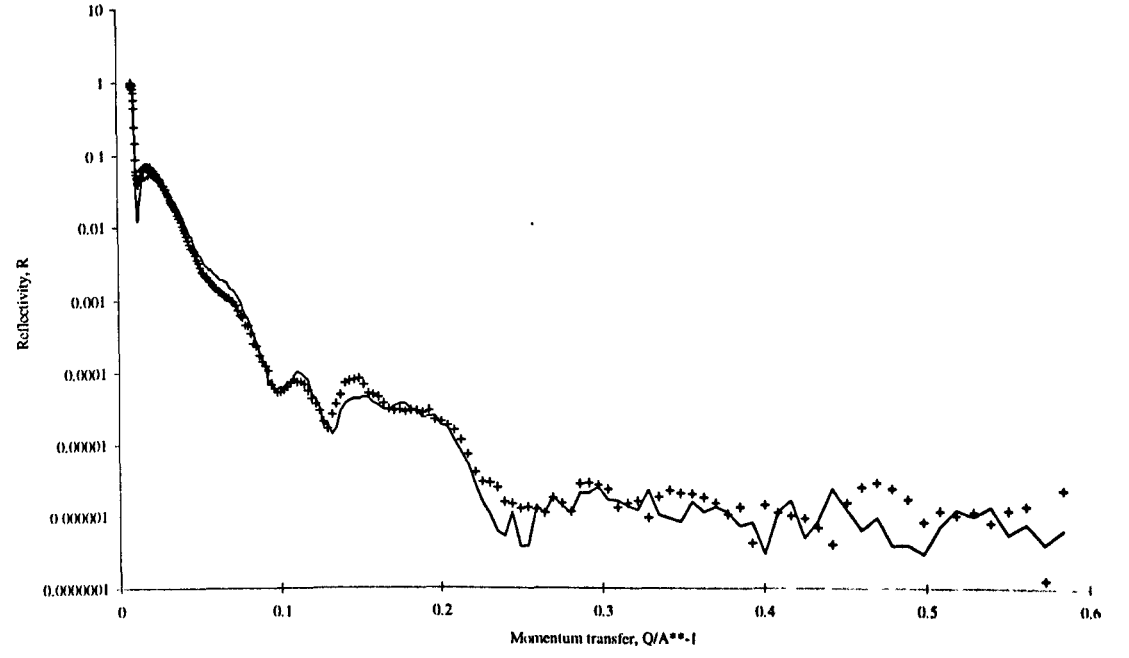

Figure 20b) Comparison of neutron data from S16 (++++) and S17 (——). See text for discussion.

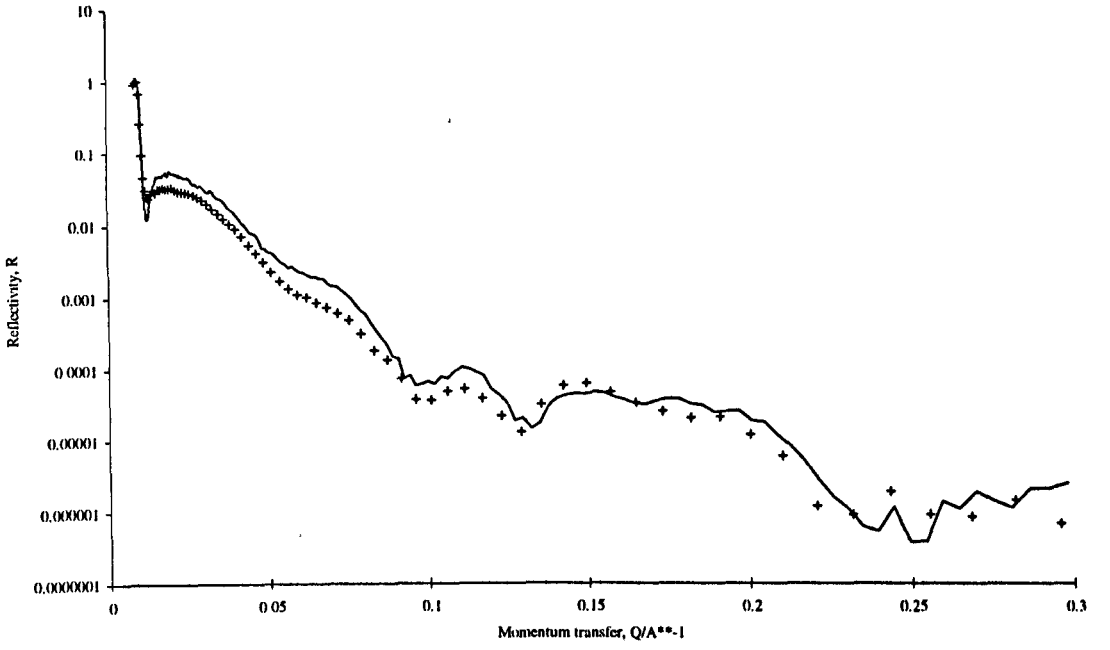

Figure 20c) Comparison of neutron data from S1 (++++) and S17 (—). See text for discussion.

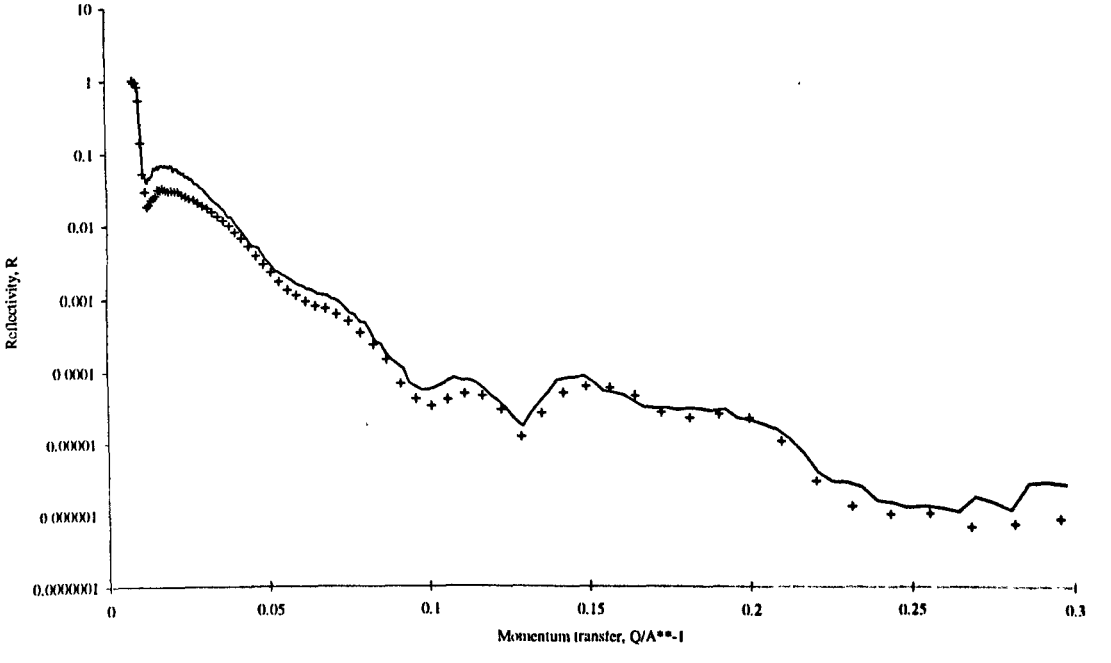

Figure 20d) Comparison of neutron data from S3 (+++) and S16 (—). See text for discussion.

It should be noted that a Langmuir film of docosanoic acid at 40mN/m is very much more rigid (viscous) than a Langmuir film of the same molecule at 30mN/m and has very different flow characteristics, chiefly that the rigid film is non-Newtonian, whereas the fluid film shows Newtonian behaviour [5a-c]. Thus, it may be seen that dipping pressure (i.e. film viscosity) must be matched with an appropriate dipping speed in order to achieve similar film structures and degrees of order. This observation is readily explained by considering the flow of the Langmuir monolayer onto the substrate. If a rigid film is dipped too fast, e.g. 15mm/min, it is easy to envisage the film being "ripped" rather than flowing smoothly, resulting in holes throughout the structure and a more scrambled film, as evidenced by a larger σ and lower DSUB. The holes in the Langmuir film, since they would inevitably be close to the dipped substrate, would not register a drop in π at the Wilhelmy plate. Hence the feedback loop would not be activated, π would not be kept completely constant over this small region and the holes would be transferred onto the substrate with the surrounding monolayer.

Conversely, dipping a rigid film at 5mm/min gives an ordered structure, explained by the slower speed allowing the monolayer to flow onto the substrate more smoothly and thus resulting in fewer holes through the structure of the dipped film.

Dipping the fluid film at the faster speed (S17) also results in fewer holes and hence less mixing, as shown by the higher DSUB.

Dipping the fluid film at the slower speed results in a more scrambled film (lower DSUB) and this is probably due to the slow speed interfering with the rearrangement of the molecules from their Langmuir film S phase to their LB film L_2 phase, causing "buckling" of the film. This would very much increase the interfacial roughnesses, and consequently increase the internal disorder of the film. See also the surface potential results, Section 5.5.4.

A further pair of samples which illustrate the effect of dipping speed is S29 and S30. These were both dipped at 15mN/m, at which point the monolayer is making the transition from L_2 to L_2', and both samples have the deuterated bilayer as the final pair of layers. S29 was dipped at 15mm/min and S30 at 5mm/min. DSUB would be expected to

be 248Å for these samples, and indeed it is 248Å for S30, whereas DSUB for S29 is 227Å, implying a greater extent of mixing, since the centre of gravity of the gaussian is lower than expected. Values for σ are very similar, at 32.4Å, 8.1Å and 32.1Å, 8.1Å (the two-sided gaussian model was used for these samples, since the D-layer is at the air), showing up a further potential shortcoming of the gaussian approach, which would be rectified by the extra flexibility of the block model with two half-gaussians. See also the discussion in Section 5.5.3.1. Nevertheless, a useful conclusion can be drawn, namely that this very fluid film, on the cusp of two phases, needs to be dipped slowly if an ordered film is to result, providing further evidence that the phase of the monolayer requires consideration, and confirming the theory outlined above on how scrambling could occur at the point of dipping.

5.5.3.3 Temperature.

Consider S2 (18°C) against S24 (30°C), otherwise identical dipping conditions, i.e. 40mN/m, 15mm/min and HHHHD (nomenclature as in Table 1).

S2 has a DSUB of 271 Å and σs of 38 Å and 8.1 Å.

S24 has a DSUB of 381 Å and σs of 60.8 and 8.1 Å.

As has already been mentioned, the docosanoic acid Langmuir film at 30°C was extremely fluid and this has caused the effective thickness of the film to be much larger than expected, most likely due to the buckling proposed in the previous section. Hence, while DSUB remains at the air-film interface, the D-layer has penetrated down into the film by 119 Å, compared with 80 Å for S2. Thus DSUB and σ continue to give consistent results. The sample also shows that a certain amount of order is required in the Langmuir film, if the subsequent LB film is to have order.

5.5.3.4 Time Under Water.

Consider S13 against S15, the latter having been left under water for 10 minutes between the down and up-strokes of the D-layer deposition. Otherwise identical dipping conditions, i.e. 35mN/m, 15mm/min and HHHHDHHHH (nomenclature as in Table 1).

S13 has a DSUB of 265 Å and σs of 32.7 and 8.1 Å.

S15 has a DSUB of 263 Å and σs of 33.4 and 8.1 Å.

Thus it is clear that, well within errors (see Table 2), the extra time under water has had no effect whatsoever on the distribution of the D-layer within the LB film. An interesting further experiment would be to use a hydrophilic substrate, so that one monolayer of D-acid could be dipped rather than a bilayer.

5.5.3.5 Effect of Subphase Ions.

The plot of X-ray data from S7 and S11 in Figure 21 illustrates the difference due to the presence of cadmium ions, which are known to make the molecules more perpendicular (Chapter 2, Section 2.2.4) and hence make the dipped film thicker. The DTOT values for the two Cd^{2+} films, i.e. S10 and S11, give a mean DMON of 29.6Å, compared with 30Å for the fully-extended molecule, and the value of DMON of 27.6Å for the acid dipped over plain water. This result is very close to that of other workers, and is therefore helpful in showing that the experimental technique used here is of the same standard as that of other published work.

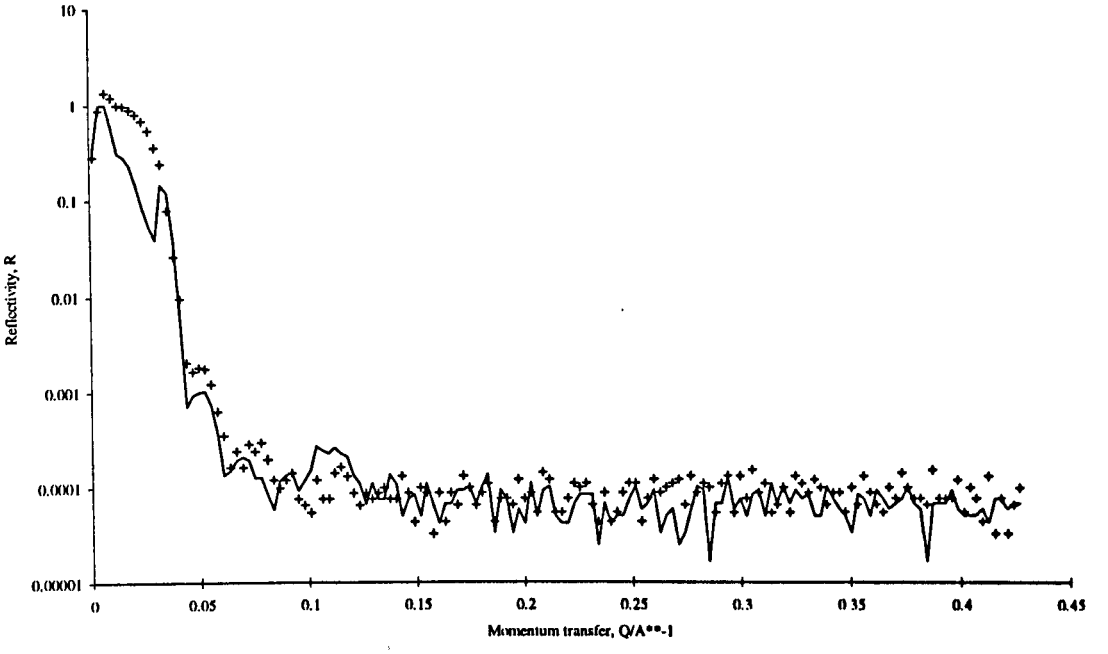

Figure 21 X-ray data from S7 (++++) and S10 (——), illustrating the effect of cadmium ions on the film thickness. It can be seen that the Kiessig fringes in the S10 data are shifted to slightly lower Q than those in the S7 data, indicating that S10 is a thicker film.

5.5.4 Surface Potential Results.

As discussed earlier in this chapter, in Section 5.4.2, the qualitative picture of the monolayer that this technique provides, namely of a film at 25mN/m being fluid and in constant motion, one at 30mN/m being steady and one at 40mN/m picking up all external vibrations, gives very useful evidence of the influence of the phase of the monolayer on its dipping behaviour. These results therefore fully support the observations on film quality at different surface pressures, as discussed in the previous sections, and help to explain them. For instance, at 25mN/m, the monolayer appears to be moving constantly, and it follows that this would produce uneven films, whatever the dipping speed. At 30mN/m, the film has no obvious internal movement on the scale detectable by the surface potential technique, i.e. of the order of 2-5mm, and it will

therefore dip uniformly at a speed of 15mm/min. However, at the slower speed of 5mm/min, the size and time scale of the fluctuations in the monolayer become significant and a disordered film results. At 40mN/m, the film is rigid and sensitive to disruption, due to its non-Newtonian flow characteristics. This explains why a slow dipping speed is therefore needed to give an ordered film, whereas a faster dip speed disrupts and "tears" the monolayer, resulting in a disordered film.

5.5.5 Samples with large errors.

As promised in Section 5.5.2, the nine samples with unreasonably large errors in NBHF, namely S1, S3, S6, S10, S15, S19, S22, S27 and S28, will now be considered, in the light of the surface potential results above. Pertinent details of these samples are summarised in Table 6 below.

Sample	π, dip speed and other brief details, from Table 1	Deposition ratio from Table 4
S1	40mN/m, 15mm/min, HHDHH	108%
S3	30mN/m, 5mm/min, HHDHH	106%
S6	40mN/m, 15mm/min, HHHHDHHHH (X-rays only)	107%
S10	40mN/m, 15mm/min + Cd^{2+}, HHHHD	91%
S15	35mN/m, 15mm/min, HHHHDHHHH	96%
S19	40mN/m, 15mm/min, PPDPP	81%
S22	40mN/m, 15mm/min, DDPDD	96%
S27	20mN/m, 15mm/min, HHHHD	100%
S38	25mN/m, 15mm/min, DDDDD	109%

(Caption overleaf)

Table 6 Brief preparation details summarised for the nine samples which show large errors in NBHF values.

It will be readily observed that most of these samples fall into one or other of the disordered monolayer categories above: S1, S6, S10, S19 and S22 were all a viscous film dipped fast, while S3 was a fluid film dipped too slowly. The remaining three samples shed interesting light on two regions of the isotherm which have not been explored as thoroughly. Given that S15, i.e. 35mN/m, produces a disordered film at 15mm/min, the monolayer must be much more viscous at this π than a monolayer at 30mN/m. It would be fruitful to extend the viscosity measurements reported in [5a-c] into this surface pressure range. In a similar vein, S27 and S38 lend support to the theory outlined in Section 5.5.3.2, namely, that such fluid monolayers require a slower dipping speed to produce ordered layers, due to phase changes in those regions of the isotherm. These are very consistent and encouraging results, and it would be helpful to do more work to verify these conclusions.

5.6 Summary.

It has been shown that, by having only one D-labelled bilayer in an LB film, a greater understanding may be reached of the factors affecting the scrambling of that D-layer into the surrounding film. It has also been shown that, as is to be expected, each dipped layer fills up the holes in preceding layers, and dipping conditions have been found which optimise the integrity of the monolayer, thus reducing the formation of those holes and consequently reducing scrambling of the D-layer. These conditions rely on a thorough understanding of the monolayer being used and on a balance being struck between film fluidity and dipping speed, i.e. a fluid film (30mN/m) can be dipped fast (15mm/min) to give an unscrambled film, whereas a more rigid viscous film (40mN/m) needs to be dipped slowly (5mm/min) to give an unscrambled film. Under these conditions, scrambling of the D-layer may be reduced to a minimum, as shown by the DSUB and σ values obtained from fits to the neutron reflectivity data, and five samples have been prepared where this is the case, covering a range of preparation conditions. These five samples are S1, S3, S14, S16 and S17.

Musgrove [8] found evidence of mixed phases in all the films examined in that work. The present work has extended this and established a link between these phases and the experimental conditions, with the result that it is possible to prepare LB films of a single phase by rigorous and systematic control of the dipping conditions. In addition, and in contrast with the findings of Musgrove [8], it has been shown that it is possible to use acid rather than salt Langmuir films to produce reproducible, ordered LB films. This removal of metal ions from the system is a further simplification, making the modelling more straightforward and hence, in principle at least, more reliable. This in turn has led to a more fundamental understanding of the dipping process, with encouraging results for producing ordered alternating LB films. In conclusion, it can be stated, with a high degree of confidence, that the results from the present work show that a Langmuir film of a fatty acid has to be in the S phase, and must be dipped at a rate which ensures

complete and uniform transition to the L_2 phase during deposition, to achieve an unscrambled LB film.

5.7 Further Work.

As mentioned in several of the preceding sections, it would be desirable to take the modelling further, for instance to obtain fits out to higher Q and thus gain information on the smaller-scale structure of the samples. More development work is needed on the block model with two half-gaussians. On the practical side, the conclusions would be strengthened by increasing the number of samples within the dipping parameter matrix, and the work described in the next chapter will start this process. It would be particularly interesting to investigate a broader range of dipping speeds. The surface potential measurements need to be verified, and Brewster angle microscopy could be a useful technique for this, particularly if a video camera were used. The viscosity of films at high (above 30mN/m) pressures could be usefully measured, to add to general monolayer understanding. Low pressure monolayers (below 25mN/m) could also be investigated, using a technique such as Brewster angle microscopy, with a view to verifying the theory on the importance of monolayer phase in this lower region of the isotherm. As to characterising LB films, infra-red spectroscopy is now a highly sensitive technique which could usefully be applied to LB films to aid further study into molecular orientation in the various phases, especially the technique of attenuated total reflection, which is particularly suited to thin layers such as LB films. As mentioned in Chapter 2, atomic force microscopy is also applicable to LB films, and could be used to quantify monolayer and LB film integrity. X-ray and neutron reflectivity are the most informative techniques for the study of the internal layer structure of an LB film; a technique such as ellipsometry is not so useful, as it gives only information on the bulk of the sample and cannot resolve individual parts of the system, due to their very similar refractive indices to the light wavelengths used. Finally, it would be very useful to quantify the deposition ratios of the samples prepared in the present work, by dipping samples under identical conditions but on a wafer polished on both sides.

5.8 References.

[1] C. Bower, S. Froggatt, R. Laycock, R. J. Musgrove, R. M. Richardson, G. Rozario, A. Zarbakhsh, J. P. R. Webster, J. S. Hill, D. Lacey and G. Nestor, Mol. Cryst. Liq. Cryst. **261**, 437 (1995).

[2] J. R. Lu and R. K. Thomas, Nucl. Instr. Meth. in Phys. Res. A, **354**, 149 (1995).

[3] M. J. Grundy, R. J. Musgrove, R. M. Richardson, S. J. Roser and J. Penfold, Langmuir, **6**, 519 (1990).

[4] A. M. Bibo and I. R. Peterson, Adv. Mater. **2**, 309 (1990).

[5a] M. Buhaenko, J. W. Goodwin, R. M. Richardson and M. F. Daniel, Thin Solid Films, **134**, 217 (1985).

[5b] M. R. Buhaenko, J. W. Goodwin and R. M. Richardson, Thin Solid Films **159**, 171 (1988).

[5c] M. Buhaenko, PhD thesis, University of Bristol, 1988, and references therein.

[6] S. J. Roser and M. R. Lovell, Thin Solid Films, **285**, 166 (1996).

[7] U. Englisch, T. A. Barberka, U. Pietsch and U. Höhne, Thin Solid Films, **266**, 234 (1995).

[8] R. J. Musgrove, PhD Thesis, Bristol 1990.

Chapter 6. Carboxylic Acid-Fatty Amine Alternating Langmuir-Blodgett Films.

6.1 Introduction.

This chapter describes the work done on and results obtained from carboxylic acid/fatty amine alternating LB films, using four different carboxylic acid molecules, and H- and D-amines to enable labelling for neutron reflectivity work. The modelling results from Chapter 5 proved invaluable for the data analysis of these samples, thus confirming the validity of the gaussian approach for analysis of reflectivity data from LB films.

6.2 Background.

It is well established that fatty acid/amine alternating LB films show a significant pyroelectric response [1], and this is due to proton transfer between the head groups [2]. In addition, the strong hydrogen-bonding of the amide linkage between the head groups should maximise order between layers as the film is built up. Polymeric molecules, by virtue of their size, are expected to enhance structural order still further, as such bulky molecules are less able to migrate through a film. For these reasons, work was done in collaboration with Dr. T. Richardson (Centre for Molecular Materials, University of Sheffield) and Dr. D. Lacey (School of Chemistry, University of Hull) to study alternating LB films of polymeric carboxylic acids and fatty amine by neutron and X-ray reflectivity, with a view to increasing the understanding of the contribution of structural order to the pyroelectric effects observed in LB films of these molecules [2, 3 and 4]. To provide smooth continuity with the work described in Chapter 5, initial samples were prepared using simple fatty acids dipped against the amine.

The reasons for the desirability and usefulness of LB films for pyroelectric devices were mentioned in Chapter 1 and a brief summary of pyroelectric behaviour is given in Appendix 2.

6.3 Experimental.

Three polymeric carboxylic acids were received from the University of Sheffield, all of them with a polysiloxane backbone. One had side chains of an aliphatic carboxylic acid, another had side chains with an aromatic group and the third was the copolymer of these two. Their structures are shown schematically in Figures 1 - 3 and as space-filling models in Figure 4, and a total of 14 samples were dipped altogether. In addition, 8 samples were dipped with a straight chain fatty acid.

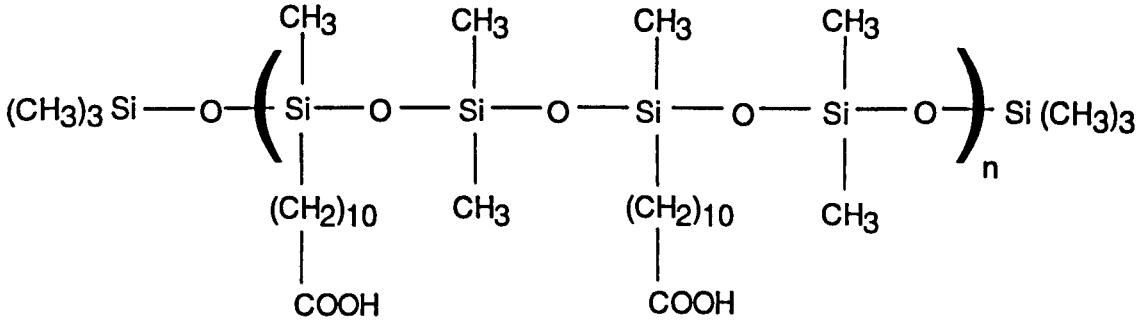

Figure 1 The aliphatic homopolymer, showing the siloxane backbone and the aliphatic side-chains. n is approximately 6.

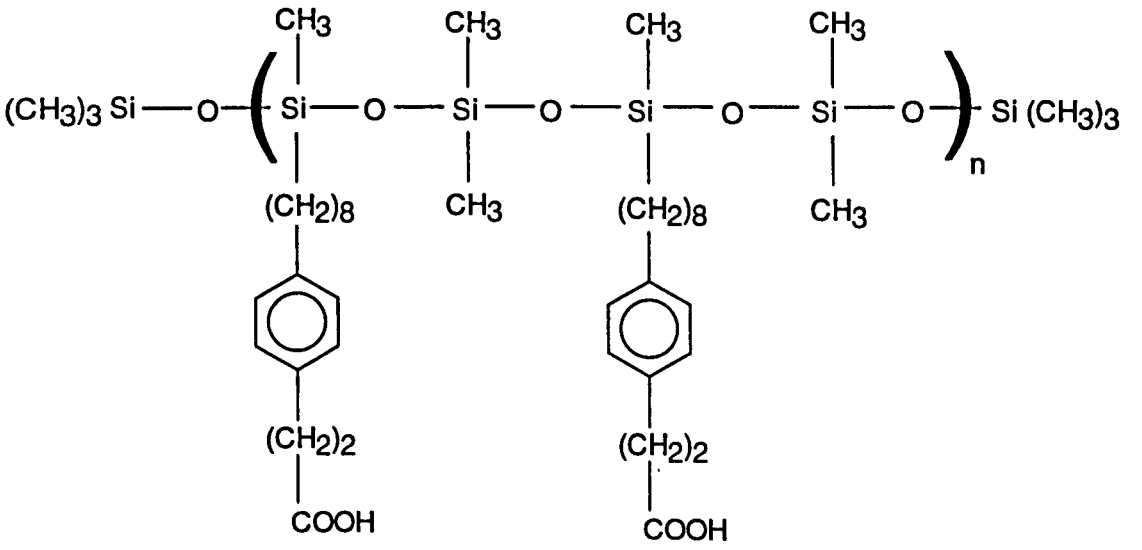

Figure 2 The aromatic homopolymer, showing the siloxane backbone and the aromatic side-chains. n is approximately 6.

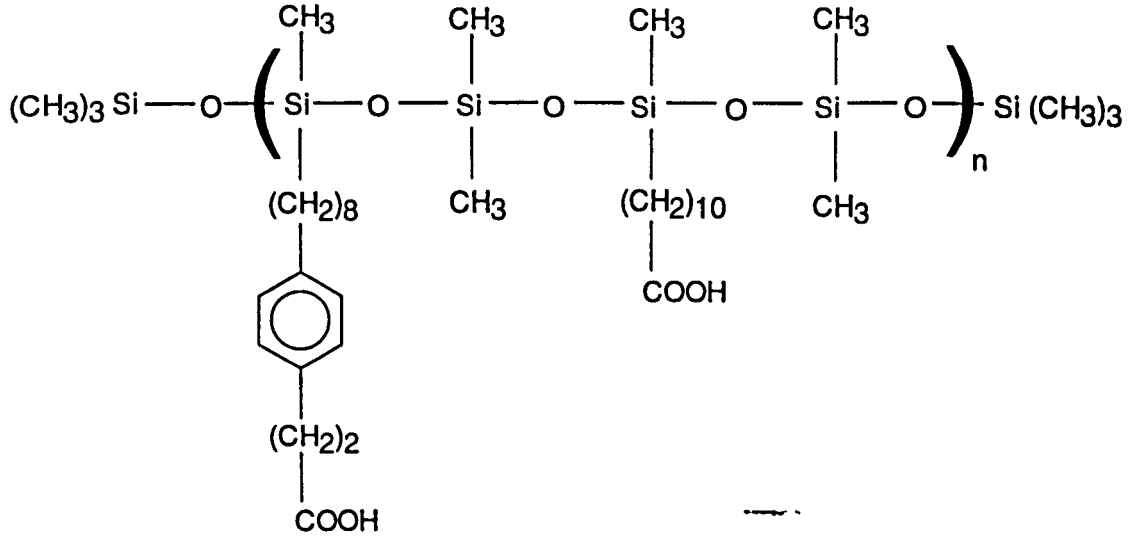

Figure 3 The copolymer, showing the siloxane backbone and the aliphatic and aromatic side-chains. n is approximately 6.

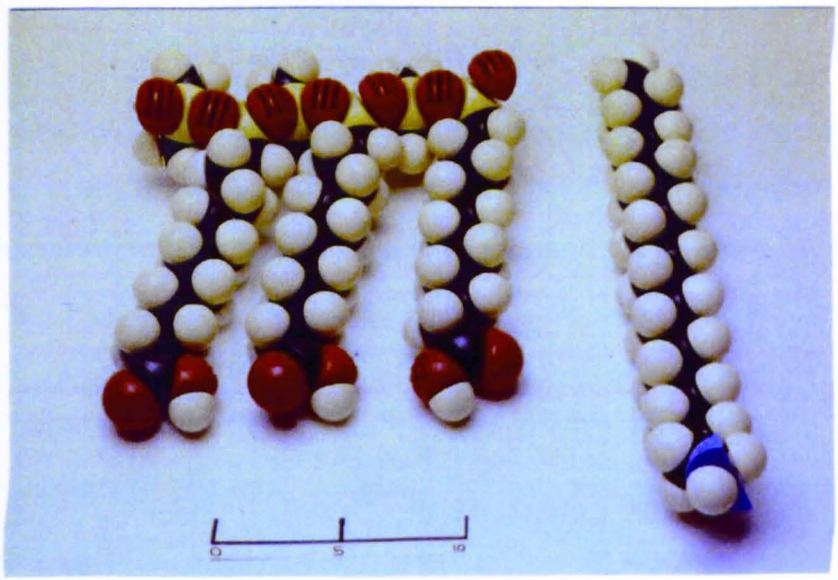

a) the aliphatic homopolymer

b) the aromatic homopolymer

c) the copolymer.

Figure 4 Space-filling (CPK) models of the three polymers. Each is shown alongside the C_{20} amine, and with an approximate Angstrom scale marked below.

The three polysiloxanes form very fluid monolayers, none reaching a surface pressure higher than 40 mN/m. Isotherms illustrating this are shown in Figure 5, along with isotherms of eicosylamine (C_{20}) at three different pH values.

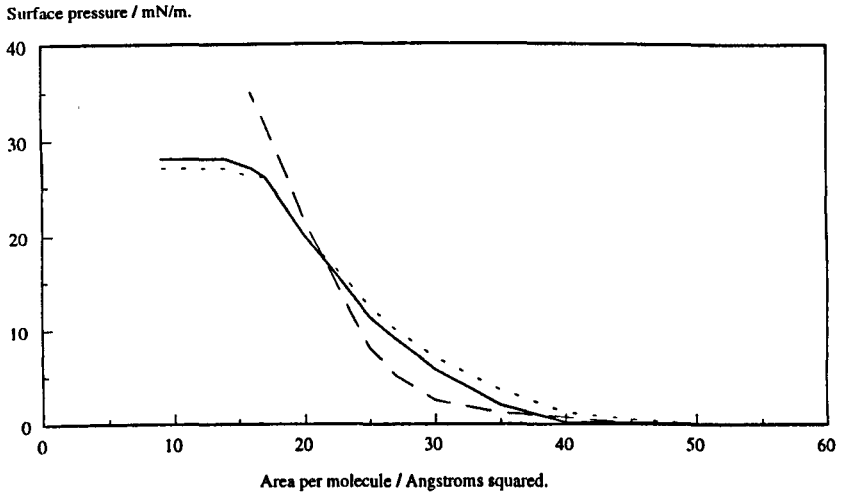

Fig. 5 a)

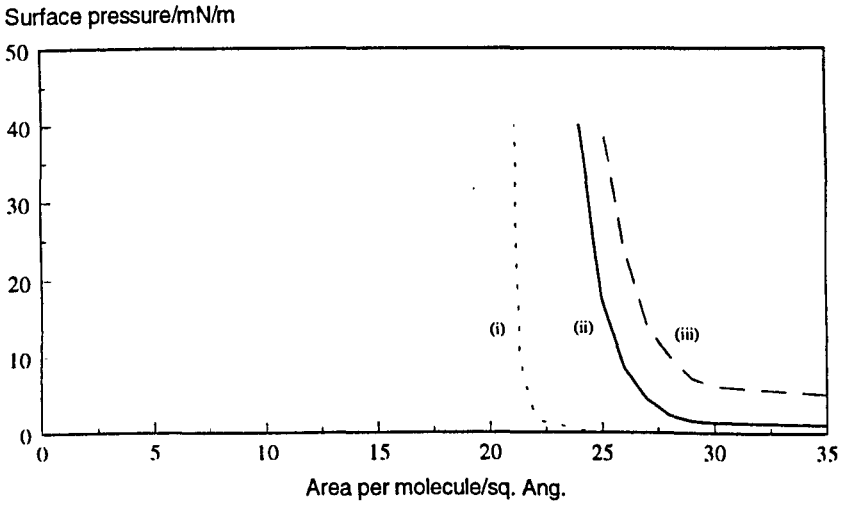

Fig. 5 b)

Figure 5 a) Isotherms of the three polysiloxanes. Solid line - aliphatic homopolymer, short dashes - aromatic homopolymer, long dashes - copolymer; b) isotherms of the amine at (i) pH10, (ii) pH 5.5 and (iii) pH2.

Despite the obvious fluidity of the three polymers, previous workers have reported successful dipping of the copolymer, with the resulting film giving a high pyroelectric response for an LB film consisting of 13 layers of polymer alternating with 12 layers of amine on a hydrophilic substrate [3]. Unfortunately, these workers do not give the dipping parameters they used to prepare their pyroelectric films, beyond stating that their deposition ratios were close to 1.0. Consequently, the present author had to rely on the isotherms of the polymers to choose appropriate dipping conditions.

In previous work, the polymers were usually dipped against a long-chain fatty amine, namely eicosylamine (C_{20}). For the present X-ray and neutron work they were dipped against the same amine but, in the light of the fatty acid work described in Chapter 5, where the presence of just one D-bilayer provides much information on the film structure, just one amine monolayer in each sample was perdeuterated. A single D-labelled monolayer is sufficient to provide a sharp change in the SLD profile through the sample, unless it has been scrambled through the structure, in which case there is no such contrast. The resultant neutron reflectivity profiles are markedly different in the two cases. Further D-labelled layers within the structure only serve to confuse the analysis, at least at this early stage.

The order in which the two molecules are dipped is important, i.e. whether acid-amine or amine-acid. Smith et al. [5] stated that they dipped films exclusively amine-acid, but they do not give their rationale for this. Christie et al. [1] do, however, present clear evidence that amine-acid films are noticeably more reproducible than acid-amine films, as measured by the consistency of their surface potential measurements on several samples at a variety of thicknesses. For example, from their graph, the surface potential varies by as much as 150mV over 8 samples three monolayers thick dipped acid-amine, but by only 25mV over 8 samples of the same thickness dipped amine-acid. Therefore, in the present work, only two samples were dipped acid-amine, to verify the observations of Christie et al. [1], and the remainder were dipped amine-acid.

Table 1 shows the film samples which were prepared. Note that only one sample (S40) was dipped at a slower speed. All samples were dipped over 18 MΩ water at ambient

temperature (18°C) and pH (~ 5.1 - 5.5). The pH could not be adjusted to pH3 as for the samples in Chapter 5, because at such a low pH the amine monolayer is completely ionised and hence expanded over the un-ionised state, affecting monolayer behaviour ([6] and see Fig. 5b above). However, the optimum pH for amines is at or above pH10, at which point the acid headgroups would be completely ionised. Ambient pH was chosen as a compromise, and monolayer stability was found to be very good for both docosanoic acid and the eicosylamine. The polymeric acids were not found to be particularly affected by pH, so ambient pH was appropriate for them too. Samples S40, S41 and S42 were not examined by X-rays, since they had been examined by neutrons at both room temperature and 50°C, which affected their structures: subsequent X-ray experiments would not have yielded information on the initial order of the films. Due to time constraints, samples S56, S57, S60 and S61 were not examined by neutrons. With these exceptions, all samples were examined both by neutrons at RAL and subsequently by X-rays in-house at Bristol.

Sample number	Structure	Dipping pressure, mN/m	Dipping speed, mm/min
S40	HAHADAHAHA	H, D 30; A 28	5
S41	HAHADAHAHA	H, D 30; A 28	15
S42	AHAHADAHAH	H, D 30; A 28	15
S43	AHAHBHAHAH	A, H, B 30	15
S44	BHAHAHAHAH	A, H, B 30	15
S45	AHAHAHAHBH	A, H, B 30	15
S46	ALALBLALAL	A, B 30; L 20	15
S47	BLALALALAL	A, B 30; L 20	15
S48	ALALALALBL	A, B 30; L 20	15
S49	AMAMBMAMAM	A, B 30; M 20	15
S50	BMAMAMAMAM	A, B 30; M 20	15
S51	AMAMAMAMBM	A, B 30; M 20	15
S52	ACACBCACAC	A, B, C 30	15
S53	BCACACACAC	A, B, C 30	15
S54	ACACACACBC	A, B, C 30	15
S55	ACACBCACAC	A, B, C 30	15
S56	ACACBCACAC	A, B, C 30	15
S57	ACACBCACAC	A, B, C 30	15
S58	BCBCBCBCBC	A, B, C 30	15
S59	ACACACACAC	A, B, C 30	15

...cont.

Sample number	Structure	Dipping pressure, mN/m	Dipping speed, mm/min
S60	AHAHAHAHAH	A, H 30	15
S61	**BHBHBHBHBH**	**B**, H 30	15

Table 1 The samples prepared. Each letter in the structure column represents a monolayer. H is the fatty acid, **D** is the perdeuterated fatty acid, A is the amine, **B** is the perdeuterated amine, L is the aliphatic homopolymer, M is the aromatic homopolymer and C is the copolymer.

6.4 Modelling the Data.

Again, a layer-by-layer approach resulted in too many independent parameters and consequently very unwieldy modelling. The approach described in Chapter 5, namely the gaussian model, enables the main features of the reflectivity profiles to be fitted with far fewer parameters.

6.5 Results.

As in Chapter 5, the X-ray data were fitted using the single-layer option in Fitnew, to extract DTOT and NBHF, and then the gaussian routine was used to fit the neutron data, to obtain values for DSUB and σ. These results are shown in Tables 2 and 3, and examples of the quality of the fits are shown in Figure 6 for the X-ray data and in Figure 7 for the neutron data. Table 4 gives the relative values for the deposition ratios for these samples, and as in Chapter 5, it must again be stressed that these deposition ratio data can only be used to compare sample with sample and molecule type with molecule type. They can in no way be said to represent actual coverage, due to the fact that deposition on the rear (i.e. ground and hence macroscopically uneven) face of the Si wafers is

uncertain, and was not measured in this work. Therefore quantitative comparison with NBHF and B_A is not meaningful.

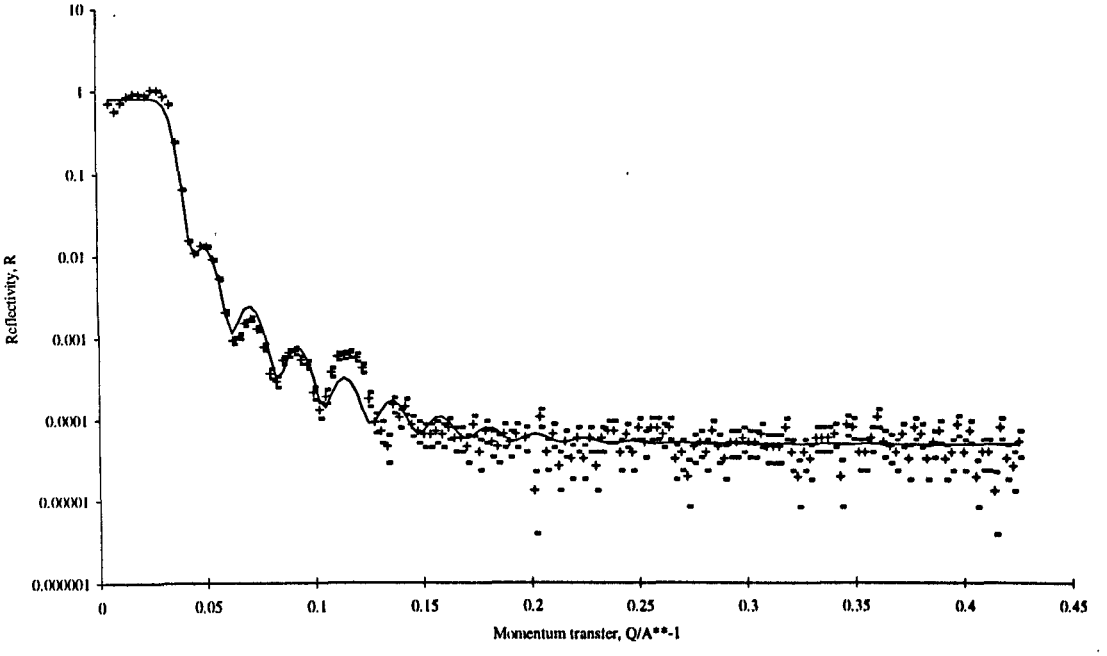

Figure 6 High-quality fit (solid line) to X-ray data (points) for S44. $\chi^2 = 6.07$. Dipping parameters are given in Table 1.

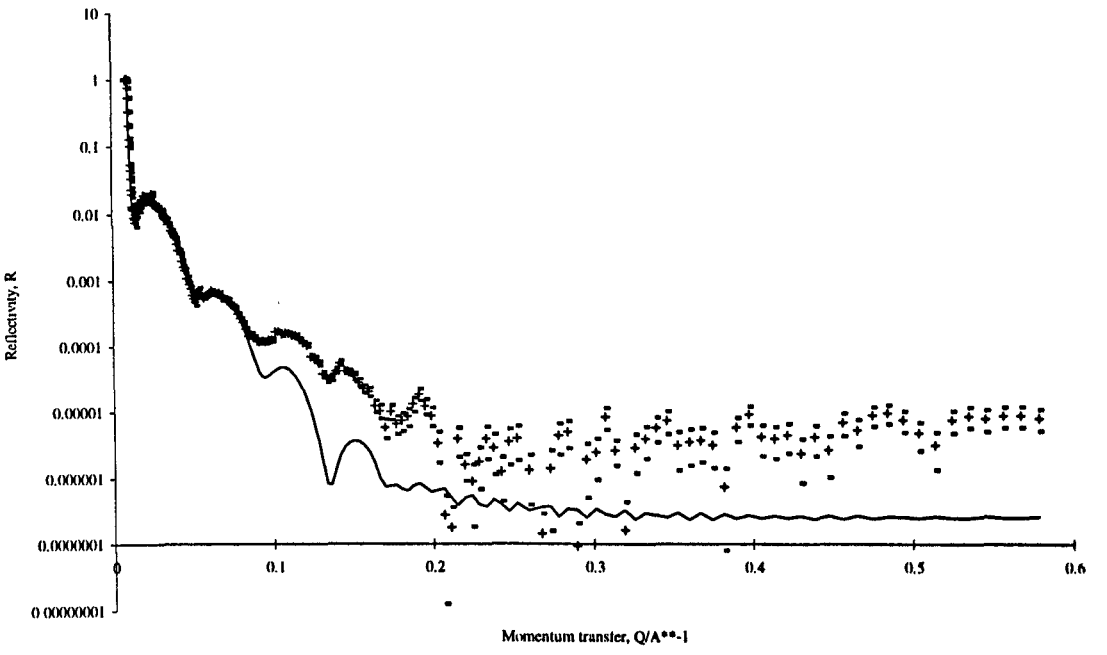

Figure 7 High-quality fit (solid line) to the neutron data from S42 (points), given the limitations of the gaussian approach as discussed in Chapter 5. χ^2 = 0.6. Dipping parameters are given in Table 1.

Errors are again as generated by the fitting routine, based on the confidence in the fit, as described in Chapter 5.

DTOT was used to obtain DMON, as in Chapter 5. Interestingly, the only way to make sense of the DMON values obtained for the amine using the Chapter 5 value of 27.6Å for the acid (28.1Å, compared with 27.2Å for the fully-extended CPK model of the amine) was to conclude that the acid packs differently when dipped against the amine headgroups. A tilt angle of 13° for both molecules would account for the observed bilayer thickness of 55.7Å, significantly lower than the value of 23° for the acid dipped against itself. This suggests that the monolayer packing relaxes on dipping only as far from the upright (S phase) as the L_2' phase, and not all the way to the L_2 phase. This is most likely to be due to the extra strength of the acid/amine bond over the acid/acid bond, which in turn would have an effect on the in-plane interactions between the headgroups, and which would be linked to the pH of the subphase. At pH5.5, the acid monolayer will not be totally un-ionised, whereas it would be at the more usual dipping pH of 3. This will undoubtedly have a positive impact on the effectiveness of the head-to-head binding between acid and amine. Infra-red spectroscopy would be a useful technique to investigate the molecular orientations further.

Of course, another possibility is that the DMON value for the acid in Chapter 5 is incorrect, but given the high degree of consistency between the DTOT values from the X-ray data, this is considered unlikely.

In conclusion, this is a significant result, and this author is not aware that this has been reported prior to this work.

Sample number	DTOT/ Angstroms	DSUB/ Angstroms.	SIGMA/ Angstroms.
S40	n/a	n/a	
S41	n/a	131.0 ± 0.8	15.3 ± 0.4
S42	n/a	153.0 ± 0.3	16.3 ± 0.2
S42, 50°C	n/a	160.0 ± 0.3	19.4 ± 0.2
S43	272 ± 3	128.0 ± 0.3	12.9 ± 0.1
S44	281 ± 2	n/a	
S45	269 ± 4	240.0 ± 0.6	10.5 ± 0.4
S46	289 ± 4	74.7 ± 0.5	45.6 ± 1.8
S47	230 ± 3	n/a	
S48	302 ± 42	62.6 ± 1.0	49.8 ± 1.0
S49	n/a	102.0 ± 2.0	59.3 ± 0.9
S50	210 ± 7	n/a	
S51	n/a	132.0 ± 3.4	131.0 ± 12.5
S52	216 ± 4	102.0 ± 2.2	74.6 ± 1.9
S53	216 ± 13	n/a	
S54	220 ± 9	n/a	
S55	216 ± 5	107.0 ± 2.0	77.6 ± 3.2
S56	215 ± 7	n/a	
S57	218 ± 21	n/a	
S58	n/a	n/a	
S59	235 ± 7	n/a	
S60	284 ± 7	n/a	
S61	287 ± 4	n/a	

Table 2 DTOT values from fits to the X-ray data and DSUB and SIGMA values from fits to the neutron data.

Sample number	X-ray NBHF/ x 10^{-5} Å.	Coverage determined by X-rays/%	Neutron B_A/ x 10^{-3} Å.	Coverage determined by neutrons/%.
S40	n/a		n/a	
S41	n/a		0.200 ± 0.002	87.7 ± 0.9
S42	n/a		0.198 ± 0.001	86.8 ± 0.4
S42, 50°C	n/a		0.186 ± 0.001	81.6 ± 0.4
S43	1.01 ± 0.067	108 ± 7	0.191 ± 0.001	86.4 ± 0.4
S44	1.24 ± 0.058	133 ± 6	n/a	
S45	0.932 ± 0.074	100 ± 8	0.206 ± 0.002	93.2 ± 0.9
S46	0.901 ± 0.019	115 ± 2	0.209 ± 0.002	98.6 ± 0.9
S47	1.04 ± 0.043	133 ± 5	n/a	
S48	0.561 ± 0.021	72 ± 3	0.223 ± 0.004	105.2 ± 2.0
S49	n/a		0.261 ± 0.010	127.3 ± 4.9
S50	0.727 ± 0.060	76 ± 6	n/a	
S51	n/a		0.214 ± 0.016	104.4 ± 7.8
S52	0.768 ± 0.047	94 ± 6	0.273 ± 0.018	130.6 ± 8.6
S53	0.766 ± 0.207	94 ± 25	n/a	
S54	0.516 ± 0.105	63 ± 13	n/a	
S55	0.875 ± 0.086	107 ± 10	0.209 ± 0.007	100.0 ± 3.3
S56	1.26 ± 0.409	154 ± 50	n/a	
S57	1.12 ± 1.37	137 ± 168	n/a	
S58	n/a		n/a	
S59	0.705 ± 0.078	81 ± 9	n/a	
S60	1.10 ± 0.115	118 ± 12	n/a	
S61	1.00 ± 0.053	107 ± 6	n/a	

Table 3 Values for NBHF and B_A and the film densities they represent. The values for NBHF were obtained from the X-ray data and for B_A from the neutron data.

Sample	1↓ cm^2	2↑ cm^2	3↓ cm^2	4↑ cm^2	5↓ cm^2	6↑ cm^2	7↓ cm^2	8↑ cm^2	9↓ cm^2	10↑ cm^2	Total cm^2	Mean Coverage %
S40	88.5	79.8	75.4	79.8	**74.0**	78.3	72.5	78.3	75.4	78.3	780	101
S41	76.9	81.2	71.1	79.8	**78.3**	78.3	74.0	79.8	75.4	79.8	775	100
S42	60.9	78.3	74.0	81.2	78.3	**79.8**	78.3	79.8	78.3	84.1	773	100
S43	66.7	79.8	76.9	82.7	**75.4**	82.7	76.9	81.2	75.4	82.7	780	101
S44	**65.3**	79.8	76.9	81.2	75.4	81.2	74.0	81.2	74.0	82.7	772	100
S45	63.8	78.3	72.5	82.7	72.5	78.3	72.5	81.2	**75.4**	79.8	757	98
S46	68.2	81.2	62.4	74.0	**72.5**	69.6	74.0	34.8	72.5	39.2	648	84
S47	**58.0**	71.1	71.1	66.7	72.5	76.9	71.1	69.6	74.0	81.2	712	92
S48	62.4	76.9	62.4	74.0	74.0	68.2	69.6	78.3	**76.9**	8.7	651	84
S49	60.9	74.0	66.7	66.7	**75.4**	62.4	75.4	71.1	75.4	72.5	701	91

For Table caption, see two pages on.

Cont.

Sample	1↓ cm^2	2↑ cm^2	3↓ cm^2	4↑ cm^2	5↓ cm^2	6↑ cm^2	7↓ cm^2	8↑ cm^2	9↓ cm^2	10↑ cm^2	Total cm^2	Mean Coverage %
S50	**52.2**	68.2	72.5	74.0	72.5	72.5	75.4	79.8	79.8	75.4	722	93
S51	56.6	52.2	68.2	66.7	69.6	63.8	74.0	74.0	**72.5**	65.3	663	86
S52	72.5	87.0	81.2	87.0	**84.1**	58.0	78.3	68.2	75.4	74.0	766	99
S53	**63.8**	78.3	75.4	65.3	75.4	71.1	75.4	74.0	75.4	75.4	730	94
S54	69.6	82.7	76.9	72.5	78.3	74.0	78.3	69.6	**81.2**	56.6	740	96
S55	65.3	78.3	76.9	71.1	**78.3**	56.6	75.4	68.2	76.9	72.5	720	93
S56	66.7	81.2	75.4	71.1	**72.5**	55.1	74.0	66.7	75.4	71.1	709	92
S57	68.2	79.8	75.4	72.5	**72.5**	55.1	74.0	68.2	76.9	71.1	714	92
S58	**65.3**	78.3	**75.4**	60.9	**74.0**	47.9	**69.6**	49.3	**74.0**	52.2	647	84
S59	71.1	81.2	76.9	72.5	76.9	74.0	78.3	74.0	76.9	75.4	757	98

For Table caption, see following page.

cont.

Sample	1↓ cm^2	2↑ cm^2	3↓ cm^2	4↑ cm^2	5↓ cm^2	6↑ cm^2	7↓ cm^2	8↑ cm^2	9↓ cm^2	10↑ cm^2	Total cm^2	Mean Coverage %
S60	72.5	78.3	74.0	81.2	74.0	78.3	76.9	81.2	76.9	78.3	772	100
S61	**62.4**	79.8	**69.6**	81.2	**74.0**	78.3	**74.0**	82.7	**72.5**	78.3	753	97

Table 4 Relative coverage for each layer of each sample (cm^2), the relative total coverage (cm^2) and the mean coverage (%). As in Table 1, bold type indicates a deuterated layer.

As in Chapter 5, several samples do not have their values filled in in Tables 2 and 3, and again this is because physically reasonable fits could not be obtained for these samples. This is most likely to be due to poor film quality, which gives rise to incomplete coverage, excessive interlayer roughness and, in the case of the neutron data, a resultant lack of detectable contrast in the SLD profile, or, in the case of X-ray data, a film so uneven as to produce a negligible overall electron density.

X-ray reflectivity profiles illustrating the reproducibility between samples S55, S56 and S57 are shown in Figure 8.

Figure 9 shows how little effect the different polymers had on DTOT.

A very clear illustration of the effect of the position of the D-layer on the reflectivity profiles is given in Figure 10.

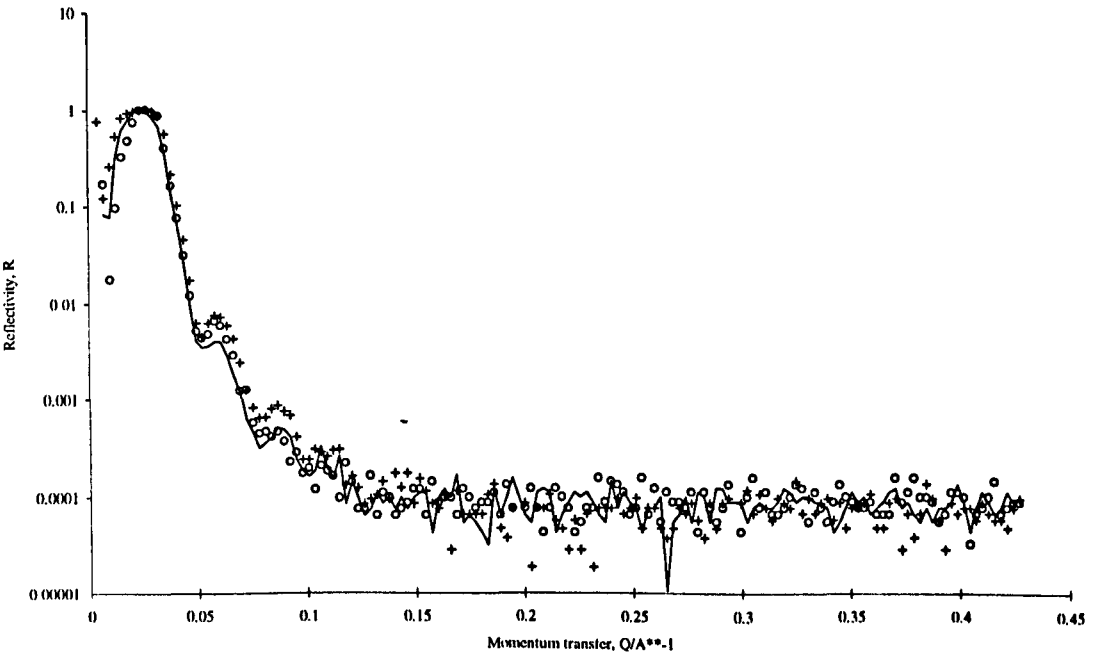

Figure 8 Showing the excellent reproducibility between samples S55 (+++), S56 (—) and S57 (oooo). X-ray data. All three samples are amine/copolymer, ACACBCACAC, dipped at 30mN/m and 15mm/min (nomenclature as in Table 1).

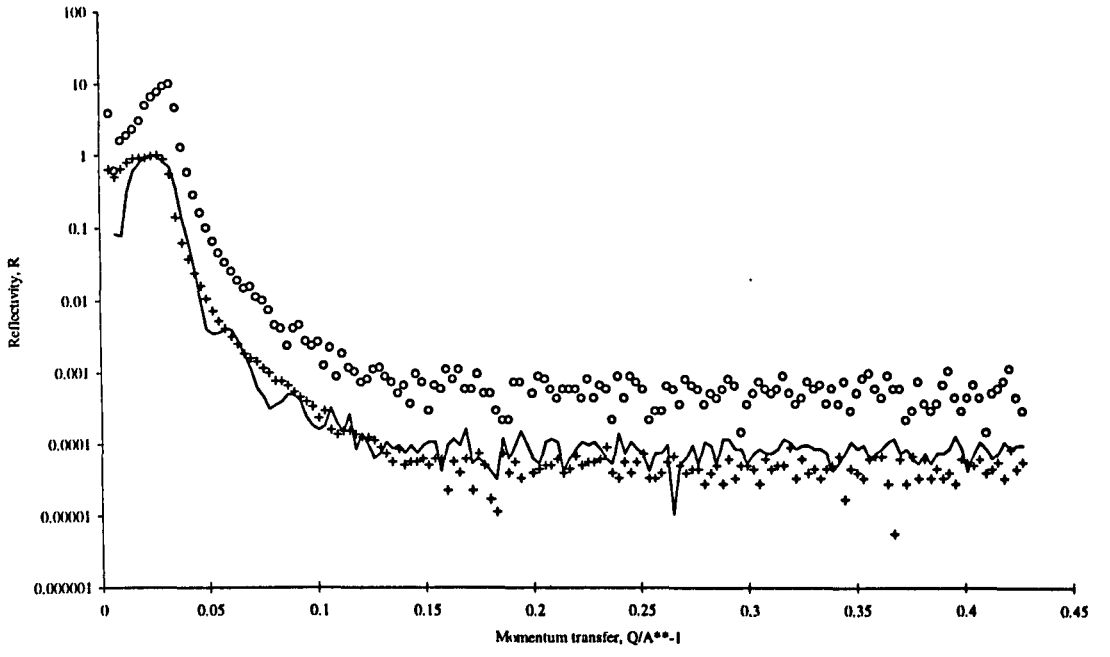

Figure 9 X-ray data from S48 (++++), S56 (—) and S49 (oooo) to show the constancy of DTOT regardless of the polymer type. S49 is shifted by a factor of 10 for clarity. The lack of fringes in S48 and S49 is due to large air-film roughnesses with these samples. S48 ALALALALBL, S56 ACACBCACAC, S49 AMAMBMAMAM; all amine layers and C dipped at 30mN/m, L and M dipped at 20mN/m; dipping speed 15mm/min for all three (nomenclature as in Table 1).

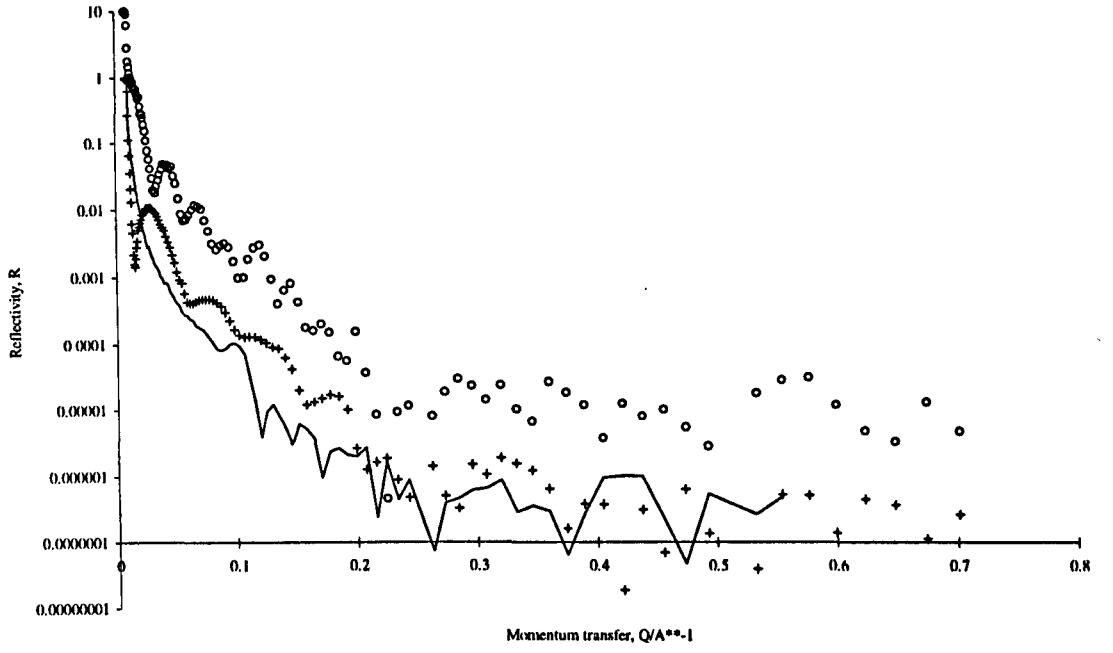

Figure 10 Illustrating the pronounced effect of the position of the D-layer on the fringes in the neutron reflectivity profiles from S43 (+++), S44 (—) and S45 (ooo). Data for S45 shifted by a factor of 10 for clarity. S43 AHAHBHAHAH, S44 BHAHAHAHAH, S45 AHAHAHAHBH; all three dipped at 30mN/m, 15mm/min (nomenclature as in Table 1).

6.6 Discussion and Conclusions.

The data for samples S40 and S41 were inconclusive because of the difficulty of obtaining fits to the data. However, S42 was much easier to fit, and since this sample reversed the dipping order of acid and amine it must be concluded that the S42 orientation (amine first, then acid) confers greater order on the structure, enabling a sensible fit to be more easily obtained. This result thus confirms the work of Christie et al. [1], by reinforcing the evidence in favour of amine-acid versus acid-amine films in terms of reproducibility. The present observation is also in agreement with the theory outlined in section 6.5, concerning the change in packing of the acid - if it is dipped first, it will be in the L_2 phase, and therefore not be in the optimum orientation with respect to the amine headgroups; if dipped second it will be free to adopt the L_2' phase imposed by the amine headgroups. Therefore, this dipping order was used in subsequent amine-acid samples. This headgroup binding is very likely due to the slightly raised pH of 5.5, compared with pH3 for the samples in Chapter 5. At pH5.5, the acid headgroups are not completely un-ionised, and so binding to the amine headgroups will be stronger.

Whilst the increased temperature has caused σ to increase in S42, DSUB has also increased. This is best explained by the temperature rise causing the molecules to "straighten out", thus increasing DMON and hence both DSUB and σ. This conclusion is consistent with the accepted mechanism for the pyroelectric effect, whereby the dipole of the film changes with molecular tilt, i.e. with the vector of the molecular dipole moment (see Appendix 2). In order to confirm this, an identical sample would need to be dipped and examined by X-rays both before and after heating, to obtain values for DTOT and hence confirm any change in molecular orientation. This author was unable to perform this obvious experiment, due to the very much delayed arrival of the deuterated amine, very shortly before the scheduled beamtime at RAL, which left no time for preliminary X-ray investigations.

In support of the theory on stronger headgroup bonds between acid and amine, the DSUB and σ values in Table 2 for S43 and S45 (128Å and 12.9Å, and 240Å and 10.5Å,

respectively) are very close to the theoretical values of 125Å and 7.6Å for a D-labelled amine monolayer dipped in the fifth layer and 236Å and 7.6Å for a D-labelled amine monolayer dipped in the ninth layer. This is a very encouraging result and is further concrete evidence, in addition to that presented in Chapter 5, that an un-scrambled alternating LB film may readily be prepared under the correct conditions. The samples discussed here, and the five in Chapter 5, are the first instances of which this author is aware, that a labelled layer has been shown to have remained in its dipped layer and not to have scrambled into the layer below. In the case of S43 and S45, which are two samples for which there is particularly strong evidence of no scrambling at all, the avoidance of scrambling will almost certainly have been aided by the strong amine-acid headgroup binding, but it will also have been affected by the phase of the acid monolayer after dipping: it is only in the L_2' phase, as evidenced by the layer and film thickness data, and hence has not relaxed as far as the acid films discussed in Chapter 5. This is therefore a major result and adds considerably to current knowledge of LB film scrambling.

The very large σ values for the polymer samples, coupled with the fact that DSUB for these samples is central regardless of where the D-layer was actually deposited, are strong evidence that with all three polymers the film structure is too open to allow the single D-amine monolayer to remain in a discrete layer. This is not surprising, given the extremely fluid nature of the films, as shown by the isotherms in section 6.3. This result also explains the empirical observation made in reference [7], namely, that to optimise the pyroelectric signal in a 13-monolayer film built from one of these molecules and eicosylamine, three bilayers of a fatty acid must be deposited after six active monolayers. From the above and the discussion in Chapter 5, it will be seen that this is readily explained by the fatty acid possessing sufficient monolayer integrity to bridge the defects in the polymer layers, while itself possessing holes too small to allow the next layer of polymer to mix with it.

Given this evidence of extreme mixing of the D-amine layer throughout the polymer LB film, the fact of high pyroelectric coefficients for these materials [3] is somewhat

surprising. It is a natural extrapolation to envisage yet higher pyroelectric coefficients if similar materials could be synthesised with better LB film-forming properties.

6.7 Summary.

It has been shown conclusively that scrambling in an alternating LB film is not a foregone conclusion. Using two molecules whose headgroups bind strongly, namely COOH and NH_2, two samples have been prepared, over a pure water subphase, for which no scrambling at all is needed for an excellent fit to the neutron data. This is a significant result, with implications for the design of appropriate molecules for pyroelectric and SHG applications. Contrary to expectations, large polymeric molecules do not form ordered layers, and this result is supported by empirical observations from other workers [7].

6.8 Further Work.

As in Chapter 5, further work is needed on the modelling, particularly on the block model with two half-gaussians. It may also be a fruitful exercise to attempt to model the totally unscrambled samples S43 and S45 using a layer by layer model, as the step-wise approach to SLD variation is expected to be an accurate model of these samples. It would be helpful to evolve the models to obtain good fits out to higher Q, so as to extract the maximum amount of information from the reflectivity data, and hence establish the smaller-scale structure of the samples. On the experimental side, repeating the fatty acid-fatty amine samples as outlined in section 6.6 would give invaluable extra information on the order within these films and the effect of temperature thereon. It would be extremely interesting to prepare ABAB samples of deuterated amine and hydrogenous acid under the same dipping conditions as S43 and S45, and use neutron reflectivity to provide rigorous confirmation of the unscrambled nature of the films. Pyroelectric measurements would also confirm the unscrambled nature of the films, and infra-red spectroscopy would be a useful tool to investigate the molecular orientations in acid/acid, acid/amine and amine/acid films. A broader temperature range would be a

very interesting study. In the longer term, the design and synthesis of polysiloxanes which exhibit improved LB film-forming characteristics would have promising implications for the future application of LB films in thermal imaging devices.

6.8 References.

[1] P. Christie, G. G. Roberts and M. C. Petty, Appl. Phys. Lett. **48**, 1101 (1986).

[2] C. A. Jones, M. C. Petty, G. G. Roberts, G. Davies, J. Yarwood, N. M. Ratcliffe and J. W. Barton, Thin Solid Films, **155**, 187, (1987).

[3] T. Richardson, W. H. A. Majid, E. C. A. Cochrane, S. Holder and D. Lacey, Thin Solid Films, **242**, 61 (1994).

[4] T. Richardson, W. H. A. Majid, R. Capan, D. Lacey and S. Holder, Supramolecular Science, **1**, 39 (1994).

[5] G. W. Smith, M. F. Daniel, J. W. Barton and N. Ratcliffe, Thin Solid Films, **132**, 125 (1985).

[6] G. L. Gaines Jr., Insoluble Monolayers at Liquid-Gas Interfaces, Wiley, New York (1966).

[7] S. V. Batty, R. Capan, T. Richardson, T. E. Mann and D. Lacey, Thin Solid Films, **284-285**, 919 (1996).

Chapter 7. Conclusions

7.1 Introduction.

X-ray and neutron reflectivity have been used to study the internal order of labelled alternating LB films prepared under a variety of experimental conditions. These experimental parameters, namely dipping speed, dipping pressure, temperature, time under water, the presence or absence of subphase cations and the position of the labelled layer, have been investigated methodically, one by one, to establish which parameters affect the order of the films and how. A new modelling approach has been evolved to fit the reflectivity data, using a gaussian profile for the labelled layer. The materials used to form the LB films have been C_{22} fatty acid, C_{20} fatty amine, a liquid crystal polysiloxane and three polymeric fatty acids, with deuterated C_{22} acid and C_{20} amine being used to label one monō- or bilayer in each sample, at varying positions. Samples have been prepared, of both pure fatty acid and of acid-amine, which are completely unscrambled, i.e. in which the neutron reflectivity data show that the labelled layer has remained in the layer where it was dipped and has not mixed in with the surrounding film. This is a very significant and hugely encouraging result for the future use of the LB technique in pyroelectrics, second harmonic generation and other molecular electronics applications.

7.2 Modelling the Data.

The commonly used layer-by-layer approach to modelling reflectivity data proved inadequate for providing close fits to the neutron data, although single-layer models were perfectly adequate for fitting the X-ray data. This is readily explained by considering the likely distribution of the labelled material in a scrambled film. It is unlikely to have mixed with neighbouring layers in the step-wise fashion inherent in a slab approach, which can only take a relatively small number of slices through the sample before the processing time becomes excessive due to the number of parameters being handled, and

the logical extension is to use a gaussian profile to model a smooth variation in labelled layer content within the thickness of the film. Optical Matrix techniques have been used throughout to maintain the required accuracy, but the Kinematic Model has proved invaluable for visualising the profile and evolving the model. The illustration of the model and its evolution are given in detail in Chapter 5. Initial results with a symmetrical gaussian were promising, and the principle was extended to two half-gaussians, the better to model the likely scenario of labelled material mixing more into the layers below than those above. The bulk of the data were modelled using this approach, with the final evolution of the model consisting of a central block and two independent half-gaussians, one on either side of the block. It will be readily seen that this would provide a yet more representative profile, and would be of particular use in analysing samples where only partial mixing has occurred.

As with all modelling approaches, however, there are limitations to the one used here. Chief among these arises from the Fourier Transform element of the Kinematic Theory. The gaussian profile has a very broad differential function, and the Fourier Transform of this will be therefore be a damping function. This means that data above $Q \sim 0.1\text{Å}^{-1}$ cannot be modelled, since the model decays faster than the RQ^4 decay of the data beyond this Q-range, and so no information on the very small-scale structure of the samples is available. Another limitation is the inherent inability of the gaussian profile to represent the situation of the labelled layer dipped directly onto the substrate as the first layer or bilayer. For this reason, several of the samples prepared (before the introduction of the gaussian model) could not be fitted. A further limitation is the situation with the labelled layer at the air-film interface, although the model with two half-gaussians was able to deal with this considerably better than the symmetrical gaussian model, which is as expected. In any further work in this area it would be interesting to test and develop the block plus two half-gaussians, specifically for films with non-central labelled layers, and to continue to use the simpler two half-gaussians for the study of the majority of other film architectures. Ways of overcoming the damping limitation are not obvious at present.

7.3 Acid-Acid Films.

7.3.1 Phase Change on Dipping.

The film thicknesses obtained from the X-ray data show that the acid monolayer has relaxed from the S phase of the Langmuir film, with upright chains, to a mixture of L_2 and L_2' phases, with a mean chain tilt of 23°. This is contrary to the behaviour observed with salt films, which deposit with a smaller molecular area than in the Langmuir film, and is therefore an important result in terms of new information on the behaviour of acid films. It highlights the fact that they show very different characteristics than do salt films and hence underlines the importance of a thorough understanding of the monolayer phases of the molecule being studied, in order to understand its LB dipping behaviour.

7.3.2 Position of Labelled Layer.

A novel feature of this work was that only one bilayer or monolayer was labelled. This is in contrast to previous work, which has concentrated exclusively on architectures with alternating labelled and non-labelled layers. The present strategy was chosen in order to establish the extent of scrambling and its mechanism more accurately than alternating architectures allow. The deuterated material was deposited as the first, the central or the final bilayer in five- or nine-bilayer samples, or the first, fourth and ninth monolayer in 10-monolayer samples. These differences of position were readily modelled by the gaussian profile technique, with the exception of the situation of the labelled layer being at the substrate. Thus, the gaussian profile is shown to be sensitive to the position of just one monolayer of labelled material, and the present combination of techniques and modelling is shown to be a powerful method for analysing the structure of LB films.

7.3.3 Subphase Cations.

Since the main aim of this work was to study the hitherto neglected pure fatty acid films, only two samples were dipped as salts, over a subphase containing cadmium. These gave data from both X-ray and neutron reflectivity experiments which agree extremely closely with literature values for similar samples. This is helpful in showing that the experimental technique used here is of the same standard as that of other published work. This is a useful benchmark, given the lack of literature data on pure fatty acid films as opposed to salts.

7.3.4 Surface Pressure.

Differences were observed between films prepared at different monolayer surface pressures. Films dipped at 40mN/m were found to be more susceptible to forming disordered films than those dipped at 30mN/m: only one ordered sample was prepared out of 19 labelled samples at 40mN/m, compared with one out of two labelled samples at 30mN/m. This is thought to be due to the increased viscosity of the film at 40mN/m, rendering it less able to flow smoothly onto the substrate during dipping, and hence more likely to have holes within it. Surface pressures below 30mN/m were also unsuccessful for producing ordered films, and in this case it is thought to be because the Langmuir monolayers are in a phase which does not possess sufficient order to transfer as a contiguous film. If the first layer does not deposit in an ordered fashion, the headgroups of the second layer will not have a suitable ordered template for deposition, nor will the chains of the third layer have an even surface to deposit onto, and the disorder will thus be perpetuated throughout the film.

7.3.5 Dipping Speed.

Some very interesting results were obtained from the investigation of this parameter, especially given the consensus in the literature that dipping must proceed at speeds of

around 60mm/min and above in order to minimise the time available under water for molecules to overturn and thus scramble the film. The speeds used here were 5 and 15mm/min, yet even over this small range significant differences were observed. These were that an ordered film resulted if a 30mN/m film was dipped at 15mm/min, whereas a 40mN/m film had to be dipped at 5mm/min if an ordered film was to be obtained. These results are readily explained by consideration of the viscosity of the monolayer. The 40mN/m film is viscous, but can flow smoothly onto the substrate if a dipping speed of only 5mm/min is used; a more rapid speed would cause the substrate to move faster than the monolayer could flow onto it, resulting in holes in the monolayer as it reached the substrate and hence a disordered LB film. Conversely, dipping the 30mN/m film at only 5mm/min allows the phase change on dipping to produce disordered films, whereas at 15mm/min the phase change is reproducible and gives ordered films. The surface potential measurements discussed later (Section 7.3.8) shed extra light on this behaviour.

7.3.6 Time Under Water.

Contrary to the literature consensus, films left under water for 10 mins in between the down- and upstrokes of the labelled bilayer were shown to be identical to films of similar structure which were not subjected to extra time under water, as revealed by the neutron reflectivity profiles. This finding casts doubt on the theory that scrambling is caused by molecules overturning whilst under water.

7.3.7 Temperature.

One sample was dipped at 30°C, at which temperature the monolayer is extremely fluid and in the L_2 phase. It was found to have no internal order, with the labelled bilayer (dipped as the topmost bilayer) distributed throughout the whole of the preceding film. This is further evidence that a certain amount of monolayer order is required to dip an ordered LB film, and is consistent with previous work on viscosity, which found that for C_{22} acid at pH3, the viscosity was halved when the temperature changed from 19 to 30°C.

7.3.8 Surface Potential.

This non-invasive technique gave a very clear macroscopic picture of the behaviour of a monolayer at different surface pressures. At 25mN/m, the film was obviously fluid, and showed evidence of rapid motion, presumably due to extraneous vibrations in the apparatus. At 30mN/m, the film was steady and it did not reflect any vibrations on the time scale observed at 25mN/m; rather, it showed fluctuations on the time scale of minutes. At 40mN/m, the film was again observed to fluctuate rapidly, and in this case it is thought that the increased viscosity of the monolayer has rendered it rigid, and therefore caused it to mirror the apparatus vibrations to a larger extent than did the 25mN/m film. This confirms the theory in Section 7.3.5, on why the 40mN/m film needs to be dipped slowly. The observation at 30mN/m also helps to explain the fact that a 30mN/m film cannot be dipped slowly. A dipping speed of 5mm/min means the substrate is picking up monolayer on the same time scale as the fluctuations in surface potential, thus giving a disordered film.

7.3.9 The Polysiloxane.

This molecule was studied to provide continuity with previous work in the group. The monolayer thickness obtained from the LB film samples agrees well with the previous values obtained from the neutron reflectivity experiments on Langmuir films of the molecule.

7.3.10 Summary of Acid Films.

As a result of this study of the parameters affecting the formation of ordered LB films of fatty acids, it is concluded that the most important parameter is the monolayer phase, which is determined by the surface pressure of the monolayer and the temperature of the subphase. The monolayer phase will affect the speed at which an ordered, unscrambled

film may be prepared, and for given values of surface pressure and temperature, the dipping speed required for the formation of an ordered film can be experimentally determined. Surface potential data have been used to provide a qualitative illustration of the structure of the monolayer at three surface pressure values relevant to the present work, and this picture supports the theory on why scrambling occurs at certain combinations of surface pressure and dipping speed and not others. The time between the down- and upstrokes of a labelled layer has been found to have little or no effect on the extent of scrambling, for times as long as minutes. Two samples across the phase (i.e. surface pressure)/speed matrix have been shown to be completely unscrambled, with a further three showing only slight scrambling. The conclusion from these results is that the Langmuir film has to be in the S phase, and must be dipped at a rate which ensures complete and uniform transition to the L_2 phase during deposition, in order to produce an unscrambled film.

7.4 Amine-Acid Films.

7.4.1 Rationale

Amine-acid films were dipped to provide an alternative molecular architecture with which to test the modelling, as well as to provide useful supporting data for pyroelectric studies carried out by collaborating groups. The series of samples began with the monomeric fatty acid used in the previous series, to facilitate direct comparisons. Subsequently, samples were dipped with polymeric fatty acids, which have previously produced good pyroelectric films.

7.4.2 Amine and Monomeric Acid.

It was found that films dipped with the acid on the first downstroke were disordered, whereas films dipped with the amine first were ordered, with no scrambling. This is explained in terms of the evidence obtained from the thickness values from the X-ray

data, for a different phase change for the acid when dipped against the amine, namely from the S phase in the monolayer to the L_2' phase in the dipped film, compared with S to L_2 for the acid dipped against itself. If dipped first, the acid adopts the usual L_2' phase, the amine deposits in the equivalent of the L_2 phase and a disordered film results. If, on the other hand, the amine is dipped first, it dictates the phase adopted by the subsequent acid layer and an ordered film results. This pronounced effect of the amine on the packing of the acid is due to the strong headgroup binding between the COOH and NH_2 moieties, especially at the pH of 5.5 which was used as a compromise between the requirements of the acid and those of the amine. Thus it would seem that, under most conditions, relaxation to the L_2 phase, and therefore 30° chain tilt, results in an open and disordered layer, and hence a disordered and scrambled film, although even in this phase of the monolayer, films have been prepared which remain unscrambled. This is further confirmation of the conclusions drawn from the acid-acid samples with regard to poor quality films from monolayers with little or no long-range order. The current theory on the origin of the pyroelectric effect, namely changes in molecular dipole moment, was confirmed by a sample which showed increased thickness on heating.

7.4.3 Amine and Polymeric Acids.

Isotherms of these molecules showed them to be very fluid, and so it was not surprising to find that LB films of them dipped against the amine showed no internal order at all, with the labelled layer distributed throughout the preceding layers. Given that these molecules are known to show good pyroelectric responses, there is potential for LB films with even better response if the molecules could be designed to dip more efficiently against the amine headgroups. This result also explains why other workers have needed to dip layers of fatty acid interleaved between the polymer, in order to obtain a good pyroelectric response - the acid introduces the required measure of order for the polymer dipole moments to be effective.

7.4.4 Summary of Amine-Acid Films.

Increased head-to-head interaction, such as is achieved by dipping acid against amine, is shown to result in ordered, unscrambled films. Three polymers are shown to be too fluid, i.e. not to possess sufficient long-range order, to dip ordered films.

7.5 Overall Conclusions.

Neutron reflectivity has been used, in conjunction with X-ray reflectivity, to investigate order within alternating LB films. Single-layer models were satisfactory for fitting the X-ray data. For the neutron data, a new modelling approach has been developed, which uses a gaussian profile to model the distribution of deuterium-labelled material within the sample. The results from this approach are consistent with the conclusions of other workers, but by enabling better-quality fits to be obtained have greatly enhanced understanding of the scrambling phenomenon.

Samples with only one deuterium-labelled layer have been shown to give the required information on the distribution of that labelled layer through the film, which is not possible with alternating structures. By *varying the experimental* parameters, it has been shown that consideration of both dipping speed and film viscosity (i.e. monolayer phase) enables LB films to be prepared in which the labelled layer has not mixed with the surrounding layers. A Langmuir film of a fatty acid has to be in the S phase, and must be dipped at a rate which ensures complete and uniform transition to the L_2 phase during deposition, or the L_2' phase if the head-head binding is significant, e.g. dipping against an amine, in order to produce an unscrambled film.

The preparation of LB films of docosanoic acid alternating with eicosylamine has shown that with increased headgroup interaction, scrambling is totally eliminated. This has been explained in terms of differences in film phase and head-to-head interactions when compared with acid-acid films.

Polysiloxane molecules with side chains having terminal carboxylic acid groups are shown to form LB films with insufficient layer structure to allow a labelled layer to remain unmixed. This result is used to explain the empirical result of workers at Sheffield and Hull ([7] in Chapter 6), that the pyroelectric effect of films of such molecules is enhanced by the periodic inclusion of bilayers of a fatty acid.

Appendix 1. Second Harmonic Generation.

Second Harmonic Generation (SHG) is most simply described as two incoming photons of frequency ω combining to give one emerging photon of frequency 2ω. The physical basis for this is as follows:

The molecular polarisation p due to an electro-magnetic wave is

$$p = \alpha E + \beta E^2 + \gamma E^3 + ...$$

where

E is the applied field

α, β and γ are constants for a particular molecule, the hyperpolarisability β being the most interesting quantity for the present discussion. α is the linear polarisability and is the origin of refractive index.

βE^2 and γE^3 are non-linear terms. Terms higher in E make a negligible contribution to the polarisation.

The macroscopic polarisation P in a linear optically-active material may therefore be expressed as

$$P = \varepsilon_0 \chi^{(1)} E$$

where

ε_0 is the permittivity of free space

$\chi^{(1)}$ is the first order susceptibility tensor and is the contribution from the molecular αs over the bulk.

Similarly, the bulk polarisation in a material with non-linear optical (NLO) properties is given by

$$P = \varepsilon_0 (\chi^{(1)} E + \chi^{(2)} E^2 + \chi^{(3)} E^3 + ...)$$

where

$\chi^{(2)}$ is the second order susceptibility tensor and is the contribution from the molecular βs over the bulk

$\chi^{(3)}$ is the third order susceptibility tensor and is the contribution from the molecular γs over the bulk.

Again, terms higher than the third in E are negligible in practice.

The second order term is the one of interest here. If E is from an electromagnetic wave, as it will be in the present case of light incident on an active material, it is described by

$$E = E_0 (\cos \omega t)$$

Hence

$$E^2 = E_0^2 (\cos^2 \omega t)$$

$$= E_0^2 (\tfrac{1}{2} + \tfrac{1}{2} \cos (2\omega t))$$

This is therefore the origin of the frequency doubling effect i.e. second harmonic generation, and

$$P = \tfrac{1}{2} \chi^{(2)} E_0^2 + \chi^{(1)} E_0 \cos \omega t + \tfrac{1}{2}(\chi^{(2)} E_0^2 \cos 2\omega t)$$

A noncentrosymmetric material is needed: if a symmetric material is used, the direction cosine terms of the molecular dipole moments cancel out and the $\chi^{(2)}$ component is equal to zero. Alternating LB films would be a very useful means of engineering such a structure, especially given the difficulty of the alternative, namely designing materials that naturally crystallise with their molecular dipoles in a noncentrosymmetric lattice. Also, if the sample is bulky a large part of the signal will be lost by absorption and again LB films would provide a solution to the problem, by means of their thinness.

The chief application of $\omega \rightarrow 2\omega$ frequency doubling is infra-red up-conversion: for instance, laser light at 1.064 μm (IR) can be frequency-doubled up to 532 nm (visible, green). This principle has great potential in the field of night vision and mountain rescue situations, where the small size and low weight of an LB-film-based system would be an

advantage over current lithium niobate-based apparatus. Since the emergent light is coherent, any laser radiation may be similarly frequency doubled to provide laser radiation at much shorter wavelengths than are obtainable by other means, although obviously intensity is halved at each frequency doubling.

A further application is the Pockels or electro-optic effect, whereby the refractive index of the material changes following a change in the surrounding electric field. This can be used to switch optical signals in telecommunications, for example, and again the thinness of LB films is an advantage, ensuring fast response times.

The third order hyperpolarisability, $\chi^{(3)}$, although as yet very small in even the most advanced materials, is nevertheless a useful property due to its far less stringent lattice requirements: a centrosymmetric system will not cancel it out. It has potential uses in optical bistability, since the refractive index changes with the intensity of the incoming light (Kerr effect), although since the emergent intensity will be only one third of the incident intensity, the material must be able to withstand high intensity illumination if the effect is to be of practical use.

References

I. R. Girling et al., Thin Solid Films, **132**, 101 (1985).

G. Ashwell et al., Proc SPIE - Int. Soc. Opt. Eng. **1361**, 589 (1991).

R. Tredgold, Order in Thin Organic Films, Cambridge University Press (1994), pp. 105-107.

Appendix 2. Pyroelectricity.

Pyroelectricity is the production of a current within a material as its polarisation changes in response to a change of temperature. The phenomenon is used chiefly for thermal imaging. The magnitude of the pyroelectric current is directly proportional to the rate of change of temperature, as given by the equation below:

$$I = Ap\frac{dT}{dt}$$

where

I is the pyroelectric current

A is the surface area of the device

p is the pyroelectric coefficient of the material, also described as the rate of change of polarisation of the material with temperature.

$\frac{dT}{dt}$ is the rate of change of temperature.

p is therefore the figure of merit for pyroelectric devices, and for polyvinylidene fluoride (PVDF), a commercially available pyroelectric polymer, $p = 3 \times 10^{-9}$ C cm^{-2} K^{-1}. For LB films of acid-amine systems, values of p have been obtained in the range 0.3 - 1.0 x 10^{-9} C cm^{-2} K^{-1}, depending on thickness [Christie et al.], which compares very favourably with existing technology.

For a material to show pyroelectric behaviour it must have no centre of symmetry and also must have a unique polar axis. This unique polar axis is associated with a surface charge Q, which is related to the potential V across the film by

$$V = \frac{QNd}{A\varepsilon}$$

where

N is the number of bilayers deposited, i.e. repeat units within the structure

d is the bilayer thickness

A is again the area of the device

ε is the electric permittivity of the material.

The surface charge Q is in turn associated with proton transfer between the molecules of the material, for instance the amine-acid headgroups of the molecules used in the present work, and the temperature-dependence of this transfer is the origin of the pyroelectric current. Alternatively, the change in temperature may change the tilts of the molecular dipoles within the material, thus changing the normal component of the polarisation and hence generating a pyroelectric current.

The requirement for a noncentrosymmetric structure, and the ease with which the thickness of an LB film may be ordained at the molecular level, make it highly desirable to use the LB technique to fabricate pyroelectric devices whose properties may thus be precisely tuned to the intended application.

References

P. Christie, G. G. Roberts and M. C. Petty, Appl. Phys. Lett. **48**, 1101 (1986).

T. Richardson, W. H. A. Majid, E. C. A. Cochrane, S. Holder and D. Lacey, Thin Solid Films, **242**, 61 (1994).